Experimental Studies of Electron–Phonon Interactions in Gallium Nitride

by

Nicola Marie Stanton

Thesis submitted to the University of Nottingham for the degree of Doctor of Philosophy, October 2001.

Contents

List of Figures

Acknowledgements

I would like to extend my gratitude to the following people who have assisted me during the last three years.

Dr. Tony Kent, for being an excellent supervisor, offering limitless support and encouragement and making all this possible; Professor Andrey Akimov, for beautiful experiments, friendship and vodka; The Phonon Group, especially Al Pentland, Stu Cavill and Phil Hawker for their seemingly constant sarcasm and frequent assistance with the experiments.

Prof. Tom Foxon, for a remarkable interest in everything and care for everyone, NOAH and red wine; The Nitrides Group old and new, for good times.

The Department, for making the time so enjoyable; The Technical staff, for all their help, especially with vacuum pumps.

My Housemates over the years (especially John Brookes, for being JB) for taking me out when it was necessary and listening to my ramblings.

Finally, I would like to thank the people who have offered unquestioning support. Dr. Richard Campion, for learning more about phonons then he ever wanted to know and, more importantly, for everything else; and my Parents, who never doubted me, always believing this would happen.

List of Publications

"Absorption of Nonequilibrium Acoustic Phonons by Low-mobility Electrons in GaN" N.M. Stanton, A.V. Akimov, A.J. Kent, T.S. Cheng and C.T. Foxon *Appl. Phys. Lett.* **78** 1089 (2001)

"Energy Relaxation by Hot Electrons in n-GaN Epilayers" N.M. Stanton, A.J. Kent, A.V. Akimov, P. Hawker, T.S. Cheng and C.T. Foxon *J. Appl. Phys.* **89** 973 (2001)

"Imaging Phonon Drag in Gallium Nitride" N.M. Stanton, A.V. Akimov, A.J. Kent, S.A. Cavill, T.S. Cheng and C.T. Foxon *Appl. Phys. Lett* **77** 3403 (2000)

"Photoenhanced Wet Chemical Etching of MBE Grown Gallium Nitride" N.M. Stanton, A.J. Kent, P. Hawker, T.S. Cheng, C.T. Foxon, D. Korakakis, R.P. Campion, C.R. Staddon and J.R. Middleton *Mat. Sci. Eng. B.* **68** 52 (1999)

"Hot Electron Energy Relaxation in Gallium Nitride" N.M. Stanton, P. Hawker, A.J. Kent, T.S. Cheng and C.T. Foxon *Phys. Stat. Solidi A* **76** 369 (1999)

"Energy Relaxation by Warm Two-dimensional Electrons in a GaN / AlGaN Heterostructure" N.M. Stanton, A.J. Kent, S.A. Cavill, A.V. Akimov, K.J. Lee, J.J. Harris, T. Wang and S.Sakai *(Accepted for publication in Phys. Stat. Solidi)*

"Phonon and Photon Emission from Optically Excited InGaN/GaN

MULTIPLE QUANTUM WELLS" A.V. Akimov, A.J. Kent, S.A. Cavill, N.M. Stanton, T. Wang and S. Sakai *(Accepted for publication in Phys. Stat. Solidi)*

"NONRADIATIVE PROCESSES AND PHONON EMISSION IN GAASN ALLOYS" S.A. Cavill, A.V. Akimov, N.M. Stanton, A.J. Kent, S.V. Novikov, I. Harrison and C.T. Foxon *(Submitted.)*

"PHONON EMISSION FROM THE RELAXATION OF PHOTOEXCITED CARRIERS IN INGAN/GAN QUANTUM WELLS" A.V. Akimov, A.J. Kent, S.A. Cavill, N.M. Stanton, T. Wang and S. Sakai *(Submitted to J. Phys. C)*

Abstract

This Thesis presents an experimental investigation of the electron–phonon interaction in GaN. Bulk epilayers, grown by MBE, and AlGaN/GaN heterostructures, grown by MOCVD, have been studied.

The energy relaxation rate for hot electrons has been measured over a wide range of temperatures, allowing both acoustic and optic phonon emission to be studied in GaN epilayers. Direct phonon measurements, both studying the emission and absorption processes, have been performed. Detection of phonons emitted when hot electrons relax their excess energy complements the measurements of relaxation rates. Absorption of acoustic phonons by the epilayers, using both fixed and extended metal film phonon sources, allowed investigation into the effectiveness of the $2k_F$ cutoff in the low mobility layers. The experimental findings are compared with the predictions of theory.

AlGaN/GaN heterostructures were characterised and measurements of the energy relaxation rate in the temperature range 4K–40K obtained. Excellent agreement with theory is observed. A preliminary study of phonon absorption by the 2DEG system is presented, which allowed experimental determination of the "thickness" of the 2DEG and demonstrated the applicability of the technique in the study of low dimensional systems.

List of Symbols

a_o – Fang–Howard parameter

B – Magnetic field

C_{-1} – Directionally averaged piezoelectric coupling constant

C_{+1} – Deformation potential coupling constant

$C_{ij\ell m}$ – Elements of the elastic tensor

$D(E)$ – Density of states

d – Epilayer thickness

E_F – Fermi energy

e – Electronic charge

e_{31}, e_{33}, e_{15} – Piezoelectric constants

$e_{\ell mn}$ – Piezoelectric tensor

E_m – Electric field

$e_{\ell m}$ – Strain tensor

f_k – Fermi–Dirac distribution function

$|F(q)|$ – Bound state form factor

f_E – Electron distribution function

$\hbar$ – Planck's constant

i – Landau level index

j – Current density

k_B – Boltzmann constant

k_F – Fermi wavevector

L_x, L_y, L_z – Normalisation lengths

ℓ – Electron mean free path

m^* – Electron effective mass

m_e – Electron mass

M – Matrix element of the electron–phonon interaction

N, n, n_e – Carrier concentration

N_s, n_s – Sheet carrier concentration

$n_{(q,\lambda)}$ – Bose–Einstein distribution function

N_q – Phonon population

$P_{(q,\lambda)}$ – Energy relaxation rate into a phonon mode λ

P_e – Power loss per electron

q – Phonon wavevector

$q_{\|}$ – Component of phonon wavevector parallel to plane of 2DEG

r_s – Thomas–Fermi screening radius

R_{abs} – Phonon absorption rate

R_D, R_{dev} – Device resistance

S, s – Screening parameter

T_e – Electron temperature

T_ℓ – Lattice temperature

T_h – Heater temperature

T_C – Superconducting transition temperature

v_s – Sound velocity

v – Electron drift velocity

V – Crystal volume

v_P –Phase velocity

v_F –Fermi velocity

V_{def} – Deformation potential

$W_k^{k'}$ – Transition probability

α_{eff} – Effective Stefan constant

α – Fröhlich coupling constant

α_{abs} – Fractional absorption

$\delta_{i\ell}$ – Kronecker delta

ϵ, ϵ_{11}, ϵ_{33}, ϵ_∞, ϵ_s – Dielectric constants

λ – Phonon polarisation vector

λ_D – inverse Debye screening length

$\Lambda_k^{(q,\lambda)}$ – Phonon emission rate

μ – Electron mobility

ρ – Crystal density

Ξ_d – Deformation potential coupling constant

$\rho(\omega)$ – Phonon density of states

τ – Electron–phonon scattering time

τ_0 – Ballistic transit time

τ_P – Momentum relaxation time

τ_c – Classical scattering time

τ_q – Quantum scattering time

$\hbar\omega$ – Phonon energy

ω_P – Plasma frequency

ω_+, ω_- – Coupled mode frequencies

ω_c – Cyclotron frequency

Subscript or label "LA" refers to longitudinal acoustic phonons

Subscript or label "TA" refers to transverse acoustic phonons

Chapter 1

INTRODUCTION

1.1 AN INTRODUCTION TO NITRIDE SEMICONDUCTORS

The Group III nitrides represent a significant development in inorganic semiconductor growth and application. Unlike gallium arsenide, with its cubic crystal structure and relatively small bandgap, gallium nitride (which generally crystallises in the wurtzite structure) has a wide, direct bandgap. It is for these reasons that gallium nitride and its alloys have been the focus of much attention, due to their successful exploitation in the manufacture of blue/UV laser diodes, LED's and high power electronic devices (for a review of recent achievements, see [1], [2], [3] and references therein).

There are many available strategies for growth; MOCVD and HVPE produce layers with the highest quality to date and are the favoured methods. MBE, dominant in the growth of GaAs, is achieving layers of improving standard. With so many potential applications, the quest for improved material characteristics is likely to continue for some time. High speed growth of low defect density, thick layers will serve to perhaps solve one of the fundamental problems in the growth of GaN; there is no lattice matched substrate. Sapphire and silicon carbide (the popular choices) are lattice mismatched by ~16% and ~5% respectively;

overcoming the strain this introduces into the epilayer during growth is likely to be the biggest hurdle to thick layer growth.

Another significant difference in behaviour (when compared to other III–V compounds) is the resistance of GaN and its alloys to chemical attack (a potential advantage of the material if devices are to used in "difficult" environments). A fundamental stage in development of devices is the ability to successfully process material. Unlike other semiconductors (for example GaAs), which are attacked by several mineral acids and bases, GaN is unaffected by even the strongest acids. Developments of wet etching techniques remains an active area of research. The effects of material homogeneity, growth method and the role of defects in this process are not fully understood. Processing of AlGaN and InGaN therefore relies on dry etching methods. Developing materials, principally the gallium nitride-arsenides, may prove easier to process, but this has yet to be tested.

Despite the success in fabrication of blue LED's and laser diodes, along with AlGaN/GaN based FET's, there are many fundamental aspects of the material behaviour that are not understood. Although theoretical studies describing various areas of device performance are numerous, many of the parameters of GaN are still relatively ill–defined. This makes theoretical treatments difficult, and the assumptions involved are often unrealistic, especially in a material with so many defects. Optical measurements have, to date, dominated the experimental studies of material properties . With the large bandgaps involved, the use of UV illumination and optics are required.

It is interesting to note that although the defect density is high in all growth modes, vastly different layer morphologies can be obtained with the different techniques. The majority of work is performed on MOCVD material; MBE material has received less attention. The AlGaN/GaN heterostructure is of interest due to its use in high power applications, whilst the InGaN/GaN multi quantum well (MQW) is now widely used in optics. These systems of reduced dimensionality have been studied by Raman spectroscopy, but little information regarding energy loss and the behaviour of phonons is available (theoretical discussions can be found in [4], [5]). The trend in semiconductor device manufacture is to fabri-

cate smaller devices. When a voltage is applied across the devices, large electric fields are produced. The result is substantial heating of the electrons. The hot electrons relax their excess energy by emission of phonons, and how efficiently this process can occur is of vital importance in understanding and predicting the ultimate limitations of device performance.

The relaxation processes and phonon dynamics in GaAs are fairly well understood (in 3D and 2D), but GaN, in relatively early stages of study, presents many new challenges, both in theoretical description and in experimentation. The different crystal symmetry, along with its very different bandgap, band structure and phonon dispersion relations suggest different and interesting behaviour from other well established semiconductors. Material quality of GaAs is much better than for GaN–how the disorder affects the basic properties will provide valuable information for future device designs.

This work aims to study the fundamental behaviour of GaN. Bulk material produced using different growth methods (and therefore of varying quality) has been studied. Recent work has concentrated on AlGaN/GaN 2DEG's (including processing issues). Energy relaxation experiments provide a wealth of information about the nature of the material and the temperature dependence of the processes involved in energy dissipation. Phonon emission experiments can give direct information concerning the mode dependence of emission, and can also provide an insight into the energy and momentum conservation, which cut off emission at certain frequencies and in certain directions. This is not possible in experiments that do not resolve phonon modes. As the dimensionality of the system is reduced, the effects on energy relaxation will be significant due to the reduction in phase space for electron scattering. Phonon absorption is another useful tool for studying the behaviour of systems, allowing the temperature dependence of different coupling mechanisms to be obtained.

1.2 THE ADVENT OF NITRIDE INTEREST

The first attempts to grow GaN were in 1970. At that time, the technique of MBE was still in development, although GaAs growth was at this time progressing with reasonable success. Thus it was CVD and sputtering techniques which were primarily used for GaN growth. The history of the growth of GaN is well documented, and the main point to note that it is only during the last decade that GaN and its alloys have been grown of sufficient quality to allow fabrication of semiconductor devices (reviews of current growth techniques can be found in [6], [7]).

The driving force in growth is towards technological exploitation – and so formation of high mobility 2DEG's is an obvious goal. The polarity of GaN (determined by the orientation of the bonds in relation to the surface) is of fundamental importance in GaN growth since, unlike GaAs growth, doping is not required to cause confinement of carriers at the heterointerface [8].

Today there exist a variety of techniques which can be employed for GaN growth. The growth techniques vary depending on precursor material, achievable growth temperature (which is also limited by substrate choice), and pressure regime. Temperature is an important consideration in GaN growth – production of high quality films relies on the deposited material having sufficient surface mobility to allow a 2D growth to occur. When the temperature is lowered, so is surface mobility and the tendency is then one of 3D growth, characterised by grain boundary formation and resulting in polycrystalline material. MOVPE, MOCVD and HVPE are all high (atmospheric) pressure processes, and so achieving high substrate temperatures is easier than in MBE. However, these methods use vast quantities of pre–cursors in comparison with MBE – a consideration if industrial application of the method is sought.

MOVPE, MOCVD and HVPE, to date, produce films of the highest quality, based on the mobility of the 2DEG's grown on these epilayers. MBE, the work–horse of GaAs growth, now yields films of good quality, but appears to be hindered by a tendency to grow N–polarity films, making growth of AlGaN/GaN 2DEG's

difficult. Determining the polarity of films is not simple – it is believed that "etch tests" can show which polarity is grown, although this issue is not yet resolved [9], [10] (see Appendix I for a more detailed discussion). The advantage of the MBE process lies in the ability of the technique to produce abrupt changes of composition in layered structures.

The definition of "quality" in nitride films requires comment. There are many techniques which are employed in the characterisation of layers. X–ray studies provide information on the crystal structure, determining whether wurtzite or cubic material is grown or a mixture of both structures. Photoluminescence studies allow observation of impurity states. Surface morphologies are mapped using AFM and interface quality can be determined by TEM. The interface between substrate and epilayer has been the source of much interest. The lack of a GaN substrate means that growth is performed on lattice mismatched substrates. Sapphire and SiC are the most widely chosen, although growth is also performed on silicon and on GaAs. The mismatch between layers introduces defects into the layer and different thermal expansion coefficients can cause cracking or bowing of the epilayer during cool–down from growth temperature. All growth modes described above suffer from a high dislocation density – how these defects behave in the material is still an area of study. The desire to reduce defects has led to the technique of "epitaxial lateral overgrowth" (either called ELO or LEO) which involves growing GaN over silicon dioxide stripes on the substrate. Under the right conditions, in the GaN above the stripes, the threading dislocation density will be significantly reduced [11].

Despite high numbers of defects, working devices are still achievable. It is possible that the dislocations aid a number of processes – for example, wet etching of GaN (a trivial task in GaAs processing) may rely on the presence of these defects. Describing a film as low or high quality is therefore based on the sample mobility. Improvements in growth are occurring rapidly–as are the mobilities of 2DEG's. At the beginning of 1999, the record mobility of an AlGaN/GaN 2DEG on sapphire was $\sim$10 000 $cm^2V^{-1}s^{-1}$ [12]. The recent use of a thick template layer produced a peak low–temperature mobility of $\sim$53 300 $cm^2V^{-1}s^{-1}$ [13], whilst the

use of small area single crystal GaN as a substrate produced a mobility of ~60000 $cm^2V^{-1}s^{-1}$ [14] (c.f. ~10 000 000 $cm^2V^{-1}s^{-1}$ in AlGaAs/GaAs 2DEG's).

Another interesting feature of the Group III–nitrides is relatively large spontaneous polarisation [15]. Due to the relative size and electronegativity of the constituent atoms, a self–polarisation field is induced in GaN layers. The direction of the spontaneous polarisation, along with the piezoelectric polarisation induced due to internal strain in the layers can cause either an accumulation or depletion of carriers at the interface. This is why the highest mobility 2DEG's are those grown on the Ga–polarity material. If nitrogen terminates the surface, the spontaneous fields oppose carrier accumulation at the interface [16].

With so much characterisation work performed, it is perhaps surprising that little work regarding the behaviour of phonons has been performed. Studying the electron–phonon interaction is of fundamental importance since energy relaxation occurs predominantly via phonon emission. The desire to achieve high mobility transistors also requires an understanding of phonon behaviour since it is phonon scattering that limits the mobility at all but the lowest temperatures.

1.3 THE DEVELOPMENT OF PHONON STUDIES

The first heat pulse experiments were performed almost forty years ago by von Gutfeld and Nethercot [17]. The basic idea was that a non–equilibrium pulse of phonons produced on one side of a crystal could be detected directly on the opposite face. The phonons propagated ballistically, and since different phonon modes would arrive at the detector at different times, the fundamental elastic properties of the crystal could be studied. At room temperature, phonons scatter readily and so propagation is diffusive. When the temperature is lowered, the phonon mean free path increases rapidly, and ballistic propagation is possible over macroscopic distances. In the early work, altering the position of the phonon source allowed the direction dependence of phonon propagation to be studied.

Several variations of the experiment were subsequently performed, changing the detector, crystal and geometry, but the basic idea remains the same.

A major development came with the work of Hensel and Dynes [18], and an adaptation shortly after by Northrop and Wolfe [19], [20]. The technique was phonon imaging, where a map of the phonon intensity across the surface could be obtained. Originally, this involved optical excitation of a metal film on one side of the crystal. The sample was rotated, and with the detector fixed, this allowed angular resolution of phonon intensity. The technique was modified by holding the sample in place and scanning the laser across the film. Phonon focussing images provide an excellent method for direct observation of acoustic anisotropy in crystals (see, for example, [21]).

With the crystal nature better understood, the electron–phonon interaction can be studied by changing the phonon source or detector. If the source is changed from a metal film to a 2DEG, for example, the detected phonons are produced by scattering in the 2DEG and so the nature of emission from the 2DEG is studied. If the epilayer is used as the detector, the absorption of phonons can be then be studied. The basis of all these experiments is the same; detection of ballistic pulses, recording of the signals and variation of either phonon source position or phonon frequency (or both) (see [22] for a review of the techniques).

The study of hot electron energy relaxation is prompted by interest in the fundamental interactions and by a desire to better understand and design devices in which electrons are subject to significant heating ([23], which contains a variety of papers on the subject, and [24]). By studying the temperature dependence of the power dissipation, the dominant energy relaxation mechanism can be determined. A variety of techniques have been employed in measurements of overall energy relaxation rate. An overview of these techniques are discussed in [25], and include photoluminescence measurements (PL) [26], magnetic field measurements [27], [28], and transport measurements [29], [30]. The measurement of energy loss rates using zero–field transport measurements is useful as this technique can be employed over a wide range of temperature [31], unlike optical measurements (which suffer from inhomogeneous line broadening effects)

and magnetic field methods (which cannot be used at high temperatures due to the decreasing amplitude of oscillations as the electron temperature is increased).

More detailed information can be obtained if the emitted phonons are directly observed by bolometric detection. By positioning a detector opposite the device, phonons emitted by the hot electrons can be detected, and consideration of the time of flight of individual modes allows the energy relaxation process to be studied in greater detail than possible by the methods described previously. The ability to move the detector allows the angular dependence of emission to be studied. This technique has been used in conjunction with transport measurements [32], allowing the temperature dependence of individual modes to be studied.

1.4 AIMS OF THIS WORK

Measurement of the energy relaxation allows the optic phonon energy and electron–optic phonon scattering time to be obtained. At lower temperature, acoustic phonon emission is expected to dominate energy loss. Comparison with the predicted energy loss rates allows the effect of screening to be determined, and also to observe any enhanced energy relaxation processes. Direct observation of the emitted phonons allows the crossover from acoustic to optic emission to be observed, and also details which coupling mechanism, piezoelectric or deformation potential, dominates energy relaxation. The cut–offs of the interaction can be studied in phonon absorption experiments. Phonon imaging techniques can be used to show the effects of phonon focussing, as well as allowing emission and absorption processes to be studied in more detail.

The purpose of this work is to study the electron–phonon interaction in GaN, using a combination of transport–type measurements and heat pulse techniques allowing direct observation of phonon modes. This work complements other transport measurements ([33], [34] for example) and Raman studies ([35], [36] and [37] are examples), and also allows comparison with theoretical predictions

to be made.

1.5 OUTLINE OF THESIS

This Chapter has been concerned with outlining the development of the techniques used to study GaN, and to discussing some of the properties of the Group III nitrides which make them so attractive. More detailed descriptions and reviews of previous work will be introduced in later Chapters.

Chapter 2 presents the fundamental concepts relevant to the experiments performed. A brief discussion of the systems and phonon propagation is followed by a detailed description of energy loss. Phonon absorption and imaging techniques are also covered.

Chapter 3 involves discussion of the fabrication processes required to successfully produce samples, and a detailed description of the experimental techniques employed. Processing (including etching and contacting) of GaN has proved troublesome; the final processing steps will be discussed, with the development of the method presented separately in Appendix I. The experimental arrangements for the different studies are explained in depth, including the equipment used and the operation of the detectors and sources.

This work is mainly concerned with the study of epitaxial GaN layers, and Chapter 4 is devoted to presentation of the experimental findings using bulk material. The analysis techniques are described and results presented. Refinements of the experimental method are also discussed. Recent work on the AlGaN/GaN system is discussed in Chapter 5 and follows the same layout as Chapter 4.

Finally, Chapter 6 summarises the conclusions drawn from the experiments and suggests refinements in the techniques and further experiments that would provide a useful extension of this initial investigation.

REFERENCES

[1] S. Nakamura. *Semi. Sci. Tech*, **10**, 641, (1999).

[2] L. F. Eastman. *phys. stat. sol (a)*, **176**, 175, (1999).

[3] B. Monemar. *J. Mater. Sci*, **10**, 227, (1999).

[4] L. Hsu and W. Walukiewicz. *Phys. Rev. B*, **56**, 1520, (1997).

[5] L. Hsu and W. Walukiewicz. *Appl. Phys. Lett*, **73**, 339, (1998).

[6] O. Ambacher. *J. Phys. D: Appl. Phys.*, **31**, 2653, (1998).

[7] J. W. Orton and C. T. Foxon. *Rep. Prog. Phys.*, **61**, 1, (1998).

[8] F. Bernardini and V. Fiorentini. *phys. stat. sol (b)*, **216**, 391, (1999).

[9] E. S. Hellman. *MRS Internet J.Nitride Semicond.Res.*, **3**, 1, (1998).

[10] J. L. Rouviere, J. L. Weyher, M. Seelmann-Eggebert, and S. Porowski. *Appl. Phys. Lett*, **73**, 668, (1998).

[11] H. Marchand, J. P. Ibbetson, P. T. Fini, P. Kozodoy, S. Keller, S. DenBaars, J. S. Speck, and U. K. Mishra. *MRS Internet J.Nitride Semicond.Res.*, **3**, 3, (1998).

[12] T. Wang, Y. Ohno, M. Lachah, D. Nakagawa, T. Shirahama, S. Sakai, and H. Ohno. *phys. stat. sol (b)*, **216**, 743, (1999).

[13] M. J. Manfra, L. N. Pfeiffer, K. W. West, H. L. Stormer, K. W. Baldwin, J. W. P. Hsu, D. V. Lang, and R. J. Molnar. *Appl. Phys. Lett*, **77**, 2888, (2000).

[14] E. Frayssinet, W. Knap, P. Lorenzini, N. Grandjean, J. Massies, C. Skierbiszewski, T. Suski, I. Grzegory, S. Porowski, G. Simin, X. Hu, M. Asif Khan, M. S. Shur, R. Gaska, and D. Maude. *Appl. Phys. Lett*, **77**, 2551, (2000).

[15] F. Bernardini, V. Fiorentini, and D. Vanderbilt. *Phys. Rev. B*, **56**, R10024, (1997).

[16] O. Ambacher, R. Dmitrov, M. Stutzmann, B. E. Foutz, M. J. Murphy, J. A. Smart, J. R. Shealy, N. G. Weimann, K. Chu, M. Chumbes, B. Green, A. J. Sierakowski, W. J. Schaff, and L. F. Eastman. *phys. stat. sol (b)*, **216**, 381, (1999).

[17] R. J. von Gutfeld and A. H. Nethercot. *Phys. Rev. Lett*, **12**, 641, (1964).

[18] J. C. Hensel and R. C. Dynes. *Phys. Rev. Lett*, **43**, 1033, (1979).

[19] G. A. Northrop and J. P. Wolfe. *Phys. Rev. Lett*, **43**, 1424, (1979).

[20] G. A. Northrop and J. P. Wolfe. *Phys. Rev. Lett*, **22**, 6196, (1980).

[21] C. Jasiukiewicz, D. Lehmann, A. J. Kent, A. J. Cross, and P. Hawker. *Physica B*, **263**, 183, (1999).

[22] M. N. Wybourne and J. K. Wigmore. *Rep. Prog. Phys.*, **51**, 923, (1988).

[23] N. Balkan. *Hot Electrons in Semiconductors: Physics and Devices.* Oxford Clarendon Press, 1998.

[24] B. K. Ridley. *Rep. Prog. Phys.*, **54**, 169, (1991).

[25] A. J. Kent in. *Hot Electrons in Semiconductors: Physics and Devices.* Oxford Clarendon Press, 1998.

[26] C. H. Yang, J. M. Calrson-Swindle, S. A. Lyon, and J. M. Worlock. *Phys. Rev. Lett*, **55**, 2359, (1985).

[27] Y. Ma, R. Fletcher, E. Zaremba, M. D'Iorio, C. T. Foxon, and J. J. Harris. *Phys. Rev. B*, **43**, 9033, (1991).

[28] E. Chow, H. P. Wei, S. M. Girvin, W. Jan, and J. E. Cunningham. *Phys. Rev. B*, **56**, R1676, (1997).

[29] E. Chow, H. P. Wei, S. M. Girvin, and M. Shayegan. *Phys. Rev. Lett*, **77**, 1143, (1996).

[30] I. G. Savel'ev, G. Remenyi, G. Kovacs, B. Podor, T. A. Polyanskaya, and S. V. Novikov. *Semi. Sci. Tech*, **14**, 1001, (1999).

[31] J. Shah, A. Pinczuk, A. C. Gossard, and W. Wiegmann. *Phys. Rev. Lett*, **54**, 2045, (1985).

[32] P. Hawker, A. J. Kent, A. J. Naylor, I. A. Pentland, M. Henini, T. S. Cheng, and C. T. Foxon. *Inst. Phys. Conf. Ser.*, **162**, 571, (1998).

[33] R. J. Molnar, T. Lei, and T. D. Moustakas. *Appl. Phys. Lett*, **62**, 72, (1992).

[34] J. J. Harris, K. J. Lee, I. Harrison, L. B. Flannery, D. Korakakis, T. S. Cheng, C. T. Foxon, Z. Bougrioua, I. Moerman, W. Van der Stricht, E. J. Thrush, B. Hamilton, and K. Ferhah. *phys. stat. sol (a)*, **176**, 363, (1999).

[35] V. Y. Davydov, Y. E. Kitaev, I. N. Goncharuk, A. N. Smirnov, J. Graul, O. Semchinova, D. Uffmann, M. B. Smirnov, A. P. Mirgorodsky, and R. A. Evarestov. *Phys. Rev. B*, **58**, 12899, (1998).

[36] L. Bergman, D. Alexson, P. L. Murphy, R. J. Nemanich, M. Dutta, M. A. Stroscio, C. Balkas, H. Shin, and R. F. Davies. *Phys. Rev. B*, **59**, 12977, (1999).

[37] K. T. Tsen, R. P. Joshi, and D. K. Ferry. *phys. stat. sol (b)*, **204**, 106, (1997).

Chapter 2

FUNDAMENTAL CONCEPTS

2.1 INTRODUCTION

The purpose of this Chapter is to introduce some of the theoretical principles underlying the experiments described in the later Chapters of this Thesis. The mathematical foundations of phonon physics and the electron–phonon interaction have been studied extensively by a number of workers for systems such as GaAs and Si. The aim here is to extend these theories to GaN and AlGaN/GaN systems. Although the majority of work has been concerned with properties and interactions in 3D systems, an extensive study of energy relaxation has been performed for the 2D AlGaN/GaN system. A description of the systems will be presented. The propagation of phonons in a crystal will be discussed, along with the effects of the lattice mismatched substrate and the interface. The theoretical description of power loss by phonon emission will be considered in detail, for both 3D and 2D systems. Phonon absorption and drag effects will also be covered.

2.2 3D AND 2D ELECTRON SYSTEMS

Electrons in GaN epilayers are termed "3D" as the sample dimensions are much greater than the Fermi wavelength. In bulk layers, the electron wavefunctions

take the form

$$\psi(r) = (L_x L_y L_z)^{-1/3} e^{ik_x x} e^{ik_y y} e^{ik_z z} \tag{2.2.1}$$

The electronic density of states is given in Equation 2.2.

$$D(E) = \frac{V}{2\pi^2 \hbar^3} (2m^*)^{3/2} E^{1/2} \tag{2.2.2}$$

where $\hbar$ is Planck's constant and m^* is the electron effective mass.

The Fermi energy, obtained by integration of the density of states between 0 and E_F is

$$E_F = \frac{\hbar^2}{2m^*} \left(\frac{3\pi^2 N}{V} \right)^{2/3} \tag{2.2.3}$$

and so k_F, the radius of the Fermi sphere is

$$k_F = (3\pi^2 N)^{1/3} \tag{2.2.4}$$

where N is the carrier concentration.

A 2DEG can be formed if a thin layer of AlGaN is grown directly onto a GaN epilayer. The band gap of GaN is 3.42 eV, while the band gap of AlGaN for a 20% aluminium composition is ~4 eV (assuming Vegard's law). The steps in the conduction and valence bands are determined by the difference in electron affinity in the two materials. The band bending that occurs at the interface produces an approximately triangular potential well. Carriers are free to move in the plane parallel to the interface, but the confining potential results in a series of discrete energy levels in the well. These levels are termed subbands and their separation is large enough that for most cases, carriers will only occupy the lowest energy state.

The energy levels of the system can be calculated by solving the Schrödinger equation (approximating the situation to a particle in a box). The energy is given by

$$E = \frac{\hbar^2\pi^2}{2m^*}\left(\frac{(\ell^2 + m^2)}{L^2} + \frac{n^2}{d^2}\right) \tag{2.2.5}$$

where ℓ, m and n are the quantum numbers for the states and d and L are dimensions of the 2D gas.

In the x–y direction (parallel to the interface), the electron energy levels are close enough together that they are indistinguishable and form a continuum of levels, whereas in the z direction, the energy levels separation is large compared to the thermal energy. As the electrons are confined to a film thickness d, a reduction in confinement distance increases the energy level separation and at low temperatures, electrons would occupy the ground state.

In this case, the density of states is

$$D(E) = \frac{m^*}{\pi\hbar^2} \tag{2.2.6}$$

and since the carrier concentration is given by $N_s = D(E)E_F$ then the radius of the Fermi circle is given by

$$k_F = \sqrt{2\pi N_s} \tag{2.2.7}$$

In practice, the z component term is replaced with the Fang–Howard wavefunction, which assumes electrons are confined in a triangular potential well. The Fang–Howard wavefunction,

$$\psi_0 = \frac{1}{(2a_0^3)^{1/2}}\, z\, exp\left(\frac{-z}{2a_0}\right) \tag{2.2.8}$$

where a_0 is the Fang–Howard thickness parameter, and is related to the "thickness" of the 2DEG ($\sim 3a_o$).

The electron wavefunction (as given in Equation 2.2.1) is thus

$$\psi(r) = (L_x L_y)^{-1/2} e^{ik_x x} e^{ik_y y} \psi_0 \tag{2.2.9}$$

2.3 PHONON THEORY

In a crystalline solid, atoms are arranged in a lattice with a regular spacing between adjacent sites. These atoms can be thought of as being confined in a potential well due to the forces of their nearest neighbours. For most purposes, it is reasonable to consider only nearest neighbour interactions. At zero temperature, the motion is small (high mass means the zero–point motion is small). As the temperature is increased, the atoms gain energy and can oscillate around their equilibrium positions. The energy of the system is quantised; the fundamental energy of vibration is $\hbar\omega$ and is called a phonon.

As the temperature is increased, the thermal energy $k_B T$ is increased and the phonon population, described using the Bose–Einstein distribution function, given by Equation 2.3.1, is high.

$$N(\omega) = \frac{1}{e^{\frac{\hbar\omega}{k_B T}} - 1} \tag{2.3.1}$$

The phonon mean free path is short and phonons can scatter with one another, resulting in diffusive behaviour. As the temperature reduces, the phonon population decreases and the mean free path in the crystal increases, eventually limited by the crystal dimensions. Phonon propagation is now ballistic; phonons can traverse a low defect crystal without undergoing any scattering events, travelling distances up to a few millimetres in high quality crystals..

Dispersion curves are plots of wavevector, q, against frequency, and allow some of the properties of phonons to be easily extracted. The dispersion curves for gallium nitride are shown in Figure 2.1, from [1] (see also [2], [3]). The curves can be considered as two groups; the lower frequency group and the high frequency group. These two groups are further split into three curves, corresponding to the three spatial dimensions. The lower frequency branches are associated with acoustic phonons, so called because of the similarities with sound waves, while the high frequency branches are associated with optic phonons. It is the acoustic phonons which are responsible for heat transport in non–metallic solids, and their emission dominates energy relaxation at low temperatures. The group velocity is

given by $d\omega/dq$, the slope of the dispersion curve. For a small range of q (near $q \sim 0$), the velocity of acoustic modes is assumed constant and acoustic modes can be described by $\omega = v_s q$. There are two polarisations of acoustic phonons, termed longitudinal (LA) or transverse (TA). In an ideal crystal, LA modes are associated with displacement of atoms along the direction of propagation, while TA modes are due to motion perpendicular to the propagation direction. Since there are two orthogonal perpendicular directions, the TA modes can be further split into "fast" and "slow" modes. In an isotropic crystal, these modes are degenerate, as is the case when travelling along directions of high crystal symmetry in an anisotropic crystal. The directionally averaged velocities of LA and TA modes in GaN are 6560ms^{-1} and 2680ms^{-1} respectively, with the difference arising due to differences in compressive and shear forces. In the limit of high q, the velocity is no longer constant since the wavelength is no longer much larger than the lattice spacing.

Acoustic phonons have frequencies which extend into the THz range. The maximum frequency is limited by the atomic spacing. From the dispersion relations it is clear that the optic phonons have a small group velocity and can therefore be considered as having an energy independent of q.

2.3.1 PHONONS AND THE SUBSTRATE

Unlike other semiconductors, for which epitaxial growth is performed on substrates of the same material, the growth of GaN is not performed on GaN substrates. The popular choice of substrate is sapphire, although growth of gallium nitride substrates remains an active area of research. The use of a sapphire substrate introduces an added complication during analysis of results. Phonons must traverse the substrate to reach the detector. The substrate is typically 200 times thicker than the epilayers, and its effects cannot be ignored.

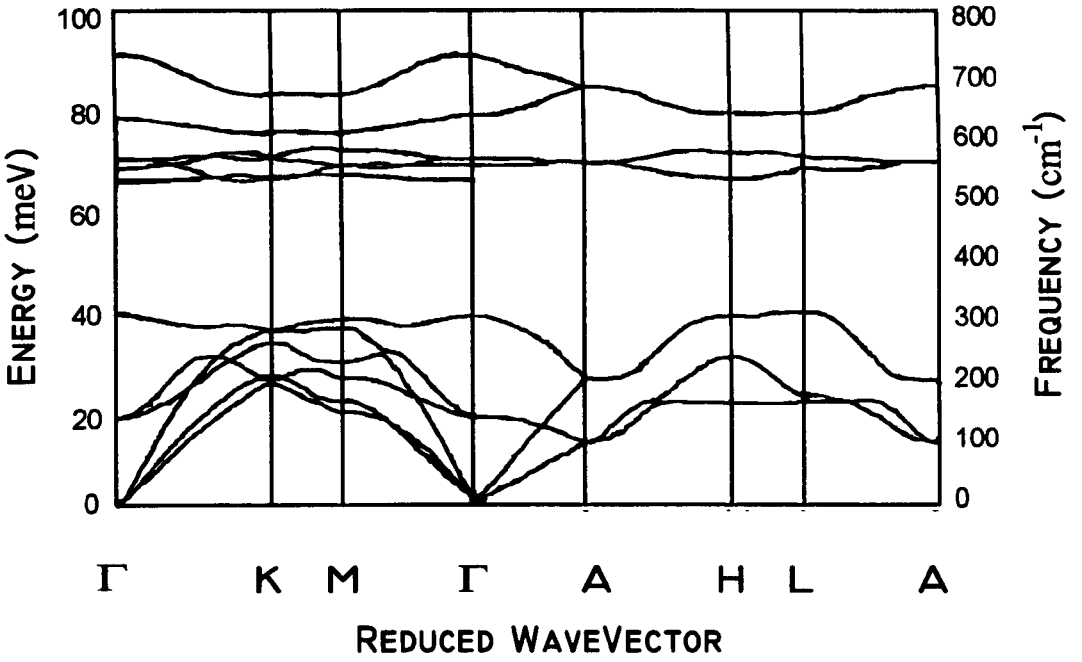

Figure 2.1: The dispersion curves for wurtzite GaN.

2.3.2 ISOTOPE MASS SCATTERING

Phonons will scatter off any departure from periodicity in the lattice. Impurities, defects and other phonons will all cause scattering. The strength of scattering depends on the nature of the scatterer and their density. In high quality crystals, impurity and defect scattering will be minimal. In GaN however, where the defect density is typically of the order $\sim 10^8 cm^{-3}$ for epitaxial growth, defects can be expected to play a role in determining the nature of phonon propagation. The sapphire substrates used in growth are of a high crystal quality. An intrinsic departure from strict periodicity will arise due to isotopic mass variations. In GaAs epilayers on GaAs substrates, this effect must be considered. If the natural isotopic abundance of the constituent elements of the system are considered, it is clear that the only real departure will be caused by gallium atoms (^{69}Ga$\sim$60% and ^{71}Ga$\sim$40%). Isotopic mass scattering will affect the propagation of high frequency phonons. At what frequency this effect becomes important can be calculated by considering scattering cross sections and attenuation of flux, an

approach first suggested by Morse and Feshbach [4]. In GaN however, this effect need not be considered, as the epilayer is thin when compared to the substrate, and isotope mass scattering in the substrate need not be considered.

2.3.3 THE ROLE OF INTERFACES

When the substrate and epilayer are of the same material, it is assumed that almost perfect lattice matching is achieved. In GaN growth, this is not the case; sapphire has a lattice mismatch of ~16%. This does not only complicate the initial stages of growth but also introduces strain and dislocations into the material of interest. It is interesting to note that there are, albeit sometimes contradictory, views that dislocations provide the means for wet chemical etching of the material. The behaviour of dislocations in GaN is an active area of study [5] – [10].

As will be discussed in Chapters 3 and 4, generation and detection of phonons generally involves the use of thin metal films deposited onto the sample. The quality of the interface (hence degree of contact) between the two materials can have a pronounced effect on phonon propagation. This is also true of the GaN/sapphire interface, where interface roughness scattering can occur when the roughness is of the order of the phonon wavelength. Scattering and mode conversion at interfaces must all be considered.

The transmission of phonons across interfaces is described by acoustic mismatch theory (see, for example, [11], [12]). When the match between epitaxial layer and substrate is not perfect, numerical calculation of the thermal flux across the boundary is required, which takes into account the different densities, phonon velocities and transmission coefficients of the two materials.

2.3.4 PHONON GENERATION

Phonons generated by excitation of a thin metal film have a spectral distribution which is assumed to be Planckian. Transmission of phonons generated in the film

is described by acoustic mismatch theory. It is assumed that transport across the interface is frequency independent. It is possible to calculate the temperature in the film using

$$\frac{P}{A} = \alpha_{eff}(T_h^4 - T_\ell^4) \tag{2.3.2}$$

where P is the power input to the film (calculated using V_H^2/R), A is the area of the heater and T_h and T_ℓ are the heater temperature and lattice temperature respectively. The effect of the interface enters via α_{eff}, the modified Stefan constant. For constantan on sapphire, a system extensively studied in the early days of phonon imaging, α_{eff}=56 $Wm^{-2}K^{-4}$ [13].

The energy distribution of emitted phonons is given by

$$E(\omega) = \frac{\hbar\omega^3}{2\pi^2}\left(\frac{2}{v_{TA}^3} + \frac{1}{v_{LA}^3}\right)\frac{1}{exp\left(\frac{\hbar\omega}{k_BT}\right) - 1} \tag{2.3.3}$$

where v_{TA} and v_{LA} are the transverse and longitudinal velocities respectively.

The peak in the blackbody spectrum occurs at $\sim 3k_BT_h$, and so by knowing the heater temperature, the wavevector at which the peak in the spectrum occurs can be calculated.

2.3.5 PHONON FOCUSSING

In an isotropic system, the elastic properties of the crystal are independent of direction. In this case, acoustic wave propagation would produce spherical wavefronts and the group velocity and wavevector would be collinear. In reality, the elastic properties of crystals are direction dependent. This anisotropy means that the phase velocity of phonons is different for different crystal directions and for different modes. The group velocity and wavevector are no longer parallel, except along certain crystal directions of high symmetry. This effect is known as phonon focussing (see [14] for a comprehensive description).

Phonon focussing in GaAs, with its cubic symmetry, has been extensively studied. In wurtzite GaN, with hexagonal symmetry, the effects of focussing are

more difficult to see, due to the lack of a GaN substrate. Any effects due to the GaN epilayer must be inferred from comparison with sapphire focussing patterns (including the effect of the interface). A study of focussing in sapphire can be found in the early work of von Gutfeld [11], Every, Koos and Wolfe [15], and in numerous other works by Every, e.g. [16], [17]. Detailed theoretical descriptions of focussing effects in cubic systems are in abundance in the literature. Only an outline of the method is presented here.

In a real crystal, elasticity is described by a fourth rank tensor which relates stress and strain, both second rank tensors in a generalised form of Hooke's law Equation 2.3.4.

$$\sigma_{ij} = C_{ij\ell m} e_{\ell m} \tag{2.3.4}$$

where $C_{ij\ell m}$ are the elements of the elastic tensor.

The fractional change in displacement of a volume element displaced by a distance u is given by Equation 2.3.5.

$$e_{\ell m} = \frac{1}{2}\left(\frac{\partial u_\ell}{\partial x_m} + \frac{\partial u_m}{\partial x_\ell}\right) \tag{2.3.5}$$

The equations of motion are given by Equation 2.3.6

$$\rho \frac{\partial^2 u_i}{\partial t^2} = \frac{\partial \sigma_{ij}}{\partial x_j} \tag{2.3.6}$$

where ρ is the density of the medium.

Making the necessary summations and assuming plane wave solutions of the form $\mathbf{u} = \mathbf{U}e^{i(\mathbf{k}.\mathbf{x}-\omega t)}$ yields the Christoffel equation, Equation 2.3.7.

$$\left[D_{ij} - \rho v_P^2 \delta_{ij}\right] e_\ell = 0 \tag{2.3.7}$$

where D_{ij} are the Christoffel coefficients, equal to $C_{ij\ell m} n_j n_m$ and v_P is the phase velocity. The wave normal is given by $\mathbf{n} = \mathbf{k}/k$.

Evaluation of the Christoffel equation is necessary to obtain the phase and group velocities. From manipulation of the equations it is possible to produce

a plot of constant frequency surfaces in k–space for the different phonon polarisations. This is called a "slowness surface" and is a useful representation of the effects of acoustic anisotropy since the curvature of this surface shows the extent of focussing. The group velocity, and so the energy flux, is normal to this surface and strong enhancement of energy flux will be observed where the surface is flat.

Solution of the Christoffel equations requires knowledge of the elastic constants of the material, which can be represented in a 6×6 matrix. In cubic crystals, there are only three non–zero elements. In wurtzite GaN, this number is increased to five. The situation is further complicated in non-centrosymmetric crystals due to internal strain fields. This leads to a correction of the elastic coefficients $C_{ij\ell m}$ and is termed piezoelectric stiffening. In cubic systems there is one independent piezoelectric constant, whereas is GaN there are three.

Sapphire is of trigonal symmetry, further complicating matters. The average sound velocities for sapphire and GaN are shown in Table 2.1. Theoretical focussing patterns for sapphire are shown in Figures 2.2 and 2.3, using the Monte Carlo simulation developed by Northrop based on the theory of A.G.Every [18].

	Mode	Velocity (ms^{-1})
Sapphire	LA	11 100
	TA	6040
GaN	LA	6560
	TA	2680

Table 2.1: The velocities of acoustic phonons in sapphire and GaN

2.4 THE ELECTRON–PHONON INTERACTIOI

As was mentioned in Section 2.3.1, deviations from ideality in the crystal cause phonon scattering. The presence of phonons in the system scatters electrons. There are two mechanisms by which phonons can interact with electrons; deformation potential coupling and piezoelectric coupling.

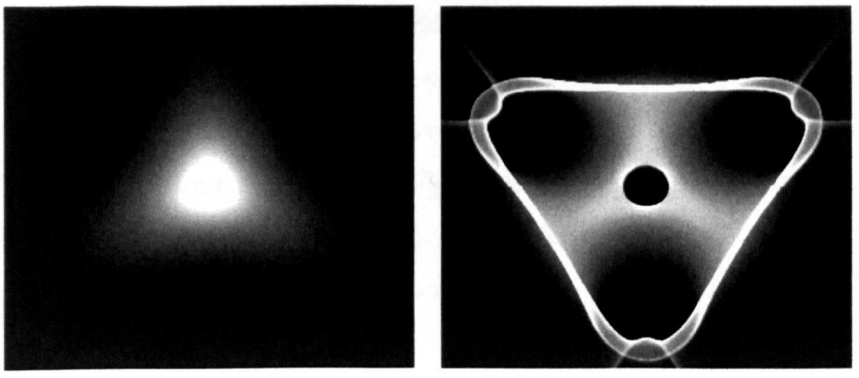

Figure 2.2: Theoretical phonon focussing patterns for sapphire. Left: The results of the Monte Carlo simulation for the longitudinal mode. Right: The fast transverse mode.

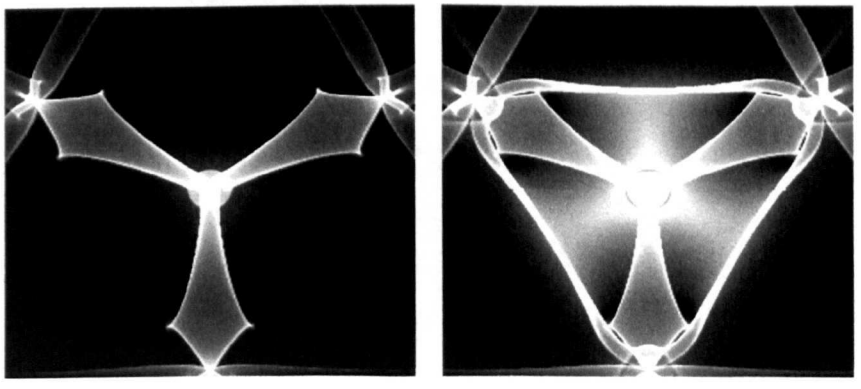

Figure 2.3: Theoretical phonon focussing patterns for sapphire. Left: The results of the Monte Carlo simulation for the slow transverse mode. Right: Both TA modes.

2.4.1 DEFORMATION POTENTIAL COUPLING

When a phonon propagates through the lattice, it produces a periodic fluctuation of the lattice constant which shifts the conduction and valence bands. These variations give rise to an effective potential capable of interacting with electrons. The deformation potential is proportional to the dilation of the lattice, which can be expressed in terms of the displacement due to the passage of a phonon. The displacement vector is obtained from elastic theory, Equation 2.4.1.

$$\mathbf{U}(\mathbf{r}) = \left(\frac{\hbar}{2\rho V \omega_{(q)}}\right)^{\frac{1}{2}} \lambda[a_{(q,\lambda)}e^{i\mathbf{q}.\mathbf{r}} + a^{\dagger}_{(q,\lambda)}e^{-i\mathbf{q}.\mathbf{r}}] \tag{2.4.1}$$

where V is the volume, λ is the polarisation vector and a and $a^{\dagger}$ are phonon annihilation and creation operators respectively.

In a semiconductor with a single parabolic band, the coupling potential is given by $V_{def} = \Xi_d \nabla.U(r)$, and so the expression for the deformation potential is given by Equation 2.4.2.

$$V_{def} = \left(\frac{\hbar}{2\rho V \omega_{(q)}}\right)^{\frac{1}{2}} - i\Xi_d \, \mathbf{q}.\lambda \, [a_{(q,\lambda)}e^{i\mathbf{q}.\mathbf{r}} + a^{\dagger}_{(q,\lambda)}e^{-i\mathbf{q}.\mathbf{r}}] \tag{2.4.2}$$

where Ξ_d is the deformation potential coupling constant.

The dot product in Equation 2.4.2 indicates that this mechanism of coupling is only possible in LA modes, where the polarisation vector and wavevector are collinear. In real crystals phonon modes are not "pure" LA or TA, and so deformation potential coupling is possible with TA modes also.

2.4.2 PIEZOELECTRIC COUPLING

Crystals which lack a centre of inversion symmetry are termed piezoelectric. An electric field is produced when strain is applied to the crystal, as occurs when phonons cause a distortion of the lattice. This electric field can then couple to the lattice. The relationship between the strain, S, and the electric field is given

by ([19])

$$\varepsilon_{lm} E_m = e_{\ell mn} S_{mn} \tag{2.4.3}$$

where ε is the dielectric tensor and $e_{\ell mn}$ are components of the piezoelectric tensor.

From elasticity theory, the strain is related to the lattice distortion $U(r)$ by

$$S_{mn} = \frac{1}{2}\left(\frac{\hbar}{2\rho V \omega_{(q)}}\right)^{\frac{1}{2}} [a_{(q,\lambda)} e^{i\mathbf{q}.\mathbf{r}} + a^{\dagger}_{(q,\lambda)} e^{-i\mathbf{q}.\mathbf{r}}](\lambda_m q_n + \lambda_n q_m) \tag{2.4.4}$$

The coupling potential V_{PZ} can be found using the preceding equations and by noting that $E_m = -\nabla V(r) = i q_m V_q e^{-iq.r}$.

2.4.3 SCREENING

Screening occurs in any system where charged particles are free to move. The effect is to modify the electron–phonon interaction potential. Screening will be discussed here only briefly, with more detail discussed in relation to the experimental results.

The Thomas–Fermi approximation, assuming static screening, is the simplest model. It is assumed that the variation in potential is very slow on length scales comparable to the electron wavelength. The Thomas–Fermi approach considers long wavelengths, and is a good approximation in most situations. The total potential is of Coulombic form with an exponential damping term. The distance over which this screening is effective can be calculated. At distances greater than the screening length, this potential becomes negligible.

The situation becomes more complex when higher energies and electron densities are considered. As previously discussed, the interaction between electrons and optical modes presents new possibilities for energy relaxation, and a dynamic screening model should be employed. Dynamic screening and the collective motion of the electrons become intertwined at high electron densities, where the optic

frequency is comparable to and in some cases larger than the plasmon frequency. (For an optic phonon of 92meV, for $\omega_p > \omega_{LO}$, the carrier density required is $\sim 2 \times 10^{25} \mathrm{m}^{-3}$). The Lindhard screening model essentially adds a correction term to the Thomas–Fermi approximation, and at high electron densities should be more applicable. In the low wavelength regime, the Lindhard model reduces to the Thomas-Fermi approximation.

2.4.4 EMISSION OF ACOUSTIC PHONONS

When electrons are heated above the equilibrium lattice temperature, they relax by imparting their excess energy to the lattice. At low temperatures, emission of acoustic phonons is the dominant relaxation mechanism. As the temperature is increased, the electrons are capable of emitting higher energy phonons with larger wavevectors. Which coupling mechanism dominates the emission of acoustic phonons is determined by considering the different q dependencies of the interactions and the coupling constants. At higher temperatures still, electrons have enough energy that emission of optic phonons is possible, and this pathway eventually dominates the energy relaxation rate. This Section will consider these emission processes in detail for both 3D and 2D systems.

THE MATHEMATICAL DESCRIPTION OF ACOUSTIC PHONON EMISSION

Phonon emission has been studied by a number of authors (for example [20]– [22]). A detailed discussion can be found in Jasiukiewicz and Karpus [23], [24].

When an electron emits an acoustic phonon, it is scattered from its initial state $\mathbf{k}$ into a new state $\mathbf{k}'$ such that $\mathbf{k} = \mathbf{k}' + \mathbf{q}$, where $\mathbf{q}$ is the wavevector of the emitted phonon.

The energy relaxation rate $P_{(q,\lambda)}$ into a phonon mode is given by Equa-

tion 2.4.5.

$$P_{(q,\lambda)} = \hbar\omega_{(q,\lambda)}\Lambda_k^{(q,\lambda)} \tag{2.4.5}$$

where $\hbar\omega_{(q,\lambda)}$ is the energy of the phonon, $\Lambda_k^{(q,\lambda)}$ is the phonon emission rate, and the subscripts q and λ represent the phonon wavevector and polarisation respectively.

The net phonon emission rate comprises contributions from phonon absorption and phonon emission, both spontaneous and stimulated and is given by Equation 2.4.6.

$$\Lambda_k^{(q,\lambda)} = \sum_{k,k'}(f_k(1-f_{k'})n_{(q,\lambda)}(T_\ell)W_k^{k'} + f_k(1-f_{k'})W_k^{k'} - (f_{k'}(1-f_k)n_{(q,\lambda)}(T_\ell)W_{k'}^{k}) \tag{2.4.6}$$

where n_q is the Bose–Einstein occupation number (as given in Equation 2.3.1), f_k and $f_{k'}$ are the electron distribution functions (giving the probability of occupation of states) and $W_k^{k'}$ and $W_{k'}^{k}$ are the transition probabilities for emission and absorption processes respectively.

The electron distribution is described by the Fermi–Dirac function, Equation 2.4.7.

$$f_k^{T_e} = \frac{1}{e^{\frac{-(E_F-E_k)}{k_B T_e}} + 1} \tag{2.4.7}$$

where $E_k = \hbar^2k^2/2m_e$. This assumes that electron–electron scattering occurs much faster than electron–phonon scattering, hence the electron gas is in equilibrium with itself but not the lattice.

The second term in the sum in Equation 2.4.6 represents spontaneous phonon emission and is independent of the phonon occupation number. The transition probabilities for emission and absorption are equal, and so Equation 2.4.6 simplifies to

$$\Lambda_k^{(q,\lambda)} = \sum_{k,k'} W_k^{k'}(f_k(1-f_{k'})(n_{(q,\lambda)}(T_\ell)+1) - f_{k'}(1-f_k)n_{(q,\lambda)}(T_\ell)) \tag{2.4.8}$$

When the system is in equilibrium, there is no net emission of phonons; in this case $T_e = T_\ell$. Substituting into Equation 2.4.8 reduces to

$$\Lambda_k^{(q,\lambda)} = \sum_{k,k'} (n_{(q,\lambda)}(T_e) - n_{(q,\lambda)}(T_\ell))(f_{k'} - f_k) W_k^{k'} \tag{2.4.9}$$

The transition probability $W_k^{k'}$ is calculated using Fermi's golden rule, Equation 2.4.10.

$$W_k^{k'} = \frac{2\pi}{\hbar} |M|^2 \delta(E_k - E_{k'} - \hbar\omega_{(q,\lambda)}) \tag{2.4.10}$$

where the δ–function is a statement of energy conservation and M is the matrix element of the electron–phonon interaction, given by Equation 2.4.11.

$$M = < k' | V_{e-p} | k > \tag{2.4.11}$$

where $|V_{e-p}|$ is the electron–phonon interaction potential, as described in Section Equation 2.4.

Substitution of Equations 2.4.10 and 2.4.9 into Equation 2.4.5 yields the energy relaxation rate into a phonon mode described by its wavevector q and polarisation λ, as given in Equation 2.4.12.

$$P_{(q,\lambda)} = 2\pi\,\omega_{(q,\lambda)}(n_{(q,\lambda)}(T_e) - n_{(q,\lambda)}(T_\ell)) \sum_{k,k'} (f_{k'} - f_k) |M|^2 \delta(E_k - E_{k'} - \hbar\omega_{(q,\lambda)}) \tag{2.4.12}$$

Up to this point, no assumptions about the nature of the electron system or crystal structure have been made; these equations are valid for all systems. Evaluation of the matrix element term requires knowledge of the system of study.

To obtain the total power dissipated due to phonon emission it is necessary to integrate over all phonon wavevectors and sum over all modes,

$$P_e = \sum_\lambda \int d\Omega \int dq\, P_{(q,\lambda)} \frac{q^2 V}{(2\pi)^3} \tag{2.4.13}$$

where the element of solid angle into which phonons are emitted,$d\Omega$, is given by

$$d\Omega = 2 \int_0^{\frac{\pi}{2}} \int_0^{2\pi} \sin\theta\, d\theta\, d\phi \tag{2.4.14}$$

EMISSION IN 3D SYSTEMS

The piezoelectric matrix elements for a 3D system are given by

$$|M|^2 = \frac{\hbar C_{-1}^2}{2V\rho v_s q}\delta_{k,k'+q} \tag{2.4.15}$$

where C_{-1} is the directionally averaged piezoelectric coupling constant.

The wurtzite crystal structure of GaN leads to three independent piezoelectric parameters and the directionally averaged coupling constant is given by ([19]),

$$C_{-1}^2 = \left(\frac{e}{\varepsilon}\right)^2 \frac{1}{6}\left\{\frac{4}{3}(e_{31} + \frac{3}{4}e_{33} + 2e_{15})^2 + \frac{7}{4}e_{33}^2\right\} \tag{2.4.16}$$

for coupling to longitudinal phonons and

$$C_{-1}^2 = \left(\frac{e}{\varepsilon}\right)^2 \frac{1}{8}\left\{(e_{31} - e_{33} - \frac{1}{3}e_{15})^2 + \frac{56}{9}e_{15}^2\right\} \tag{2.4.17}$$

for coupling to transverse phonons.

For coupling via the deformation potential,

$$|M|^2 = \frac{\hbar C_{+1}^2 q}{2V\rho v_s}\delta_{k,k'+q} \tag{2.4.18}$$

where $C_{+1} = \Xi_d = 8.3\text{eV}$ [25].

In 3D electron systems, the power loss per electron into a given mode λ is given by

$$P_e = \frac{3m^* C_\gamma^2 v_s k_F^{\gamma+1}}{4\pi\rho\hbar^2}\left(\frac{k_B T_e}{\hbar v_s k_F}\right)^{\gamma+4} \times \int_0^{x_{max}} x^{\gamma+1}dx\left(\frac{1}{e^x - 1} - \frac{1}{e^{x(T_e/T_l)} - 1}\right)\left(\frac{1}{1 + \frac{s^2}{x^2}}\right)^2 \tag{2.4.19}$$

with γ equal to $+1$ for deformation potential coupling and γ equal to -1 for piezoelectric coupling.

The integration parameter x is given by

$$x = \frac{\hbar v_s q}{k_B T_e} \tag{2.4.20}$$

In the upper limit of the integral in Equation 2.4.19, the maximum wavevector phonon that can be emitted is given by $q = 2k_F$.

The effect of screening of the interaction is incorporated through the screening parameter, given by

$$s = \frac{\hbar v_s \lambda_D}{k_B T_e} \tag{2.4.21}$$

where λ_D is the inverse Debye screening length, given by

$$\lambda_D = \frac{e}{\pi\hbar}\sqrt{\frac{m^* k_F}{2\varepsilon}} \tag{2.4.22}$$

All other symbols take their usual meanings.

The evaluation of Equation 2.4.19 is performed numerically, and assumes that the crystal is isotropic.

EMISSION IN 2D SYSTEMS

The piezoelectric matrix elements for a 2D system are given by

$$|M|^2 = \frac{\hbar C_{-1}^2}{2\rho V \omega_{q,\lambda}} |F(q_z)|^2 \delta_{k,k'+q_{||}} \tag{2.4.23}$$

and for the deformation potential,

$$|M|^2 = \frac{\hbar C_{+1}^2 q}{2V\rho v_s} |F(q_z)|^2 \delta_{k,k'+q} \tag{2.4.24}$$

$F(q_z)$ is the bound state form factor, given by

$$|F(q_z)|^2 = \frac{1}{(1+q_z^2 a_0^2)^3} \tag{2.4.25}$$

where a_0 is the Fang–Howard parameter.

The presence of the form factor, $|F(q)|$, introduces another cut–off in the allowed values of q, which can be seen by considering the uncertainty principle,

which states

$$\Delta p_z \sim \frac{\hbar}{\Delta z} \tag{2.4.26}$$

When a phonon is emitted (or absorbed), the change in momentum is given by $\Delta p_z = \hbar q_z$ and so $q_{z_{MAX}} \sim \frac{1}{\Delta z}$. The thickness of the 2DEG sheet is given by the Fang–Howard parameter, a_0, and therefore

$$\Delta q_z \sim \frac{1}{a_0} \tag{2.4.27}$$

This effectively limits the maximum wavevector phonon that can be emitted such that the interaction is cut off for phonons with wavevectors $q_z \geq 1/a_0$.

The power loss per electron into a given mode λ in 2D systems is given by

$$P_e = 2\int_0^{\frac{\pi}{2}} d\theta \int_0^{\infty} \frac{m^{*3/2} C_\gamma^2 S^2 |F(q)|^2 \omega^{\gamma+2}}{4\sqrt{2}\pi^3 \rho \hbar^2 v_s^{\gamma+3}} \left(\frac{1}{e^x - 1} - \frac{1}{e^{x(T_e/T_l)} - 1}\right) \int_{E_o}^{\infty} \frac{f_{E'} - f_E dE}{\sqrt{(E - E_o)}} \tag{2.4.28}$$

where f_E is the electron distribution function (as in Equation 2.4.7) and E_o is given by

$$E_o = \left(\frac{sin^2\theta}{2m^* v_s^2}\right)\left[\frac{\hbar\omega}{2} + \frac{m^* v_s^2}{sin^2\theta}\right]^2 \tag{2.4.29}$$

and all other symbols have their usual meanings.

In 2D systems, the quasi–static screening parameter is given by

$$S = \left(\frac{r_s q_{||}}{1 + r_s q_{||}}\right) \tag{2.4.30}$$

where $q_{||} = qsin\theta$, the component of q parallel to the 2DEG, θ is the angle between the phonon wavevector and the 2DEG normal and $r_s = 2\pi\varepsilon\hbar^2 m^* e^2$ is the Thomas–Fermi screening radius.

The coupling constant is given by

$$C_{-1} = \left(\frac{e_{15}(q_x^2 + q_y^2)\lambda_z + e_{33}q_z^2\lambda_z + (e_{15} + e_{31})q_z(q_x\lambda_x + q_y\lambda_y)}{\varepsilon_{11}(q_x^2 + q_y^2) + \varepsilon_{33}q_z^2} \right)^2 \tag{2.4.31}$$

In the calculation of power loss in a 3D system, it was appropriate to directionally average the piezoelectric coupling constant. In 2D systems, because of the θ dependence of $q_{||}$, it is only appropriate to average over ϕ. The polarisation term can be evaluated for each mode separately and expressed in terms of θ only allowing the angular dependence of emitted power for each mode to be calculated. The piezoelectric coupling constants for each mode are given below.

$$C_{-1}^{LA} = \frac{\cos^2\theta(e_{31}\sin^2\theta + 2e_{15}\sin^2\theta + e_{33}\cos^2\theta)}{(\varepsilon_{11}\sin^2\theta + \varepsilon_{33}\cos^2\theta)^2} \tag{2.4.32}$$

$$C_{-1}^{TA(IN)} = \frac{1}{2}\frac{\cos^2\theta\sin^4\theta(e_{15} + e_{31})^2}{(\varepsilon_{11}\sin^2\theta + \varepsilon_{33}\cos^2\theta)^2} \tag{2.4.33}$$

$$C_{-1}^{TA(OUT)} = \frac{\sin^2\theta(e_{15}\cos^2\theta + e_{31}\cos^2\theta + e_{15}\sin^2\theta + e_{33}\cos^2\theta)}{(\varepsilon_{11}\sin^2\theta + \varepsilon_{33}\cos^2\theta)^2} \tag{2.4.34}$$

where the labels "$TA(OUT)$" and "$TA(IN)$" correspond to phonon polarisation out of plane (of the 2DEG) and parallel to the 2DEG.

2.4.5 EMISSION OF OPTIC PHONONS

At high electron temperatures, electrons are capable of relaxing their energy via the emission of optic phonons. The only electrons which can emit optic phonons are those with an energy greater than $\hbar\omega_{LO}$, and so it is only electrons in the tail of the Fermi distribution which can relax by this mechanism.

It is assumed that the electrons are in thermal equilibrium with one another and that the lattice is also in equilibrium. It is also assumed that LO phonons are dispersionless. A detailed discussion can be found in [26] and [27]. More thorough

treatments can be found in, for example, [28] - [32], although these treatments are more complicated than is required for the experiments and analysis performed in this study. Only an outline of the method is presented here.

Ignoring re–absorption of phonons, the power loss of an electron to an LO phonon is given by Equation 2.4.35.

$$P = \frac{2\pi}{\hbar} \sum_{k,k'} \hbar\omega_{LO} |M|^2 \delta(E_K - E_{k'} - \hbar\omega_{LO}) \tag{2.4.35}$$

where all symbols have their usual meanings.

In this case, the electron–phonon matrix element $|M|^2$ is given by Equation 2.4.36.

$$|M|^2 = \frac{4\pi\alpha(\hbar\omega_{LO})^{\frac{3}{2}}}{\sqrt{2m^*}} \frac{1}{q^2} \tag{2.4.36}$$

where m^* is the electron effective mass and α is the Fröhlich coupling constant, given by Equation 2.4.37.

$$\alpha = \frac{e^2}{4\pi\hbar} \sqrt{\frac{m^*}{2\hbar\omega_{LO}}} \left(\frac{1}{\varepsilon_\infty} - \frac{1}{\varepsilon_s} \right) \tag{2.4.37}$$

where ε_∞ and ε_s are the high frequency and static dielectric constants respectively.

Substitution into Equation 2.4.36 simplifies the matrix element to Equation 2.4.38.

$$|M_k^{k'}|^2 = \frac{1}{q^2} \frac{e^2\hbar\omega_{LO}}{2} \left(\frac{1}{\varepsilon_\infty} - \frac{1}{\varepsilon_s} \right) \tag{2.4.38}$$

Summing over all phonon wavevectors leads to Equation 2.4.39.

$$P = 2\frac{(\hbar\omega_{LO})^{\frac{5}{2}}\alpha}{\hbar} \frac{1}{\sqrt{E}} \sinh^{-1} \left[\left(\frac{E}{\hbar\omega_{LO}} - 1 \right)^{\frac{1}{2}} \right] \tag{2.4.39}$$

Assuming a Maxwell–Boltzmann distribution of electrons, the power loss per electron is given by Equation 2.4.40.

$$P = \frac{4(\hbar\omega_{LO})^{\frac{5}{2}}\alpha\beta^{\frac{3}{2}}}{\sqrt{\pi}\hbar} \int_{\hbar\omega_{LO}}^{\infty} dE \sinh^{-1} \left[\left(\frac{E}{\hbar\omega_{LO}} - 1 \right)^{\frac{1}{2}} \right] e^{-\beta E} \tag{2.4.40}$$

where β is given by $1/k_BT$.

If the only temperatures to be considered are those for which $\hbar\omega_{LO} \gg k_BT$, then the integrand can be expanded and in powers of $k_BT/\hbar\omega_{LO}$ and Equation 2.4.40 simplifies to the well known "phenomenological" expression for power loss due to optic phonon emission, Equation 2.4.41.

$$P_e = \frac{\hbar\omega_{LO}}{\tau} exp\left(\frac{-\hbar\omega_{LO}}{k_BT_e}\right) \tag{2.4.41}$$

where τ is the electron–phonon scattering time given by Equation 2.4.42.

$$\tau = \frac{1}{2\alpha\omega_{LO}} \tag{2.4.42}$$

So assuming one phonon processes and emission to bare LO phonons only, the final expression for power loss is quite straightforward. In reality, optic phonons have a finite lifetime and a small group velocity, and so there is possibility of the phonon being reabsorbed. At high temperatures, "hot phonon" effects may be evident, where the energy relaxation rate is reduced. This can be observed as an increase in the effective scattering time – as the electron temperature is further increased, the value of τ approaches the down–conversion time.

Another possible mechanism of energy relaxation is through emission of coupled LO–plasmon modes. Possible evidence of energy loss via this route has been observed experimentally in GaAs and also in GaN systems studied using Raman techniques, and occurs when the plasma frequency is comparable to the optic phonon frequency (see, for example, [33]). Plasmons are collective excitations of the electron gas. Electrons in the bottom of the conduction band move through a relatively immobile background of positively charged ions. On average, neutrality prevails, but when fluctuations in electron density do occur, strong electric fields appear which attempt to restore neutrality but only succeed in producing oscillations, termed plasma oscillations. These oscillations can couple to the lattice, resulting in LO–plasmon modes. The uncoupled plasma frequency, ω_P, is given by Equation 2.4.43.

$$\omega_p^2 = \sqrt{\frac{Ne^2}{m^*\varepsilon_\infty}} \tag{2.4.43}$$

Because the plasma frequency is dependent on the carrier density, energy loss into LO–plasmon coupled modes should also exhibit a density dependence. Following the argument of Das Sarma [34], it can be shown that even though the phonon spectral weight in the plasmon–like mode is small, it can significantly modify the power loss.

Power is distributed into two channels, as shown in Equation 2.4.44.

$$P = \hbar\omega_+ C_+ exp\left(\frac{-\hbar\omega_+ C_+}{k_B T}\right) + \hbar\omega_- C_- exp\left(\frac{-\hbar\omega_- C_-}{k_B T}\right) \tag{2.4.44}$$

where C_+ and C_- are factors which depend on the phonon spectral weight at the two frequencies.

In considering plasmon–LO phonon coupled modes, the matrix element as given by Equation 2.4.38 is modified, and so the two extremes of behaviour are seen by considering the carrier density. When the electron density is high, $\omega_+ \sim \omega_p$ and $\omega_- \sim \omega_{LO}$. In this case, $C_+ \ll C_-$ and most of the energy is dissipated in the LO–like mode. At lower densities, the reverse situation is true (i.e. $\omega_+ \sim \omega_{LO}$ and $\omega_- \sim \omega_p$ and $C_+ \gg C_-$) and although the prefactor favours emission via the LO–like mode, the exponential term favours the plasmon–like mode. At higher temperatures, the exponential terms "even out" and the LO mode is again dominant.

To observe emission via coupled modes experimentally, the change from phonon–like to plasmon–like emission would have to occur at a temperature high enough that the contribution from emission into acoustic modes was small. The effect of the coupled modes should be evident in the "abruptness" of the crossover from acoustic to optic emission as the electron density reduces (with a more gradual crossover occurring at higher densities).

2.4.6 DECAY OF OPTIC PHONONS

As previously discussed (see Section 2.3), optic phonons are considered to be dispersionless and have a small group velocity and finite lifetime. When electrons

lose energy by optic phonon emission, the optic phonons decay and energy is dissipated. In GaAs, optic phonons quickly decay into to two LA phonons, which can themselves be down converted into lower energy modes. The decay of optic phonons in GaN cannot follow this "normal" three phonon process because the zone centre frequency is too high ($2\omega_{LA} < \omega_{LO}$). Decay by four phonon processes is energetically allowed, although the lifetime would be long and hot phonon effects pronounced. In GaN, there exist two possible decay routes [35];

$$LO \rightarrow TO + LA$$
$$LO \rightarrow TO + TA$$

It is necessary for the acoustic phonon to have a large wavevector to satisfy energy constraints. The favoured route is decay into an LA mode, followed by further down–conversion into TA modes. This is because TA emission may not be possible in all crystal directions. Conservation of crystal momentum in normal processes means the emitted phonons move in opposite directions, and the polarisation vectors of the emitted phonons must be mutually perpendicular. This is easier to achieve by LA emission with the TO mode polarised normal to the plane. Both TO and LO modes are essentially dispersionless and so the effects of non–equilibrium phonons will be of importance under conditions of high carrier density and high temperatures.

2.4.7 THE MATHEMATICAL DESCRIPTION OF ACOUSTIC PHONON ABSORPTION

Absorption of acoustic phonons can take place in a manner analogous to emission, but characterised by $\mathbf{k}' = \mathbf{k} + \mathbf{q}$. In absorption, a beam of phonons with wavevector q are incident on the electron gas, with a temperature T_e. The electrons are in equilibrium with the lattice, $T_{e(eq)} = T_\ell$. Absorption of phonons raises the electron temperature, and the electron gas is described by a temperature $T_e = T_{e(eq)} + \Delta T$. If $\Delta T \ll T_{e(eq)}$, then it is reasonable to consider that $\Delta T \sim P_{abs}$. An outline of the formal theory is given below.

Incident phonons create an excess population of phonons in a mode q such that

$$N_q = N_q(T_e) + \Delta N_q \tag{2.4.45}$$

The net power incident on the electron gas due to the incident phonons is given by Equation 2.4.46.

$$P_{inc} = A\,\hbar\omega\,v_s\cos\theta\left(\frac{\Delta N_q}{V}\right) \tag{2.4.46}$$

where θ is the angle of incidence of the phonons. All other symbols have their usual meanings.

The rate of energy absorption from the mode due to the electron–phonon interaction is given by Equation 2.4.47.

$$R_{abs} = -\hbar\omega\frac{dN_q}{dt} \tag{2.4.47}$$

Using Equations 2.4.46 and 2.4.47 allows the fractional absorption of a mode, α_{abs}, to be determined.

$$\alpha_{abs} = \frac{R_{abs}}{P_{inc}} = \frac{V}{A\,v_s\cos\theta\,\Delta N_q}\frac{1}{}\frac{dN_q}{dt} \tag{2.4.48}$$

Fermi's golden rule is applied to determine the scattering rate, given by Equation 2.4.49.

$$\frac{dN_q}{dt} = \sum_{k,k'} f_k(1-f_{k'})(N_{(q,\lambda)}+1)W_k^{k'} - f_{k'}(1-f_k)N_{(q,\lambda)}W_{k'}^{k} \tag{2.4.49}$$

If only absorption processes are considered, then the transition probability is given by Equation 2.4.50.

$$W_{k'}^{k} = \frac{2\pi}{\hbar}|M|^2\,\delta(E_k - E_{k'} + \hbar\omega_{q,\lambda}) \tag{2.4.50}$$

where all symbols have their usual meanings (the matrix elements are as given in Equations 2.4.15 and 2.4.18).

To calculate the total fractional absorption requires summing over all phonon modes and frequencies, as shown in Equation 2.4.51.

$$\alpha = \frac{\sum \hbar\omega \, \Delta N_q \Gamma}{\sum \hbar\omega \, v_s \cos\theta \Delta N_q} \tag{2.4.51}$$

where Γ is given by

$$\Gamma = \sum (f_{k'} - f_k) W_k^{k'} \tag{2.4.52}$$

To calculate the total fractional absorption precisely, this expression must be evaluated numerically.

It is possible however, to obtain analytic expressions for the scattering rates if the exact nature of the phonon spectrum is not considered explicitly.

The situation can be reasonably approximated by assuming that

$$\frac{dN_q}{dt} = \frac{1}{\tau} N_q \tag{2.4.53}$$

where τ is the phonon scattering time.

It is then possible to simplify further by working in the limit of high energy, such that the phonon wavevector q is equal to $2k_F$.

Then, Equation 2.4.53 can be written as

$$\frac{1}{\tau} = \frac{\pi C_{+1}^2 \, q}{V \rho \, v_{sL}} \sum_{k,k'} \delta_{\mathbf{k},\mathbf{k'}+\mathbf{q}} \, \delta(E_k - E_{k'} + \hbar\omega) \tag{2.4.54}$$

for deformation potential coupling and

$$\frac{1}{\tau} = \frac{\pi \, C_{-1}^2}{V \rho \, v_{sT} \, q} \sum_{k,k'} \delta_{\mathbf{k},\mathbf{k'}+\mathbf{q}} \, \delta(E_k - E_{k'} + \hbar\omega) \tag{2.4.55}$$

for coupling via the piezoelectric interaction. v_{sL} and v_{sT} are the longitudinal and transverse velocities. The δ function ensures energy conservation and the Kronecker delta implies conservation of momentum.

The summations in Equations 2.4.54 and 2.4.55 are replaced with integrals and become

$$\frac{1}{\tau_{DP}} = \frac{\pi \Xi_d^2 q}{(2\pi)^3 \rho v_{sL}} \int \delta_{\mathbf{k},\mathbf{k}'+\mathbf{q}}\, \delta(E_k - E_{k'} + \hbar\omega)\, F(E)\, d\mathbf{k} \tag{2.4.56}$$

and

$$\frac{1}{\tau_{PZ}} = \frac{\pi (e C_{-1})^2}{(2\pi)^3 \rho v_{sL} q} \int \delta_{\mathbf{k},\mathbf{k}'+\mathbf{q}}\, \delta(E_k - E_{k'} + \hbar\omega)\, F(E)\, d\mathbf{k} \tag{2.4.57}$$

where $F(E)$ is $f_k(1 - f_{k'})$.

The integral is performed in terms of θ, the angle between the phonon and electron wavevectors. The limits of the integration are calculated from energy and momentum conservation arguments [36].

Since energy and momentum are conserved, then

$$\mathbf{k} + \mathbf{q} = \mathbf{k}' \tag{2.4.58}$$

and

$$\frac{\hbar^2 k^2}{2m^*} + \hbar v_s = \frac{\hbar^2 k'^2}{2m^*} \tag{2.4.59}$$

Simplifying Equation 2.4.59, substituting into 2.4.58 and rearranging yields Equation 2.4.60.

$$k = \frac{q}{2\cos\theta}\left(\frac{2m^* v_s}{q\hbar} - 1\right) \tag{2.4.60}$$

Substituting for $E = \hbar^2 k^2 / 2m^*$ allows the minimum and maximum angles to determined. The integration is performed and the final result is given by Equation 2.4.61 [37].

$$\frac{1}{\tau_{DP}} = W_q^{DP} = \frac{\hbar\omega \Xi_d^2 q^2 m^*}{8\pi \rho v_{sL} E_F \hbar^2} \tag{2.4.61}$$

for DP coupling. The scattering time for PZ coupling can be found by replacing Ξ_d with $(eC_{-1})^2$, v_{sLA} with v_{sTA} and noting that the matrix element is $\propto 1/q^2$, Equation 2.4.62

$$\frac{1}{\tau_{PZ}} = W_q^{PZ} = \frac{v_{sLA}}{v_{sTA}} \frac{(e C_{-1})^2}{\Xi_d} \frac{1}{q^2} \frac{1}{\tau_{DP}} \tag{2.4.62}$$

The ballistic transit time, $\tau_0 = d/v_s$, where d is the epilayer thickness, is much less than the scattering times W_q for both modes and so the power absorbed by the electron gas can be written as in Equation 2.4.63.

$$\Delta T \sim P_{abs} = A\tau_0 \int_0^{\omega_{max}} W_q \hbar\omega\, \rho(\omega) N_q d\omega \tag{2.4.63}$$

where $\rho(\omega)$ is the phonon density of states, given by

$$\rho(\omega) = \frac{\omega^2}{2\pi^3 V} \tag{2.4.64}$$

2.4.8 PHONON DRAG

When a phonon is absorbed by an electron, the phonon transfers its momentum to that electron. Since electron–electron scattering occurs rapidly, this momentum is redistributed amongst all the electrons over a very short time–scale and the net result is a collective momentum and drift velocity of the electron system.

The phonon–drag induced current density is calculated using Equation 2.4.65.

$$\mathbf{j} = n_e e \mathbf{v} \tag{2.4.65}$$

where $\mathbf{v}$ is the drag induced drift velocity of the electrons given by Equation 2.4.66.

$$\mathbf{v} = \frac{\tau_p}{m^*}\mathbf{f} \tag{2.4.66}$$

Here $\mathbf{f}$ is the force from the flux of phonons, m^* is the effective mass and τ_p is the momentum relaxation time.

The force, $\mathbf{f}$, is given by Equation 2.4.67, taken from [38], and assumes that phonons with a wavevector $\sim 2k_F$ are absorbed. This assumption simplifies matters, since otherwise it is necessary to know the exact non-equilibrium phonon distribution.

$$\mathbf{f} = \frac{1}{n_e} \int_0^{2k_F} \frac{\mathbf{q}}{q} \hbar\omega \frac{W(\mathbf{q})}{v_s} N_q \frac{d^3\mathbf{q}}{(2\pi)^3} \tag{2.4.67}$$

where $W(\mathbf{q})$ is the probability that a phonon will be absorbed and all other symbols have their usual meanings.

The Bose–Einstein occupation number, N_q, must be modified to take into account geometric factors relevant to the experiment, and so N_q is given by

$$N_q = A \frac{1}{e^{\frac{\hbar\omega}{k_B T_m}} - 1} \tag{2.4.68}$$

where A is a factor which accounts for reflections at the GaN/sapphire interface and T_m is the temperature corresponding to the maximum in the Planckian distribution in the metal film.

Substitution of Equations 2.4.68 and the analytic expression for the absorption probability, Equation 2.4.62, into Equation 2.4.67 yields

$$f = \frac{A \cos\theta \, d\Omega \, (eh_1)^2 \, m^*}{n_e (2\pi)^3 \, 8\pi \, \rho \, E_F \, \hbar v_s} \int_0^{2k_F} \hbar\omega \, q^3 \frac{1}{e^{\frac{\hbar\omega}{k_B T_m}} - 1} dq \tag{2.4.69}$$

where $d\Omega$ is the solid angle into which phonons reach the electron gas all symbols have their usual meanings.

In the long wavelength limit $\omega = v_s q$ and substituting for $\hbar\omega / k_B T_\ell = X$ and $2k_F \, \hbar\omega / k_B T_m = X_0$ yields the following expression for the drag induced current density, Equation 2.4.70.

$$j = \frac{A \cos\theta \, d\Omega \, (eh_1)^2 \, (k_B T_m)^5 \, \tau_p}{4(2\pi)^4 \, \rho \, E_F (\hbar v_s)^5} \int_0^{X_0} \frac{X^4}{e^X - 1} dX \tag{2.4.70}$$

The integral in Equation 2.4.70 is evaluated numerically to give the phonon drag induced current.

REFERENCES

[1] H. Siegle, G. Kaczmarczyk, L. Filippidis, A. P. Litvinchuk, A. Hoffmann, and C. Thomsen. *Phys. Rev. B*, **55**, 7000, (1997).

[2] C. Bungaro, K. Rapcewicz, and J. Bernholc. *Phys. Rev. B*, **61**, 6720, (2000).

[3] H. M. Tutuncu and G. P. Srivastava. *Phys. Rev. B*, **62**, 5028, (2000).

[4] P. M. Morse and H. Feshbach. *Methods of Theoretical Physics, New York*, (1953).

[5] M. Fehrer, S. Einfeldt, U. Birkle, T. Gollnik, and D. Hommel. *J. Cryst. Growth*, **189/190**, 763, (1998).

[6] J.-L. Farvacque, Z. Bougrioua, I. Moerman, G. Van Tendeloo, and O. Lebedev. *Physica B*, **273-274**, 140, (1999).

[7] A. Yamamoto, K. Azuma, K. Ueno, Y. Tsuji, and A. Hashimoto. *phys. stat. sol (a)*, **176**, 689, (1999).

[8] M. G. Cheong, K. S. Kim, C. S. Oh, N. W. Namgung, G. M. Yang, C.-H. Hong, K. Y. Lim, E. K. Suh, K. S. Nahm, H. J. Lee, D. H. Lim, and A. Yoshikawa. *Appl. Phys. Lett*, **77**, 2557, (2000).

[9] N. M. Shmidt, V. V. Emstev, A. S. Kryzhanovsky, R. N. Kyutt, W. V. Lundin, D. S. Poloskin, V. V. Ratnikov, A. V. Sakharov, A. N. Titkov, A. S. Usikov, and P. Girard. *phys. stat. sol (b)*, **216**, 581, (1999).

[10] J. W. P. Hsu, D. V. Lang, S. Richter, R. N. Kleiman, A. M. Sergent, and R. J. Molnar. *Appl. Phys. Lett*, **77**, 2873, (2000).

[11] R. J. von Gutfeld. *in Physical acoustics : principles and methods*, (edited by W. P. Mason Vol. 5. New York, Academic Press 1968).

[12] W. A. Little. *Can. J. Phys.*, **37**, 334, (1959).

[13] F. Rosch and O. Weiss. *Z. Phys. B*, **27**, 33, (1977).

[14] J. P. Wolfe. *Imaging Phonons: Acoustic Wave Propagation in Solids, Cambridge University Press, Cambridge*, (1998).

[15] A. G. Every, G. L. Koos, and J. P. Wolfe. *Phys. Rev. B*, **29**, 2190, (1984).

[16] A. G. Every. *Phys. Rev. B*, **34**, 2852, (1986).

[17] A. G. Every and A. K. McCurdy. *Phys. Rev. B*, **36**, 1432, (1987).

[18] A. G. Every. (Private Communication).

[19] G. D. Mahan in. *Polarons in Ionic Crystals and Semiconductors (edited by J.T.Devreese), North-Holland, Amsterdam*, page 553, (1972).

[20] M. E. Daniels, B. K. Ridley, and M. Emeny. *Solid. State. Electron.*, **32**, 1207, (1989).

[21] M. Rothenfusser, L. Koster, and W. Dietsche. *Phys. Rev. B*, **34**, 5518, (1986).

[22] S. Das Sarma, A. Kobayashi, and W. A. Lai. *Phys. Rev. B*, **36**, 8151, (1987).

[23] Cz. Jasiukiewicz and V. Karpus. *Semi. Sci. Tech*, **11**, 1777, (1996).

[24] Cz. Jasiukiewicz. *Semi. Sci. Tech*, **13**, 537, (1998).

[25] L. Hsu and W. Walukiewicz. *Phys. Rev. B*, **56**, 1520, (1997).

[26] S. Das Sarma, J. K. Jain, and R. Jalabert. *Phys. Rev. B*, **41**, 3561, (1990).

[27] C. Y. Tsai, C. H. Chen, T. L. Sung, C. Y. Tsai, and J. M. Rorison. *J. Appl. Phys*, **85**, 1475, (1999).

[28] D. Das Sarma, A. Kobayashi, and W. Y. Lai. *Phys. Rev. B*, **36**, 8151, (1987).

[29] F. Binet, J. Y. Duboz, J. Off, and F. Scholz. *Phys. Rev. B*, **60**, 4715, (1999).

[30] B. K. Ridley. *J.Phys:Condens. Matter*, **10**, 6717, (1998).

[31] C. Bulutay, B. K. Ridley, and N. A. Zakhleniuk. *Phys. Rev. B*, **62**, 15754, (2000).

[32] J. K. Jain, R. Jalabert, and S. Das Sarma. *Phys. Rev. Lett*, **60**, 353, (1988).

[33] M. Giltrow, A. Kozorezov, M. Sahraoui-Tahar, J. K. Wigmore, J. H. Davies, C. R. Stanley, B. Vogel, and C. D. W. Wilkinson. *Phys. Rev. Lett*, **75**, 1827, (1995).

[34] S. Das Sarma, J. K. Jain, and R. Jalabert. *Phys. Rev. B*, **37**, 4560, (1988).

[35] B. K. Ridley. *J.Phys:Condens. Matter*, **8**, L511, (1996).

[36] B. K. Ridley. *Quantum Processes in Semiconductors (4th Edition), Clarendon Press, Oxford*, (1999).

[37] A. V. Akimov. *Private Communication.*

[38] L. V. Keldysh and N. N. Sibeldin. *in Non-Equilibrium Phonons in Non-Metallic Crystals, edited by W. Eisenmenger and A. A. Kaplyanskii, North Holland, Amsterdam*, (1986).

Chapter 3

SAMPLE PREPARATION AND EXPERIMENTAL TECHNIQUES

3.1 INTRODUCTION

This Chapter is concerned with the fabrication techniques required to produce the experimental samples and with the experimental procedures used. When compared to other materials such as silicon and gallium arsenide, the processing steps employed during GaN device fabrication are at a relatively early stage of development. A more detailed account of the processing steps developed during this work is presented in the Appendix. The discussion in this Chapter will be limited to the final results of the processing development. A detailed description of the experimental techniques used will also be presented.

3.2 SAMPLE PREPARATION

Gallium nitride and aluminium gallium nitride/gallium nitride samples have been studied in this work. Growth of the Group III nitrides can be achieved us-

ing many growth techniques, as outlined in Chapter 1, with MOCVD being the popular choice. Material from a variety of sources (and therefore a variety of growth conditions) has been utilised: GaN layers grown by MBE at the University of Nottingham; AlGaN/GaN heterostructures grown by MOCVD at Intec, Gent, Belgium and also at the University of Tokushima, Japan; AlGaN/GaN heterostructures, also grown by MOCVD at DERA, Malvern; and GaN template material, grown by HVPE by AXT, USA. All samples are grown on sapphire substrates. MBE layers have a coating of molybdenum on the back surface of the sapphire (to allow determination of temperature during growth). Although other substrates are used in GaN growth (GaAs, Si and SiC), earlier work [1] has shown that certain experiments on GaN on GaAs samples provide information about the substrates rather than the epilayers.

Gallium nitride sample preparation is often a lengthy procedure, requiring several processing steps. Perhaps the most striking difference between GaN and GaAs device fabrication is the resistance of GaN to almost all mineral acids and bases under standard conditions. Since a necessary requirement of this work was to produce structures with dimensions of the order of microns, a fundamental step in processing was mesa etching. Etching of GaN and its alloys is still an active area of research, and is perhaps the most troublesome aspect of sample manufacture. This Section will discuss the techniques employed during sample preparation.

3.2.1 CUTTING AND CLEANING

The first stage of processing was to cut the wafer into the appropriate sized pieces. Typical sample dimensions were ~4mm×3mm. Epilayer thickness varied between 0.8μm and ~5μm and the thickness of the sapphire substrate is ~380μm. With such small area devices and hard substrates, cleaving was not practical. Samples were cut using a diamond saw, held to the cutting stage using an adhesive tape. A cutting speed of ~0.5mm s^{-1} was used to avoid causing excessive damage to the sample edges.

After cutting, the samples were cleaned using the standard four solvent clean; ethyl lactate, acetone, methanol and isopropyl alcohol. Each step involves a 10 minute ultrasonic soak in the solvent. After the solvent clean, the sample can be baked at high temperature to remove any residual solvents.

3.2.2 PHOTOLITHOGRAPHY

The next stage was to define the overall pattern of the device. The device area must be protected from the etch, and the etching method determines the capping layer used. The sample was coated with resist, a photosensitive material, and was spun at ~4000 rpm for 30s. There are a variety of resists available offering different film thicknesses and profiles after developing. BPRS 150, a positive photoresist, was chosen for the majority of this work, giving a typical film thickness of ~1.5μm. After spinning, the sample was baked either on a hot plate at 110°C for 1 minute or in an oven at the same temperature for 30 minutes.

The pattern was transferred onto the wafer using a pre–written chrome on quartz mask. The resist to be removed was exposed to ultra–violet radiation using a Karl Suss MJB 3 mask aligner. (The UV source was a 275W mercury arc lamp). The exposure time was between 4s and 10s depending on resist thickness and type. After exposure, the resist was developed, leaving the required pattern on the wafer by washing in a solution of one part developer (a basic solution) to three parts water for between 20s and 60s depending on the resist thickness and exposure time used.

3.2.3 ETCHING

Two methods of etching have been used to make samples; photoenhanced wet chemical etching and reactive ion etching (RIE). In a research environment, where samples may be processed individually, wet chemical etching is an attractive method for mesa definition when compared to dry etching methods such as RIE, which is not only a lengthy process, but can also damage the surface of the

material being etched. However, to date, there are no wet etchants for either AlGaN or InGaN. Processing of these samples requires the use of dry methods.

AlGaN devices were etched by RIE (using silicon tetrachloride) by Dr.G.Hill at the EPSRC Central Facility, University of Sheffield. The capping layer for RIE is thick photoresist. A rule of thumb was that the photoresist should be twice as thick as the material to be etched. For the majority of samples, this means deposition of $\sim 4\mu$m resist. This can be achieved either by multiple coatings of BPRS 150 or by use of a thicker AZ resist. The etch rate achieved by this method was $\sim 1\mu$m h^{-1}.

GaN samples were etched by photoenhanced wet chemical etching (originally following the method described in [2]). With this method, a titanium layer $\sim$150nm was used as a capping layer and was deposited by thermal evaporation. Regions covered with titanium were protected from the etch. The experimental arrangement is shown in Figure 3.1. The sample was clamped to the Teflon base with a nickel washer providing contact to the capping layer. The base stands in a Teflon container with a platinum wire used as the cathode. The etchant was 0.5M potassium hydroxide (KOH). The solution was stirred and the photocurrent monitored during the etch. Illumination was provided by a 350W mercury arc lamp emitting at 365nm with an intensity at the sample in excess of 50mW mm^{-2}. Etch rates varied between 0μm h^{-1} and $\sim 6\mu$m h^{-1}. A more detailed discussion of this behaviour can be found in Appendix I.

The etch depth was determined by use of a Tencor alpha step. After etching, the titanium capping layer was removed with a 10:1 solution of water:hydrofluoric acid. The molybdenum coating was removed using a 1:1 solution of hydrochloric acid and hydrogen peroxide.

3.2.4 CONTACTS

With the mesa defined, another photolithography stage was required to expose areas of material for contacting. The contacts were formed by evaporation of

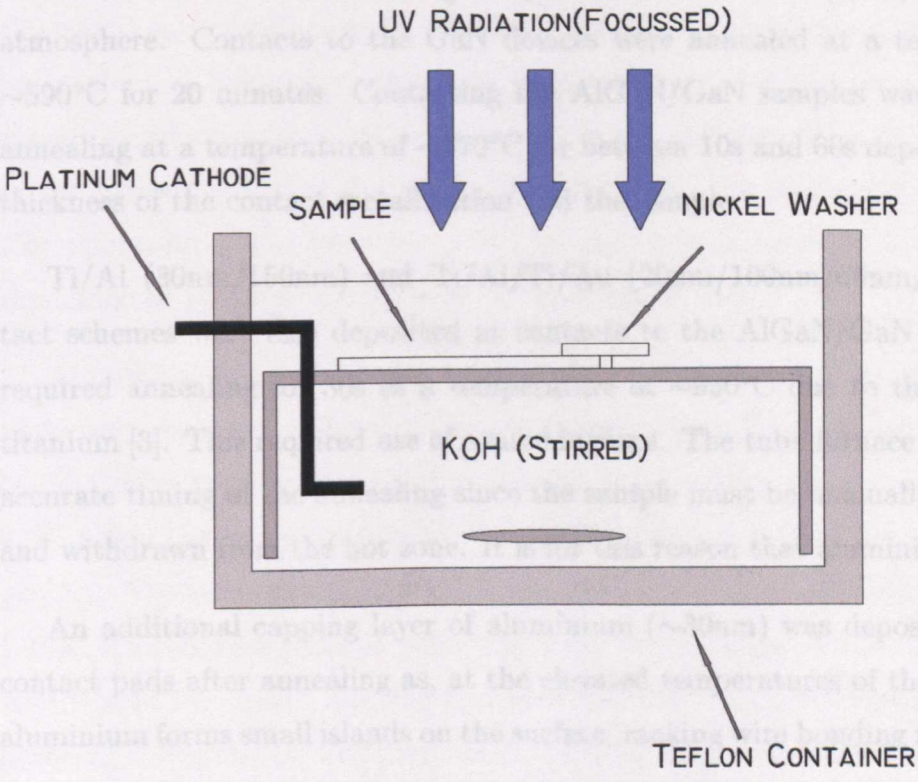

Figure 3.1: The arrangement for GaN etching. The sample is clamped to the Teflon base with a nickel washer holding the sample in place.

high purity metals using an Edwards E306A evaporator. Aluminium was used as the contact material for both the GaN and AlGaN devices, and was evaporated from a tungsten filament at a pressure of $\sim 10^{-6}$ mbar. The thickness and rate of deposition was monitored during the evaporation and was typically 150nm. After evaporation, "lift off" was performed by soaking the sample in acetone at 70°C until excess metal coated resist had been removed.

Contacts were annealed using a rapid thermal annealer (RTA) in a nitrogen atmosphere. Contacts to the GaN devices were annealed at a temperature of ~590°C for 20 minutes. Contacting the AlGaN/GaN samples was achieved by annealing at a temperature of ~570°C for between 10s and 60s depending on the thickness of the contact metallisation and the sample.

Ti/Al (30nm/150nm) and Ti/Al/Ti/Au (20nm/100nm/60nm/300nm) contact schemes were also deposited as contacts to the AlGaN/GaN samples, but required annealing for 30s at a temperature of ~950°C due to the presence of titanium [3]. This required use of a tube furnace. The tube furnace did not allow accurate timing of the annealing since the sample must be manually pushed into and withdrawn from the hot zone. It is for this reason that aluminium was used.

An additional capping layer of aluminium (~30nm) was deposited onto the contact pads after annealing as, at the elevated temperatures of the process, the aluminium forms small islands on the surface, making wire bonding more difficult.

3.2.5 POLISHING

In phonon emission and absorption experiments it was necessary to position structures on the reverse side of the sample. The sapphire substrates must be polished prior to structure fabrication as roughness between deposited materials and the sapphire can cause unwanted scattering as phonons traverse the interface.

Polishing was a three stage process for which a Multipol jig and polisher were used. The sample was held onto the jig with wax, which was removed from the sample after polishing by soaking in acetone at 70°C. The first two stages were

a mechanical polish, using 6μm and 1μm Hyprez diamond pastes on a solder lap. The final stage was a mechanical–chemical polish using Syton, an aqueous suspension of silicon dioxide, on a polyurethane lap producing a mirror finish.

3.2.6 PHONON DETECTOR FABRICATION

Two methods of phonon detection at low temperatures have been employed in this work; superconducting aluminium bolometers and cadmium sulphide (CdS) bolometers. A bolometer is a device in direct contact with the crystal that has a strong, rapid variation of some parameter with temperature, at the temperature of the experiment. For the two bolometers used, this parameter is resistance. The operation of the bolometers will be discussed in detail in Section 3.3.5 (a discussion of bolometric detection can be found in [4]).

Aluminium bolometers were fabricated using the photolithography techniques previously discussed. There are many geometries available for bolometric detection, offering varying degrees of sensitivity and angular resolution. Two designs were used, the larger serpentine design and the small loop, as shown in Figure 3.2. The superconducting transition temperature, T_C, of pure aluminium is 1.18K. This temperature is below the base temperature of the cryostats used. Addition of impurities into the film increases the transition temperature and is achieved using one of two methods. The first is to evaporate aluminium from a tungsten filament, as with contacts, but to deposit material at a pressure of $\sim 10^{-3}$ mbar. The second is to evaporate from an Al_2O_3 crucible at a pressure of $\sim 10^{-5}$ mbar. This results in a transition temperature of ~2.1K. In both cases, ~35nm aluminium is deposited during evaporation.

A two stage process was required for cadmium sulphide bolometer production. The sample was heated to ~90°C and ~1μm of CdS is evaporated at a pressure of $\sim 10^{-5}$ mbar. At this substrate temperature the film is cadmium rich and had an orange appearance. A shadow mask, rather than photolithography, was used to define the contacts; gold (~15nm) was evaporated onto the CdS. The CdS bolometer geometry is also shown in Figure 3.2.

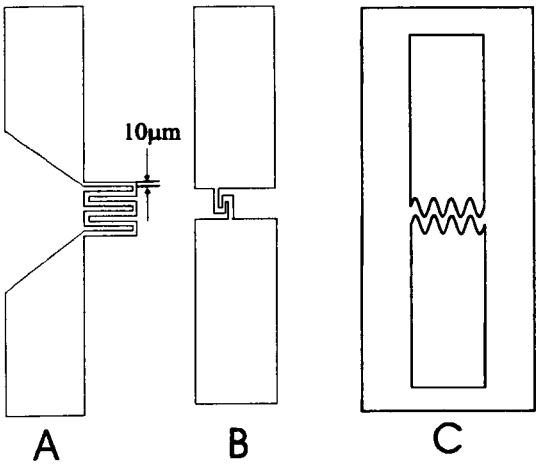

Figure 3.2: The geometry of the bolometers used in emission experiments. Designs A and B are superconducting aluminium bolometer patterns. The CdS bolometer design, C, is also shown.

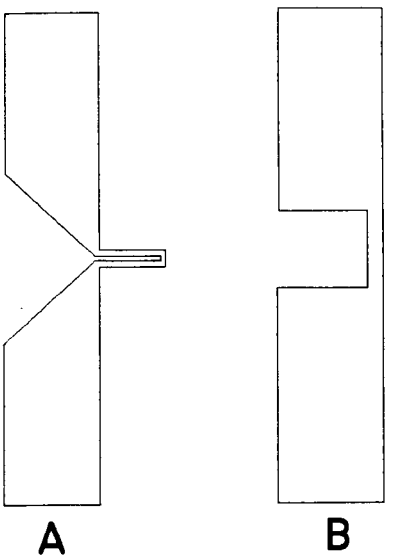

Figure 3.3: The geometry of the heaters used in absorption experiments. Geometry A is patterned using photolithographic techniques, with an overall area (the central region) of $30 \times 100\mu$m. The second design, B, is larger, with a central region area of 0.1×0.8mm, and is fabricated using a shadow mask.

3.2.7 PHONON SOURCE PRODUCTION

In phonon absorption experiments, phonons can be produced either by pulsed electrical or optical heating of a thin metal film. Details regarding the generation of phonons can be found in Section 2.3.4. Heaters have been produced using both standard lithographic techniques and by use of a shadow mask, depending on the sample geometry. Heater geometries are shown in Figure 3.3. Between 50–70nm of constantan (an alloy of copper and nickel) was evaporated onto the substrate at a pressure of $\sim 10^{-5}$ mbar. For heaters used in this work, this gave a heater resistance of $\sim 50\Omega$. Heater resistances of 50Ω are desirable as they match the cable impedances and so aid in the reduction of electrical pick–up. For optical excitation, a constantan film with a thickness of ~300nm was evaporated onto the substrate. Care was taken to ensure the metal film is of high quality, free from scratches.

3.3 EXPERIMENTAL PROCEDURES

3.3.1 THE CRYOSTATS

Two cryostats were used to perform the experiments. The Oxford Instruments Optistat Bath cryostat is the smaller of the two, having the advantage of fast fill and cooling times. The Oxford Instruments Spectromag 3 cryostat is much larger, and houses a superconducting NbTi split coil magnet which provides a magnetic field up to 7T perpendicular to the sample. Both cryostats offer optical access to the sample space via quartz windows. The helium reservoir and sample space are surrounded with a radiation shield which is cooled with liquid nitrogen. A vacuum jacket minimises gaseous conduction, and a vacuum of $\sim 10^{-6}$ mbar is achieved with a diffusion pump. Adjustment of a needle valve allows liquid helium from the reservoir to be admitted into the sample space. To allow cooling below 4.2K, the vapour pressure in the sample space is reduced using a rotary pump. The Optistat cryostat has a base temperature of ~1.3K, while the Spectromag 3 has

a working temperature of ~1.5K. In experiments where it is necessary to hold the temperature above the base temperature, a manostat on the pumping line is used. A reference pressure of helium (corresponding to the required temperature) is trapped. This pre-set pressure is maintained by pumping through the manostat, and so the temperature is regulated. It is also possible to control the temperature without use of the manostat by careful adjustment of the needle valve and a valve on the pumping line. An introduction to low temperature experimentation is given in [5].

Both cryostats now have laser systems allowing optical excitation of samples. A recent addition to the Optistat is a UV laser, emitting at 355nm (produced by frequency tripling a Nd:YAG (yttrium aluminium garnet)), allowing a wide range of experiments on nitride samples to be performed in the future. A Nd:YLF (yttrium lithium fluoride) laser, emitting at 524nm, is used for imaging experiments (where optical excitation of a metal heater film is required) with the Spectromag 3.

3.3.2 SAMPLE MOUNTING

Samples were mounted onto the end of the sample rod or "dipstick", which was lowered into the cryostat from above. The height of the dipstick can be adjusted, allowing the sample to be correctly oriented within the sample space with respect to magnetic field and laser spot position. The dipstick is a thin walled stainless steel tube with a copper block mounted on the lower end. The stainless steel tube has a low thermal conductivity to reduce heat losses. The copper block has a high thermal conductivity and ensured that the sample and thermometer were at the same temperature. Two thermometry schemes were used. Measurements made using the Optistat utilised a calibrated Cernox resistor, whilst experiments performed in the Spectromag 3 used a combination of a rhodium–iron resistor and an Allen–Bradley resistor (a calibrated carbon resistor). The Cernox thermometer is sensitive over the temperature range 1.3–400K, adequately satisfying the requirements of the experiments. The rhodium–iron is accurate down to a tem-

perature of ~30K, while the Allen–Bradley can be used from ~60K down to base temperature. In this work, where measurements required accurate knowledge of sample behaviour as the temperature was varied, care must be taken to ensure that the measured temperature was the same as the sample temperature. This required careful placement of the thermometers, away from helium inlets into the sample space. The thermometers were embedded within the copper block with an interference fit, and held in place with use of GE varnish, a relatively high thermal conductive adhesive varnish. Low currents were passed through the resistors and the change in temperature was measured as a change in voltage. Both the Cernox and Allen–Bradley resistance increase rapidly at low temperature (whereas the resistance of the Rh–Fe decreases from ~100Ω at room temperature to ~30Ω at 30K). To avoid self–heating of the resistors, low (100nA) currents ware used.

Rather than using a prefabricated 8 or 16 pin chip holder, the samples were mounted onto a copper plate, held either with GE varnish or silver dag (a conducting adhesive). A header strip was soldered to the copper plate and eight pins on the header allowed four contacts to be wired. The plate was screwed to the dipstick copper base plate, ensuring good thermal contact. The copper sample and base plates permit reverse access to the sample, allowing for laser excitation and also wiring to structures on the sapphire substrate.

Electrical contact to the sample was achieved by using one of two wire bonding schemes. In devices where the contact pads were large, rolled indium wires were pressed onto the contact metal and secured with silver dag. The other ends of the indium wires were pressed onto the appropriate header pins and again secured with dag. When the contact pads were small, or closely spaced, 25μm gold ribbon was bonded to the pads using silver epoxy as the adhesive. The silver epoxy was cured at ~ 120°C for ~2 hours. The process was repeated when attaching the wires to the header pins.

With the copper plate attached to the base plate, the header was plugged into the socket. Four co–axial cable run from the socket, are wrapped around the length of stainless steel tube, as are the thermometry and heater wires, and are anchored at points along the length of the tube, before being passed through

the centre of the tube to the top plate of the dipstick. Four co–ax connectors on the brass top plate allow wiring to the sample from outside the cryostat. Figure 3.4 shows the sample mounting arrangement, while Figure 3.5 shows the sample geometries used in the experiments.

3.3.3 ENERGY RELAXATION MEASUREMENTS

There are essentially two aspects to the energy relaxation experiments, from which the optic phonon energy, optic phonon scattering time and acoustic phonon power dependencies are obtained. The first step was to obtain an accurate "temperature calibration", a measurement of the resistance of the device as a function of temperature. The second stage was to apply short voltage pulses across the device and measure the device resistance. From comparison of these two measurements, the input voltage, and therefore power, as a function of temperature could be obtained.

TEMPERATURE CALIBRATION

The temperature calibration was performed such that the input power did not cause heating of the electrons above the lattice temperature, i.e. $T_e = T_l = T_{equilibrium}$. In two terminal measurements, there are two techniques that can be employed to satisfy this condition. These are referred to as "the lock–in technique" and "the pulse calibration".

The lock–in technique uses the reference output from a Stanford Research Systems SR 830 lock–in amplifier. There are several options for making this measurement, with the choice depending on the exact sample wiring arrangement. The output from the lock–in, typically 1V rms, at a frequency of ~1kHz, was put across a 1MΩ resistor in series with sample. This provided a constant current of 1μA to the device (provided that the device resitance, $R_{dev} \ll 1\text{M}\Omega$). The lock–in was then used to monitor the change in voltage across the sample as the temperature was varied. In samples where the pulse measurement was to

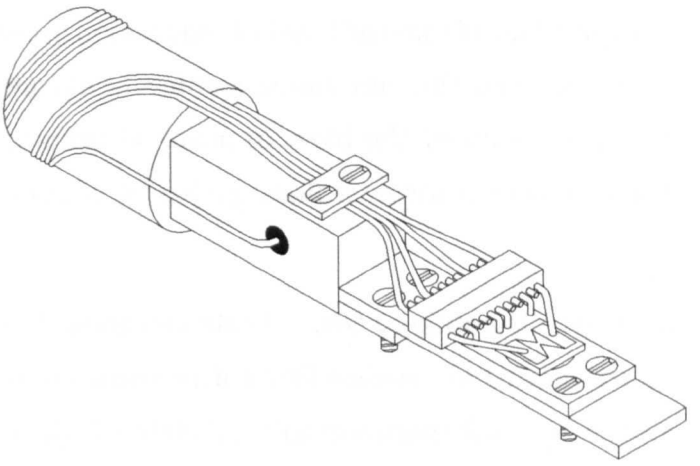

Figure 3.4: The sample mounting arrangement.

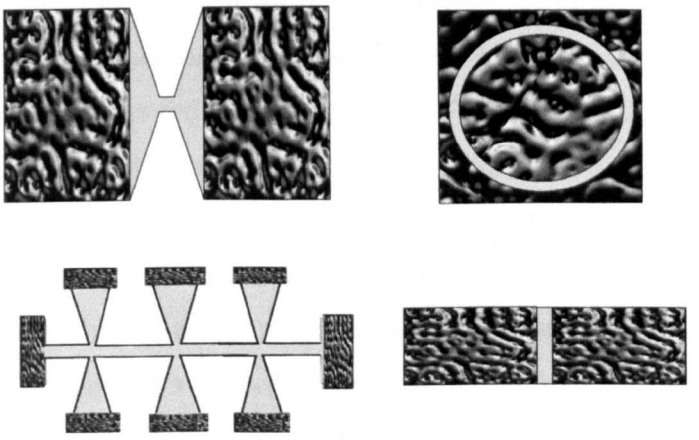

Figure 3.5: The geometry of the devices used in the experiments. The patterned areas are the metal contacts, while the grey shaded regions are the uncoated GaN or AlGaN areas. The two geometries on the right hand side can be fabricated without mesa etching.

be performed, a 10Ω resistor was mounted onto the header block on the copper sample plate in series with the device. In this case, 0.1V rms from the lock–in was applied directly across the device. Current through the device was measured by noting the change in voltage across the 10Ω resistor, again measured using the lock–in. Care must be taken to avoid self–heating effects at low temperature, which can be observed by noting small temperature changes as the input voltage is reduced.

The pulse calibration can also be used to obtain the temperature dependence of samples which are wired with a 10Ω resistor. In this method, small, short voltage pulses (typically 50–100mV, 20ns duration) from an Avtech pulse generator were applied to the sample. The voltage across the 10Ω resistor was monitored using a high–speed digitising Philips PM 3323 oscilloscope. The voltage can be taken directly from the scope, although this method can present problems. The change in measured voltage across the temperature range was small, and the signals themselves were small and tended to be noisy. An alternative was to use the SR 250 boxcar integrator. The signal could be amplified using up to four ×5 modules on the SR 240 fast pre–amp. A sampling window, or "gate", was appropriately positioned and the signal could be averaged up to 10 000 times. The output of the boxcar was fed into a Solartron 7150 digital multimeter (DMM). The pulse height was measured using the scope and was used to determine the scaling factor necessary to convert the boxcar output into the required voltage reading. Temperature calibrations were performed when cooling and also warming the sample up to room temperature after the measurements at base temperature have been made. This allowed any hysteresis effects, indicative of damage to the sample during low temperature measurements, to be observed.

The temperature was measured using a Stanford Research Systems SR 510 lock–in, with a reference voltage of 1V applied across either a 1MΩ (for the Rh–Fe and Allen–Bradley resistors) or a 10MΩ (for the Cernox sensor) resistor in series with the thermometer used. A four terminal measurement was made, and the voltage of the thermometers was measured using the SR 510.

The temperature was controlled and the data were recorded with a PC using

the PID controller written by Dr.P.Hawker. The program can read the output from the lock–in amplifiers and DMM or can read cursors set on the scope. The calibrations of resistance against temperature, whether supplied by the manufacturer or measured, are incorporated into the software allowing the variation of voltage to be directly measured as a function of temperature.

With four terminal measurements, a Keithley 224 programmable current source (DCS) was used to provide a current of 10μA or 10 mA through the source–drain contacts of a Hall bar. The voltage between two potential probe contacts along one side of the device was measured using a DMM.

PULSE MEASUREMENTS

In two terminal devices, with the sample held at the base temperature, electrons were heated above the lattice temperature by applying short voltage pulses from the Avtech pulse generator. Subsequent energy relaxation was by emission of phonons. By measuring the voltage across the series resistor, the power and resistance during the pulse was obtained.

The pulse generator was capable of producing 0–80V pulses. By use of a FET based amplifier, the maximum amplitude of the pulse was increased to 160V. The amplitude of the pulse applied to the device was controlled with a programmable attenuator capable of 0 dB to 63 dB attenuation in single dB steps. Measurement of the voltage across the 10Ω resistor was achieved using the methods previously described for the pulse calibration. For low voltages, the signal could be amplified using the $\times 5$ modules before being displayed on the scope.

With four terminal devices, the current–voltage relation was measured at base temperature. The voltage between the two side contacts was measured as the current through the device, supplied from the DCS, was increased from 0–1.5mA in 10μA steps.

Comparison of the temperature calibration with the pulse measurements or I–V allowed the dependence of power dissipated as a function of electron temper-

ature to be obtained. The experimental arrangement is shown in Figure 3.6.

3.3.4 AN EXAMPLE OF THE ANALYSIS TECHNIQUE

This Section introduces the analysis techniques used to obtain the plots of power dissipated as a function of electron temperature. As with the description of the experiment, the transformations of the temperature calibration data and the pulse data are discussed separately. A discussion of the nature of the GaN samples is also included.

THE NATURE OF GaN – "THE TWO BAND MODEL"

The "two band model" has been proposed to explain the temperature dependence of Hall measurements performed on bulk epilayers (see [6] and references therein). In this model, the system is considered to consist of a relatively high mobility conduction band and a lower mobility impurity band. At low temperatures, the electron population in the low mobility impurity band is relatively high, while that of the conduction band is small. When the samples are pulsed, it is the conduction band electrons which are initially heated. However, due to rapid electron–electron interactions, the electrons in the effectively localised impurity band can be considered to be at the same temperature as those in the conduction band. This thermalisation of electrons occurs over a much shorter time than acoustic phonon emission, and so at low temperatures all electrons participate in energy relaxation. It is therefore appropriate to use the room temperature carrier concentration in the calculation of the theory curves and for the analysis of experimental data across the temperature range of interest.

TEMPERATURE CALIBRATION

As mentioned in Section 3.3.3, the first step in the energy relaxation measurements was to obtain the "temperature calibration", a measurement of device resistance as a function of temperature. A typical temperature calibration curve

is shown in Figure 3.7. As was discussed in Section 3.3.3, there are many techniques available for recording the temperature dependence.

The original method used to obtain the curve was the pulsed temperature calibration, with pulse heights measured directly from the scope. Voltage pulses were kept short, generally 20ns, and were typically ~100mV amplitude to avoid self–heating effects. The device resistance is calculated using transmission line theory

$$R_D = \frac{100V_f}{6V_m} - 58 \tag{3.3.1}$$

where V_f is the voltage applied to the sample and V_m is the voltage measured across the 10 Ω series resistor. The numerical factors account for the characteristic impedance of the cables and for the series resistor.

The expression 3.3.1 comes from consideration of the reflected voltage that occurs when the sample and cables are not impedance matched. The voltage that the sample "sees" is given by the sum of forward and reflected voltages, and

$$I = \frac{V_f + V_r}{R_D} \tag{3.3.2}$$

and

$$R_D = \frac{V_f + V_r}{V_f - V_r} Z \tag{3.3.3}$$

where V_r is the reflected voltage and Z is the impedance of the line. Re–arranging the above expressions allows the device resistance to be obtained in terms of forward voltage,

$$R_D = \frac{2V_f}{I} - Z \tag{3.3.4}$$

The voltage across the 10Ω resistor was monitored, and substitution of I leads to Equation 3.3.1. This approach has been used elsewhere (see [7], for example).

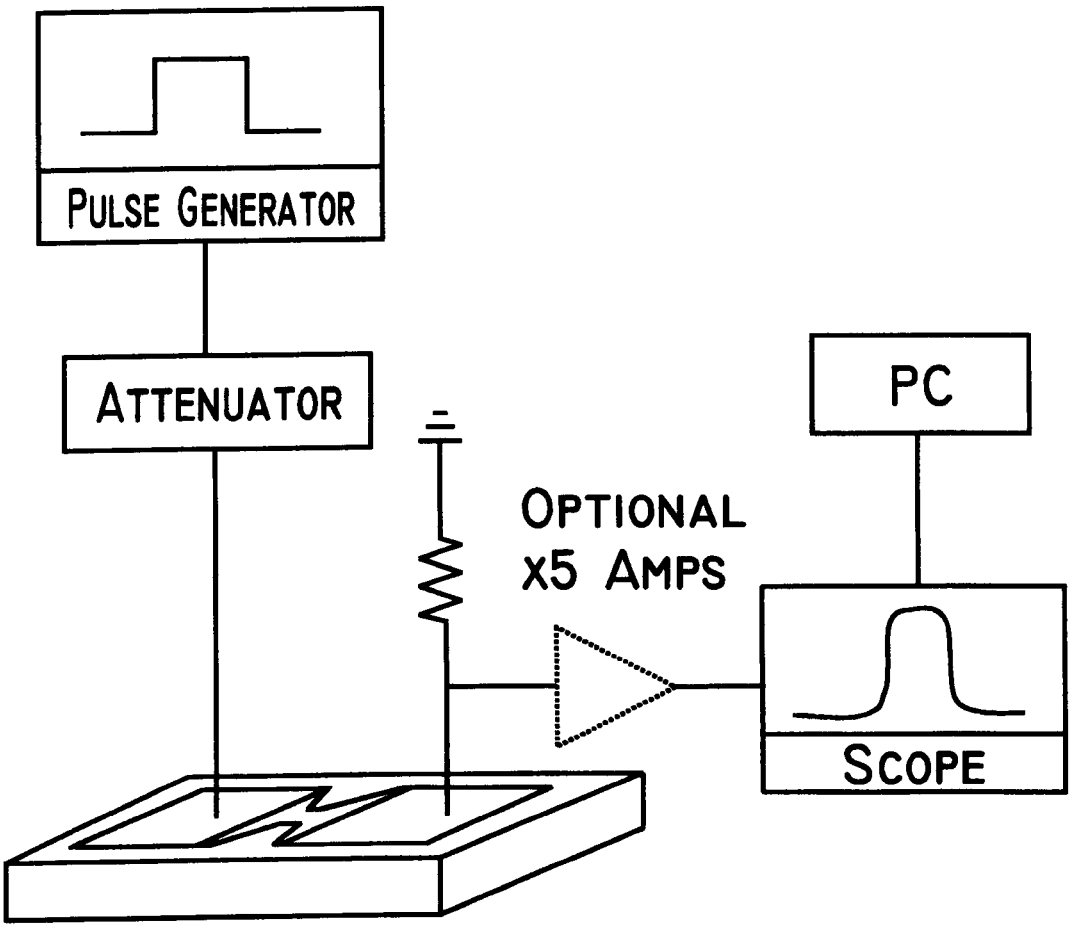

Figure 3.6: The experimental arrangement for the energy relaxation experiments.

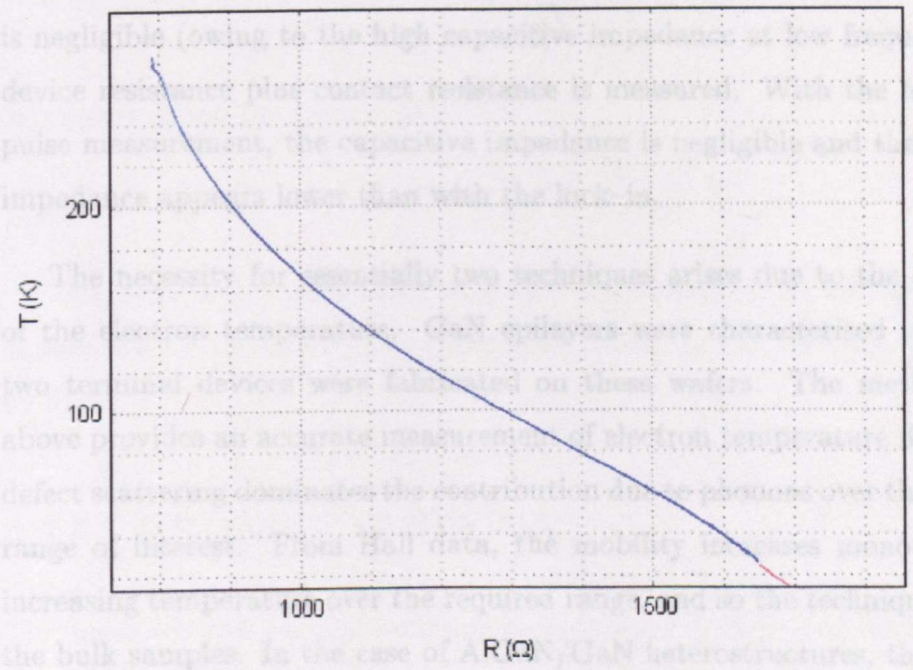

Figure 3.7: The temperature calibration curve for MG 588. The device resistance increases with decreasing temperature.

So for a device resistance which varies between 500 Ω and 1000 Ω from room temperature to 1.5K, the measured pulse height will change by ~1.5mV. Thus, the major problem of the pulse calibration when reading directly from the scope was that of noisy signals. Noise of the order of 50μV on a 1.5mV signal represents a resistance uncertainty of ~50 Ω. The temperature calibration must be of high quality, and so the signal was averaged using the boxcar to reduce the random noise. Another method employed was to use the output from a lock–in, generally both methods were employed enabling any effects due to contact capacitance to be identified. When the lock–in is used, the shunting effect of the contact capacitance is negligible (owing to the high capacitive impedance at low frequency) and the device resistance plus contact resistance is measured. With the high frequency pulse measurement, the capacitive impedance is negligible and the total contact impedance appears lower than with the lock–in.

The necessity for essentially two techniques arises due to the determination of the electron temperature. GaN epilayers were characterised elsewhere, and two terminal devices were fabricated on these wafers. The method described above provides an accurate measurement of electron temperature if impurity and defect scattering dominates the contribution due to phonons over the temperature range of interest. From Hall data, the mobility increases monotonically with increasing temperature over the required range, and so the technique was valid in the bulk samples. In the case of AlGaN/GaN heterostructures, this approach is no longer applicable and more specialised methods are employed to separate the contributions. At a high enough current, heating of the electrons occurs and this causes a difference in device resistance at the base temperature when compared with the low current curve. This difference is corrected for, and the high current calibration curve is used to obtain the contribution to resistance from phonons as a function of temperature. Impurity and defect scattering depend only on the electron temperature. By subtracting the contribution from phonons from the low current curve, the contribution from impurities and stimulated processes remains, and this is the calibration curve. A more detailed discussion of the method is given in Section 5.3.2.

PULSE MEASUREMENTS

Figure 3.8 shows a typical set of pulse data. Non–ohmic behaviour can clearly be seen. As with the temperature calibration, there are numerous methods available for collection of the signal. Pulse heights have been measured both directly from the scope or by using either the fast pre–amp or boxcar averager if the signals were small or noisy.

The power dissipated by the device (using Equation 3.3.4) is given by

$$P_D = 2IV_f - I^2Z \tag{3.3.5}$$

and substituting for I leads to

$$P_D = \frac{12V_mV_f}{50} - \frac{36 \times 58}{2500}V_m^2 \tag{3.3.6}$$

The data was transformed into the more useful form of dissipated power against device resistance, and comparison with the temperature calibration can be made.

3.3.5 PHONON EMISSION

The basis for the phonon emission experiments is described as follows. Short electrical pulses were applied to the sample, heating the carriers above the ambient lattice temperature. These excited electrons relax their energy by emission of phonons. The emitted phonons traverse the sapphire substrate and were detected by an appropriately positioned bolometer on the back of the wafer. The arrival of the ballistic phonons was directly observed by biasing the bolometer allowing the heat pulse to be detected as a change in voltage across the bolometer. The experimental arrangement is shown in Figure 3.10.

The operation of aluminium bolometers as phonon detectors relies on successfully exploiting the superconducting properties of the metal. A typical bolometer transition is shown in Figure 3.11, and was recorded using the lock–in technique described in Section 3.3.3.

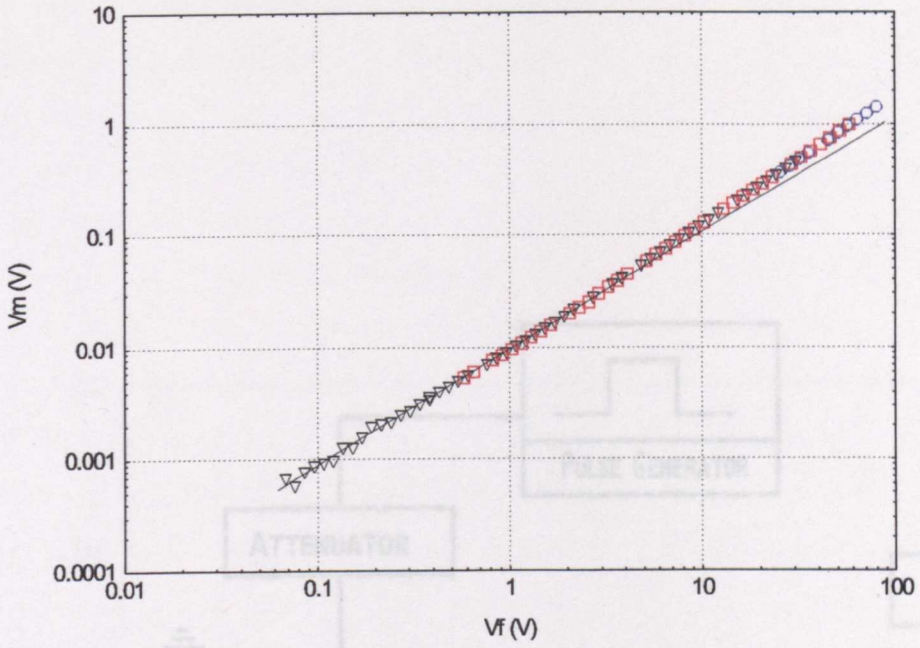

Figure 3.8: A plot of the measured voltage as a function of applied voltage for the same sample as shown in Figure 3.7. The line is to emphasise the deviation from ohmic behaviour.

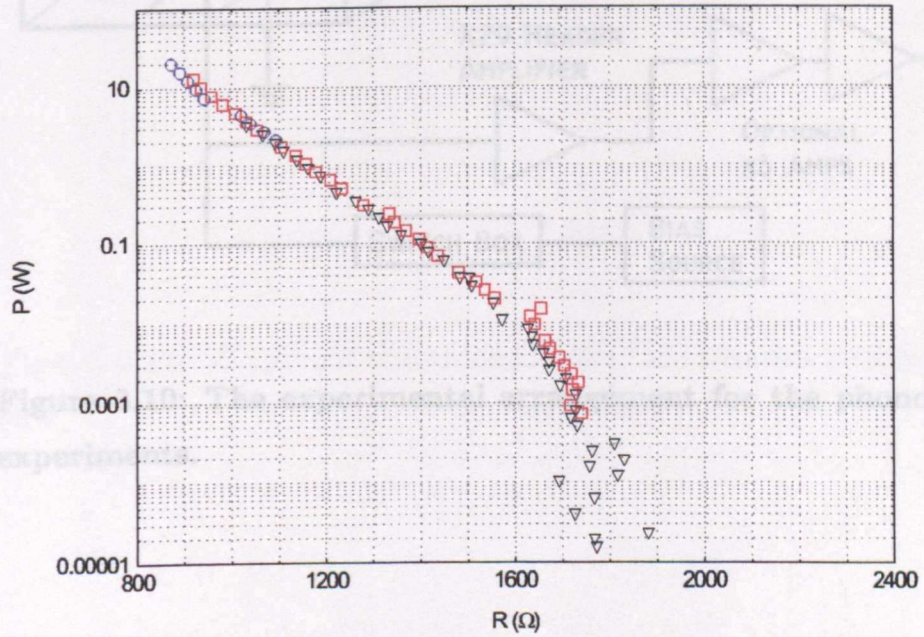

Figure 3.9: Transformation of the pulse data allows power as a function of resistance to be displayed.

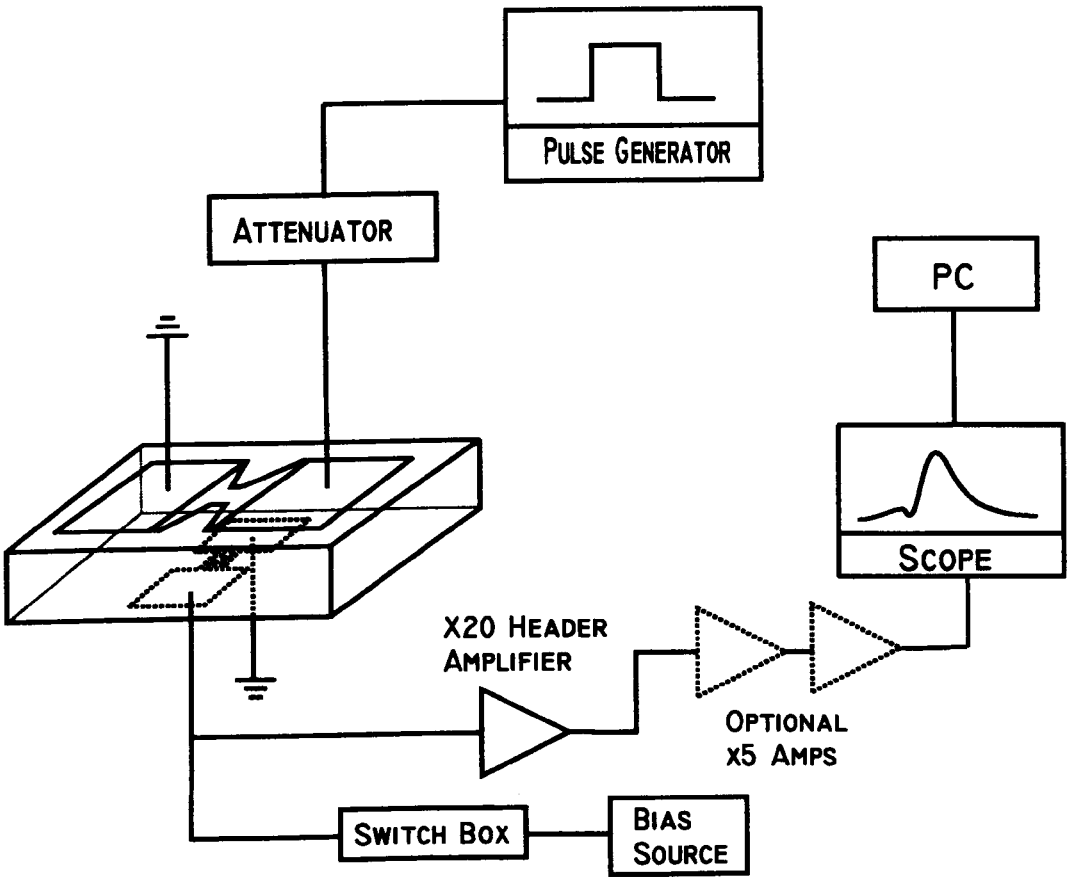

Figure 3.10: The experimental arrangement for the phonon emission experiments.

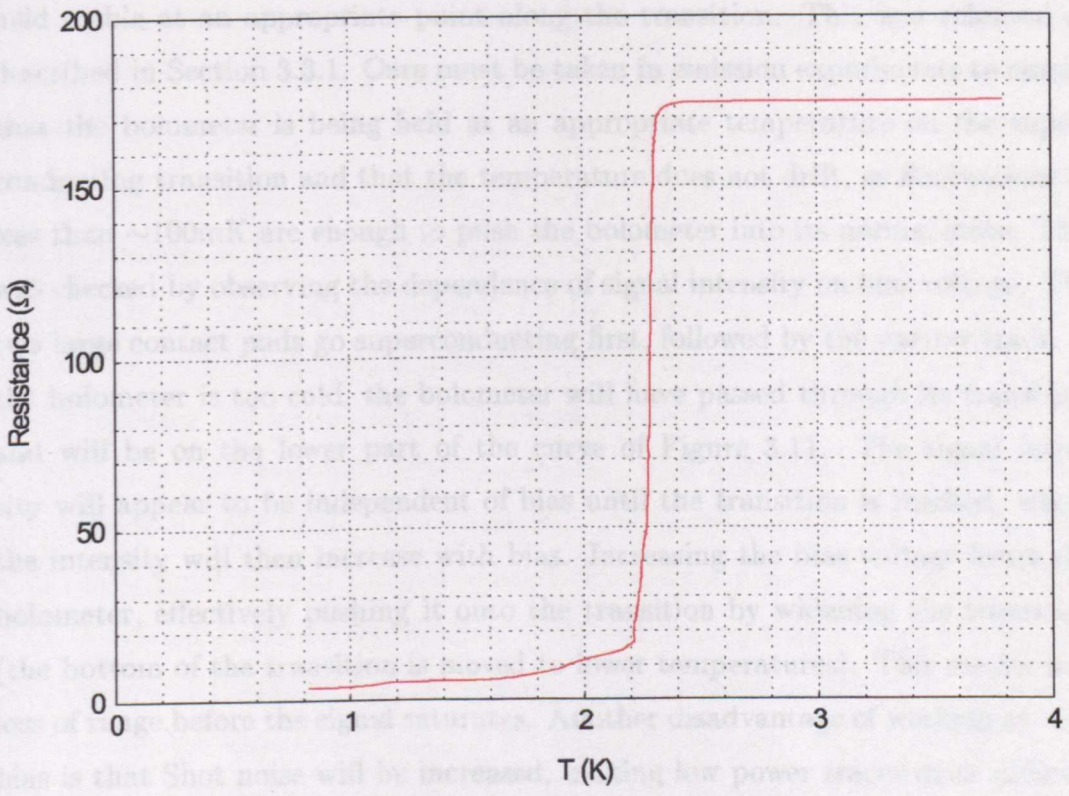

Figure 3.11: A typical superconducting aluminium bolometer transition.

With incorporation of impurities, the transition temperature is raised to ~2K. The transition is sharp and so any small change in temperatures causes a large change in resistance. Phonons incident on the film are absorbed and thermalised, increasing the temperature and pushing the bolometer along its transition. The bolometer was biassed with a constant current provided by a constant voltage applied to a 100kΩ resistor in series with the bolometer. This allows the phonons to be detected by observing the change in voltage. The temperature must be held stable at an appropriate point along the transition. This was achieved as described in Section 3.3.1. Care must be taken in emission experiments to ensure that the bolometer is being held at an appropriate temperature on the superconducting transition and that the temperature does not drift, as fluctuations of less than ~100mK are enough to push the bolometer into its normal state. This was checked by observing the dependence of signal intensity on bias voltage. The two large contact pads go superconducting first, followed by the narrow track. If the bolometer is too cold, the bolometer will have passed through its transition and will be on the lower part of the curve of Figure 3.11. The signal intensity will appear to be independent of bias until the transition is reached, where the intensity will then increase with bias. Increasing the bias voltage heats the bolometer, effectively pushing it onto the transition by widening the transition (the bottom of the transition is moved to lower temperatures). This results in a loss of range before the signal saturates. Another disadvantage of working at high bias is that Shot noise will be increased, making low power traces more difficult to obtain. Increasing the bias voltage also pushes the narrow track (which is detecting the phonons) towards the critical current I_C. If the bias is so high that I_C is reached, the detecting track is driven into the normal state and incident phonons will have no effect. However, if a bolometer with tapering contact pads is used, the increased bias may be sufficient to widen the transition such that previously superconducting regions of the pads are now capable of phonon detection. In this situation, where contacts are responsible for the observed signals, analysis becomes almost impossible. If the temperature is too high, the bolometer is near the top of its transition, and in this case increasing the bias quickly saturates the bolometer. In practice, a compromise between signal intensity and

dynamic range is made. The disadvantage of using aluminium detectors is that although for low power pulses they provide a very sensitive detector, at the high powers required in the experiments the bolometers saturated at a few tenths of a watt dissipation in the devices. Aluminium detectors are not suitable for magnetic field work, although the degradation of the transition with increasing field (up to the point where the bolometer is driven normal) has been employed to de–sensitise the detector on occasions where the transition occurred over a very narrow range of temperatures. In these situations, holding the bolometer at the required temperature was not possible, and application of a small magnetic field widened the transition.

When using higher power pulses, it was necessary to use semiconducting cadmium sulphide bolometers as detectors. These bolometers have a much larger dynamic range and did not saturate for the highest powers used in the experiments. At room temperature, the bolometer resistance was typically 2–7kΩ. Upon reducing the temperature, the resistance increased to several hundred kΩ or even MΩ at liquid helium temperatures. The bolometer was not sensitive to phonons in this state. The bolometer was activated with above band gap (>2.42eV) illumination, using a small bulb mounted onto the sample header. This promoted electrons into shallow traps which were then thermally activated into the conduction band and the resistance was reduced to something approaching the room temperature value. This induced conductivity was persistent for several hours if the temperature remained low. Detection occurred through a process of thermal activation of carriers. As the phonons were thermalised in the film, the temperature was increased slightly and this promoted carriers into the conduction band, which was observed as a change in the resistance of the bolometer. As before, by biassing the bolometer, the arrival of phonons could be seen directly as a change in voltage. Cadmium sulphide bolometers can also be used in magnetic field studies.

Samples were pulsed as described in Section 3.3.3. Signals from the aluminium bolometer were amplified using a low impedance $\times$20 inverting amplifier. Due to the higher CdS bolometer resistance, a high impedance amplifier (non–inverting,

×10 gain) was used. If required, the signals could be further amplified by the SRS boxcar ×5 modules before being fed out of the screened room via an opto–coupler (an inverting amplifier with a gain ×6) to the scope and digitiser. The trigger signal for the scope and digitiser was passed out of the screened room via another opto–coupler. The excitation pulse was kept short, typically 20ns with a repetition rate of 20kHz, to avoid equilibrium heating of the system and allow carriers to cool between pulses. The programmable attenuator stepped through the required range, and the phonon signals for each excitation power were recorded using Scan (a description of the software can be found in [8] and [9]) and averaged typically ~65 000 times.

3.3.6 PHONON ABSORPTION

In phonon absorption experiments, it is the device which is used as the phonon detector, with phonons being generated either by electrical pulsing of a heater or optical excitation of a metal film on the back of the wafer. This burst of non–equilibrium phonons traverses the substrate, with a small fraction of the generated phonons being absorbed and eventually thermalised in the epilayer. Absorption of phonons is detected as a change in resistance, in the same manner as emission experiments.

The constantan heater was pulsed with ~20ns pulses provided by a Philips 5786B pulse generator capable of producing 5V pulses. The sample was biassed in the same manner as the bolometer, with the series resistor varied as necessary to avoid heating the sample. The device resistances were typically a few kΩ at liquid helium temperatures, much greater than the aluminium bolometers, and so a high impedance amplifier was used. Further amplification was used as required and the signal passed to the PC via the opto–couplers. The attenuation of the heater excitation pulse was altered and the corresponding signals recorded.

The temperature dependence of the sample was measured in the same manner as the heat pulse experiment was performed i.e. using the same bias current and measuring the change in voltage across the device using a lock–in. This allowed

comparison of the phonon signal with the temperature calibration so that the phonon induced change in conductivity could be observed in terms of electron temperatures. The experimental arrangement is shown in Figure 3.12.

3.3.7 OPTICAL TECHNIQUES

As previously mentioned, optical excitation can be used as an alternative to electrical pulsing of samples or heaters. The major advantage of this method is that detailed information regarding the angular dependences can be readily obtained. The signals obtained from optical experiments are also free from some of the inherent problems in electrical measurements (which are discussed in Section 3.3.8).

Phonon imaging experiments can provide useful and detailed information regarding focussing of phonons in a crystal. In this work, sapphire has been studied using this method, along with the GaN epilayers. Although there are many possible experimental arrangements (determined by what is used as the detector and where the phonons are produced), the basic principles are the same. A metal film is evaporated onto one surface, and this film is optically excited, producing a Planckian distribution of phonons. The phonons are detected on the opposite face of the crystal.

The film was excited using one of the two optical set–ups, with a focussed beam size of $\sim 20\mu$m. The beam could be attenuated by use of a series of glass slides onto which aluminium of various thicknesses had been evaporated. The laser was raster scanned over the sample using two galvanometer controlled mirrors. The detector, whether it be the GaN itself or a superconducting aluminium bolometer, was biassed in the usual way and signals were amplified and recording in a manner analogous to emission and absorption experiments. The experimental arrangement is shown in Figure 3.13.

Imaging required that the polished surface of the sapphire was parallel to the grown layer. Relatively small deviations in substrate thickness manifest them-

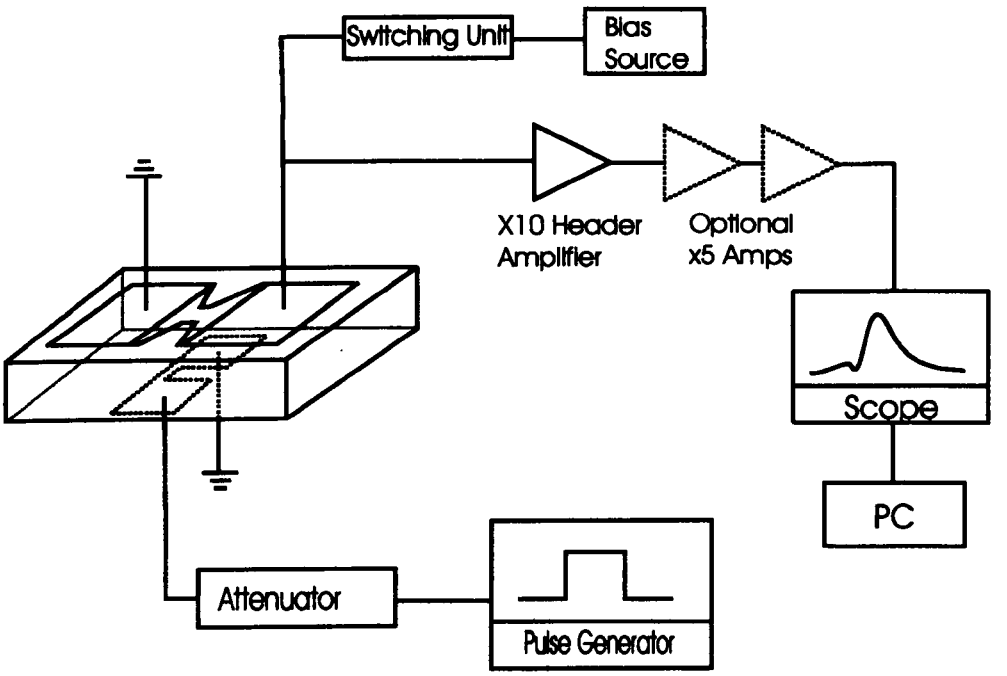

Figure 3.12: The experimental arrangement for the phonon absorption experiments.

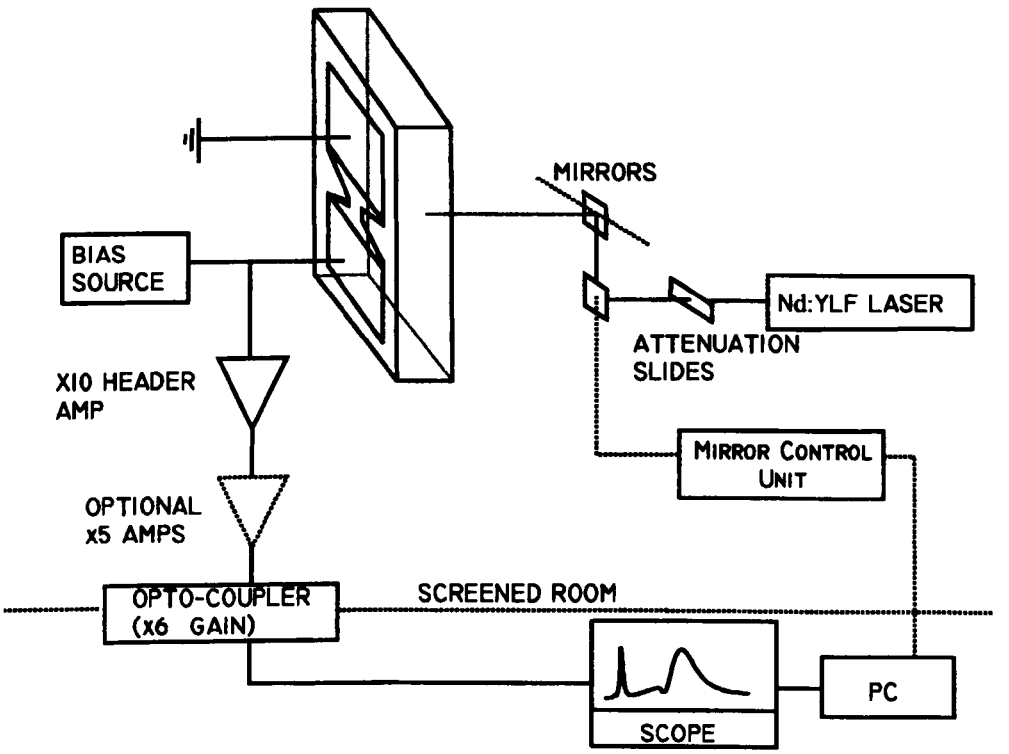

Figure 3.13: The experimental arrangement for the phonon imaging experiments.

selves as a gradual increase (or decrease) in the overall intensity across the scan. A deviation of only 20μm across the scan area causes a 3ns change in the arrival time, which can complicate the interpretation of imaging results where the signal is gated.

3.3.8 NOISE, PICK–UP AND OTHER IRRITATIONS

In all experiments, care must be taken to identify possible sources of error and inaccuracy, and where possible, eliminate them. Electrical measurements suffer from noise created by the circuit itself. Add to this the difficulties of working at low temperatures and also that the signals studied are not only small but the response of the system is fast. These factors must all be considered if reliable information is to be obtained. This Section discusses some of the more troublesome aspects of the experiments.

REDUCTION OF NOISE

Random motion of electrons due to their thermal energy causes an inherent noise level in any system. In phonon emission and absorption experiments, signals are amplified and passed out of the screened room via the opto–couplers. If no additional stages of amplification are used, the total amplification of the signal is 120. What may initially be small noise levels become significant on the output signal. Increasing the number of averages performed causes a significant improvement in the recorded signal (since the signal to noise ratio improves as the square root of the number of averages). Typically, signals were averaged 65 536 times with a digitiser capable of 30 000 averages per second. The Johnson noise level can be calculated using

$$V = \sqrt{4k_B T R \Delta f} \tag{3.3.7}$$

where Δf is the bandwidth and R is the equivalent resistance.

The Johnson noise due to the sample at T=1.6K (assuming a device resistance

of $1k\Omega$) is $\sim 3\mu$V, for a bandwidth of 100 MHz. The large bandwidth is necessary since the measurements involve very short voltage pulses. The Johnson noise due to the pre–amplifier is $\sim 9\mu$V. The Johnson noise from the pre–amplifier is generally much larger than that due to the sample owing to the temperature difference.

Another contribution to the noise arises due to the movement of carriers across potential barriers in the devices used and in the amplifier. This is Shot noise and adds to the Johnson noise. The Shot noise (along with flicker ($1/f$) noise) can be minimised by careful design of the electronics. For the pre–amps used in the experiments, the total noise level was $\sim 40\mu$V, much lower than the amplitude of the measured signals.

Any coherent noise (from the digitiser) is removed during the bias subtraction technique (described in Section 3.3.8). The electrical measurement circuit can also suffer from noise picked–up from sources external to the experiment. Radio signals and computers are two of the main culprits. To eliminate unwanted interference, the entire experimental set–up (apart from the PC used to record data and a scope) is enclosed within a screened room. The screened room is earthed independently of the mains.

REDUCTION OF PICK–UP

One of the major problems encountered in phonon emission and absorption experiments, where phonon time of flight traces are recorded, is the observation of electromagnetic pick–up on the measured signal. This occurs when the input pulse is detected by the detector circuitry, due to high frequency components in the pulse and the proximity of the wiring of the device and detector. Reduction of pick–up is a necessity if time of flight traces are to be of use.

The most widely employed technique used to reduce the effects of pick–up was "bias subtraction". In this method, the detector bias was reversed under IEEE control by a Philips PM 2122 switch unit. The required number of signal averages were performed for positive and negative bias. The method exploits the fact that

the pick–up signal does not change with bias whereas the phonon signal does. By subtracting one trace from another (an inbuilt feature of Scan), the resulting trace should be free from pick–up, with enhancement of the phonon signal.

A variant of the above method was to reverse the excitation pulse. In this case, the pick–up was reversed with the pulse, while the phonon signal remained the same. Averaging was performed as necessary and traces were added to one another in order to cancel the effects of pick–up. Bias subtraction and pulse reversal are illustrated in Figures 3.14 and 3.15.

Observing the pick–up shows that positive and negative spikes coincide with the rising and falling edges of the excitation pulse (which explains the strategies above). It is possible to reduce the pick–up by manipulation of the leading and trailing edges of the pulse and the pulse duration. Rounding the edges of the pulse has the effect of removing the high frequency components of the pulse. Since the sample is effectively a capacitor (heater or bolometer on one surface of the wafer with the device on the opposite surface separated by an insulator), the sample impedance is low for high frequencies–increasing the impedance (and so reducing the amount of input pulse the sample "sees") can be achieved by removing the high frequency components. Sloping the pulse edges reduces the pick–up but obviously degrades the input pulse (reducing the power). This can be compensated for by extending the pulse duration, which also extends the decay of the pick–up. If the pulse is too long, heating will occur.

The situation is complicated further by the structure of the samples studied. It is desirable to be able to resolve LA and TA modes separately, allowing time gating of the signals. In order to achieve this, the excitation pulse should not exceed the difference in time of flight of the two modes. In GaAs, the arrival of the first ballistic phonons for wafers of similar thickness will be observed ~70ns after the initial pulse. In the samples studied in this work, this time is reduced to around 40 ns. The difference in arrival time of the two modes is ~30ns. This further limits the use of manipulation of the pulse to reduce pick–up.

In order to reduce the pick–up, wires to the sample are kept as short and as

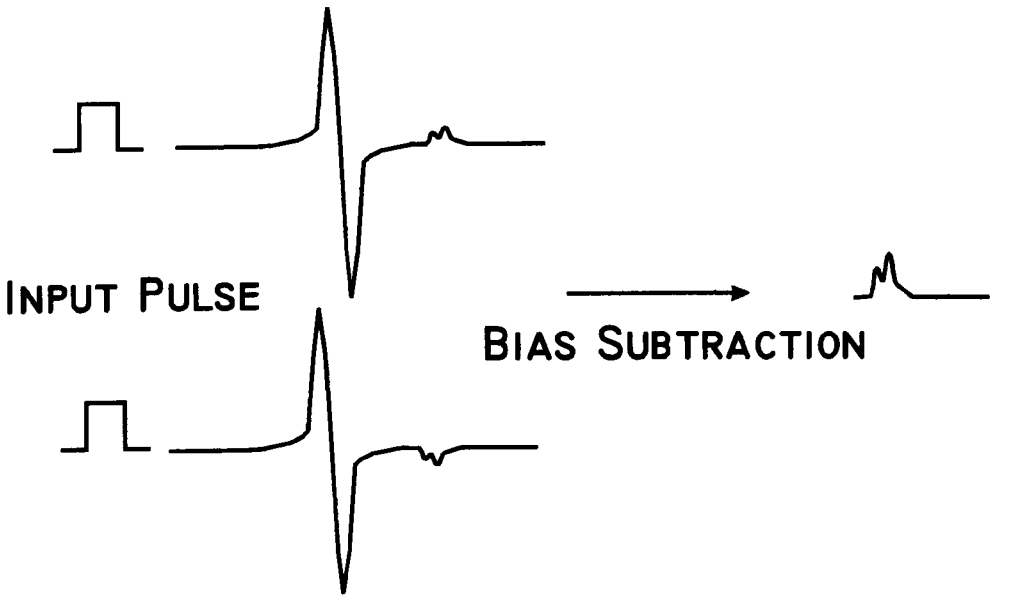

Figure 3.14: An illustration of the "bias subtraction" technique.

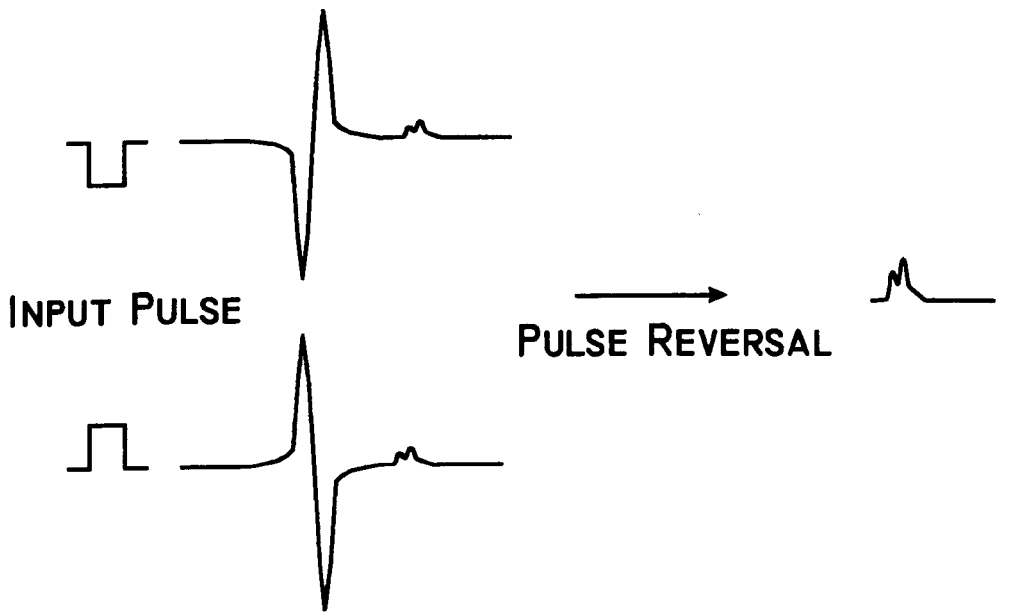

Figure 3.15: An illustration of the "pulse reversal" technique.

separated as possible. The geometry of the detectors, when possible, was chosen to reduce pick–up effects. By using serpentine bolometers, the pick–up in each arm cancels and the overall pick–up is reduced.

TIME OF FLIGHT TRACES

As mentioned above, the GaN on sapphire samples present additional problems in experimentation when compared to GaAs. GaAs structures are grown on GaAs substrates of high quality. The effects of the interface are small, and phonons propagate through the wafer with LA and TA velocities of $\sim$5500ms^{-1} and 3300ms^{-1} respectively. In GaN, these velocities are greater (the LA velocity is $\sim$6560ms^{-1} and the TA velocity is $\sim$2680ms^{-1}). In principle, this should make mode resolution straightforward, although as mentioned, the fast arrival of the LA mode has additional drawbacks. In reality, the situation is much worse. Typically, a GaN epilayer is $\sim 2\mu$m thick. The sapphire substrate is $\sim$0.4mm (polishing then reduces the thickness), and LA and TA phonon velocities are 11 100ms^{-1} and 6040ms^{-1} respectively. The time of flight is dominated by the substrate, and apart from an even faster LA arrival time, mode separation becomes more difficult.

Early heat pulse experiments were performed on layers as thick as 5 mm. This allowed individual modes to be resolved. To delay the observed LA signal by 10 ns in these samples requires either epilayers to be 20 times thicker or to increase the substrate thickness by 30%.

These effects are apparent in phonon imaging experiments. In order to produce the 2D map of phonon intensities, the phonon signal is gated, as is the baseline. For each point on the scan, the signal is averaged (to increase signal to noise ratio) and then averaged between the gate. The baseline is also averaged and subtracted from each signal so that baseline drift does not affect the results. Gating the signal presents an interesting problem. Gating the entire signal allows the overall focussing pattern to be obtained, but detailed structure is lost. Gating single modes has the disadvantage of "losing" signal intensity as the signal moves

to longer times at large angles to the normal (for LA) and enhancement of the TA mode caused by the LA signal moving into the gate. It is possible to resolve individual modes using a static gate if a good deal of patience is employed.

A recent adaptation of the Scan software allowed a "sliding gate" to be used. The thickness of the sample and the appropriate velocities are used to calculate the shift in arrival time of the ballistic signal at various angles and the gate is moved accordingly.

3.3.9 MEASUREMENTS IN MAGNETIC FIELD

The application of magnetic field to AlGaN/GaN systems can provide a wealth of information regarding the characteristics of the material. The observation of Shubnikov–de Haas oscillations (oscillations of device resistance as the field is varied) allows the carrier density and mobility to be extracted. Application of magnetic field to the GaN samples allows the effects of localisation and parallel conduction to be observed.

As discussed, the Spectromag cryostat houses a superconducting magnet capable of producing fields up to 7T. In the normal sample mounting configuration, this field was parallel to the c–axis. If required, the sample mounting arrangement could be changed such that the field was perpendicular to the c–axis. The sample was wired as for the lock–in temperature calibration, with a constant current passed through the sample and the voltage measured using a DMM. The magnetic field was measured by noting the current through the magnet as the field is swept, again using a DMM connected to the monitor output of the magnet power supply unit. The rate of field sweeping was typically 7T in 20 minutes, although this time could be extended to several hours if required. Transport measurements and phonon absorption experiments have been performed with applied magnetic fields. It was also necessary to perform temperature calibrations at zero and high field if a true comparison of behaviour was to be obtained.

3.3.10 PHOTOCONDUCTIVITY MEASUREMENTS

In AlGaN/GaN samples which showed no oscillations in resistance with field (G0–155, G0–164 and D982–AN26), illumination of the sample was performed. In similar AlGaAs/GaAs structures this was achieved by the use of a red LED. In this work, two sources of illumination were used; a halogen lamp and a UV source. Illumination caused a decrease in device resistance and was generally attributed to exciting carriers from defects to the conduction band.

Magnetic field sweeps were performed before and after illumination. Because the field sweeps were performed over 50 minutes, it was necessary to monitor the decay of the induced conductivity to ensure that the effect persisted over a greater time scale than the experiment. The sample was illuminated until no change in device resistance was observed. The light was removed, and the resistance was recorded over time. The measurement was repeated at room temperature.

REFERENCES

[1] P. Hawker, A. J. Kent, T. S. Cheng, and C. T. Foxon. *Physica B*, **263-264**, 227, (1999).

[2] C. Youtsey, I. Adesida, and G. Bulman. *Appl. Phys. Lett*, **71**, 2151, (1997).

[3] Q. Z. Liu and S. S. Lau. *Solid. State. Electron.*, **42**, 677, (1998).

[4] M. N. Wybourne and J. K. Wigmore. *Rep. Prog. Phys.*, **51**, 923, (1988).

[5] A. J. Kent. *Experimental Low Temperature Physics, Macmillan Press*, (1993).

[6] J. J. Harris, K. J. Lee, I. Harrison, L. B. Flannery, D. Korakakis, T. S. Cheng, C. T. Foxon, Z. Bougrioua, I. Moerman, W. Van der Stricht, E. J. Thrush, B. Hamilton, and K. Ferhah. *phys. stat. sol (a)*, **176**, 363, (1999).

[7] N. M. Stanton, A. J. Kent, A. V. Akimov, P. Hawker, T. S. Cheng, and C. T. Foxon. *J. Appl. Phys*, **89**, 973, (2001).

[8] A. J. Cross. *PhD Thesis, University of Nottingham*, (2001).

[9] S. A. Cavill. *PhD Thesis, University of Nottingham*, (2000).

Chapter 4

BULK GaN–RESULTS AND DISCUSSION

4.1 INTRODUCTION

This Chapter deals with the results of the experiments performed on GaN epilayers. All samples were grown on sapphire substrates. There are essentially four experiments which have been performed; energy relaxation, phonon emission, phonon absorption and phonon drag imaging. Although the basis of the experiments performed here is the same as used in the study of GaAs systems, the results presented here provide the first direct analysis of the individual phonon modes involved in emission and absorption processes in GaN. The imaging techniques which have been employed have drawn on previous studies of sapphire and extended to include the GaN epilayers. The energy relaxation measurements have been performed across a wide range of temperatures, extending far beyond the maximum temperatures achievable with other techniques. The results of each set of experiments will be presented separately. The results are compared with the theoretical predictions outlined in Chapter 2 and a discussion of the findings with reference to other relevant investigations is included where applicable. The Summary presents a brief recap of the experimental results.

4.2 ENERGY RELAXATION

4.2.1 INTRODUCTION

Energy relaxation experiments have been performed on a number of epilayers, the details of which are given in Table 4.1. A detailed discussion of the analysis steps will be presented for a typical sample, with a more concise presentation of other samples for completeness.

A disadvantage of this technique over direct phonon measurements (as described in the Section 3.3.5) is that the information obtained is integrated over all modes and directions. Although directional information can be obtained from the theoretical models, to experimentally study individual modes requires direct observation techniques. However, as will been seen in this Chapter, energy relaxation measurements provide valuable information regarding the crossover from acoustic to optic emission. This crossover occurs at a higher temperature and a much larger power per carrier than for GaAs, complicating the observation of this feature by ballistic phonon detection alone (due to the saturation of superconducting bolometers).

Sample Number	Layer Thickness (μm)	Electron density at 300 K (m^{-3})	Mobility at 300 K ($m^2V^{-1}s^{-1}$)
MG 588	0.9	5.70×10^{24}	0.0031
MG 610	3.7	2.20×10^{24}	0.014
MG 622	3.7	2.60×10^{24}	0.015
MG 657	1.4	1.13×10^{24}	0.0097
MG 675	1.4	6.40×10^{24}	0.02
MG 676	1.5	9.00×10^{24}	0.019
MG 716	2.0	9.20×10^{24}	0.011

Table 4.1: Material parameters of the GaN epilayers.

It is appropriate to use the room temperature carrier concentrations as determined from Hall measurements in these measurements due to the high electron densities – the variation of carrier density with temperature is small. In lower

density material, this is not necessarily the case, and in some samples, the carrier density has been observed to change by up to a factor of four from the room temperature value.

4.2.2 ENERGY RELAXATION CURVES

With the temperature calibration and the pulse measurement performed, as described in Section 3.3.4, the two results can be combined to produce plots of power dissipated against inverse electron temperature, as shown in Figure 4.1. There are three regions to consider; the "low–temperature" region, ranging from ~10K to ~50K, the "high–temperature" region for electron temperatures above ~130K and the "intermediate" region in–between. Let us first consider the low–temperature regime.

At low electron temperatures, energy loss occurs through emission of acoustic phonons. This low temperature regime can be further separated into two regions. At *very* low temperatures, in the Bloch–Grüneisen regime, characterised by electron temperatures $T_e \ll \hbar v_s k_F / k_B$, power loss is expected to be proportional to T_e^n. (In the range of densities studied, $T_e \ll$ 16K and 30K for LA modes for the lowest and highest densities respectively). The value of the exponent is determined by the coupling mechanism; n=3 and n=5 for unscreened PZ and DP coupling respectively. Inclusion of screening of the electron–phonon interaction serves to increase the value of the exponent, as can be seen by inspection of Equation 2.4.19. The region in which $T_e > 2\hbar v_s k_F / k_B$, is termed the "equipartition regime", [1]. In this range, analytic solutions of Equation 2.4.19 are possible and a linear dependence of power loss on temperature is predicted.

Owing to the wavevector dependences of the coupling mechanisms (PZ $\propto 1/q$, DP $\propto q$), one would expect DP coupling to dominate power loss as the electron temperature is raised and phonons of a higher wavevector are emitted. At what point the crossover from PZ to DP coupling occurs is determined by the ratio of the coupling constants. Using the accepted values of $C_{+1} \simeq$ 8.3eV and $C_{-1} \sim 9 \times 10^{-10}$ Jm^{-1}, the wavevector at which the crossover should occur is $\sim 10^9$ m^{-1};

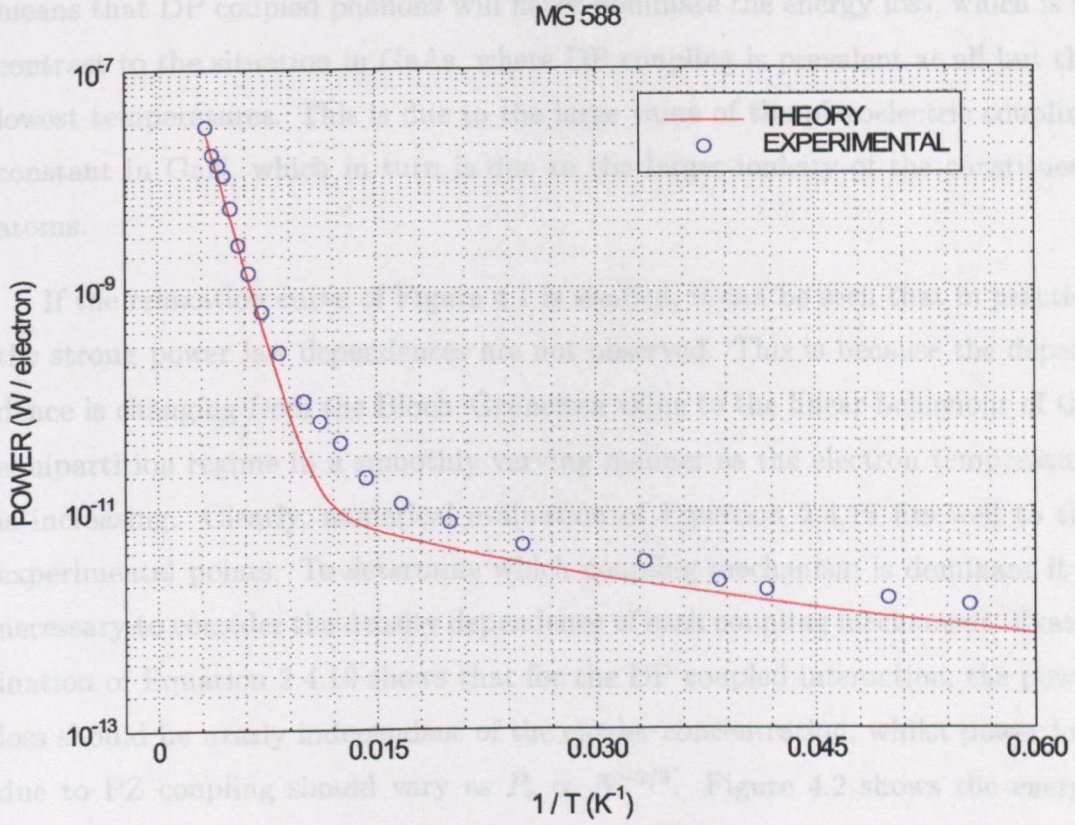

Figure 4.1: The power dissipated per carrier as a function of inverse electron temperature. The theoretical curve is a sum of the power loss from emission of transverse and longitudinal acoustic phonons and optic phonons, calculated from Equation 2.4.19 and Equation 2.4.41 but does not include screening of the interaction.

this corresponds to an electron temperature of ~40K. The maximum wavevector that can be emitted is limited by the $2k_F$ cut–off. For the highest carrier density studied in this work ($n = 9.2 \times 10^{24}$ m^{-3}), the maximum wavevector an acoustic phonon may have is $\sim 1.3{\times}10^9$ m^{-1}, which corresponds to a temperature of ~60K. In the lowest density sample, the equivalent temperature is $\sim$ 33K. This means that DP coupled phonons will never dominate the energy loss, which is in contrast to the situation in GaAs, where DP coupling is prevalent at all but the lowest temperatures. This is due to the large value of the piezoelectric coupling constant in GaN, which in turn is due to the larger ionicity of the constituent atoms.

If the relaxation curve of Figure 4.1 is studied, it can be seen that in practice the strong power law dependences are not observed. This is because the dependence is changing from the Bloch–Grüneisen value to the linear behaviour of the equipartition regime in a smoothly varying manner as the electron temperature is increasing. Clearly, numerical evaluation of Equation 2.4.19 fits well to the experimental points. To determine which coupling mechanism is dominant it is necessary to consider the density dependence of each coupling mechanism. Examination of Equation 2.4.19 shows that for the DP coupled interaction, the power loss should be nearly independent of the carrier concentration, whilst power loss due to PZ coupling should vary as $P_e \propto N^{-2/3}$. Figure 4.2 shows the energy relaxation rate as a function of carrier density. The electron temperature is 10K (T_l=1.6K). The theoretical line is calculated by evaluation of Equation 2.4.19 and the experimental points are taken from each of the samples studied. The density dependence shows that PZ coupling is indeed dominant at low temperatures.

In the previous graphs, the theoretical curves have been calculated without the inclusion of screening. The effect of screening on the power loss is shown in Figure 4.3. As can be seen clearly, the experimental points suggest that the interaction is unscreened in these systems. This is justified by consideration of two cut–offs. The first occurs when the phonon wavevector exceeds the inverse Debye screening length λ_D, as given in Equation 2.4.22. In the highest carrier density sample studied, this occurs for electron temperatures above ~13K and ~5K for

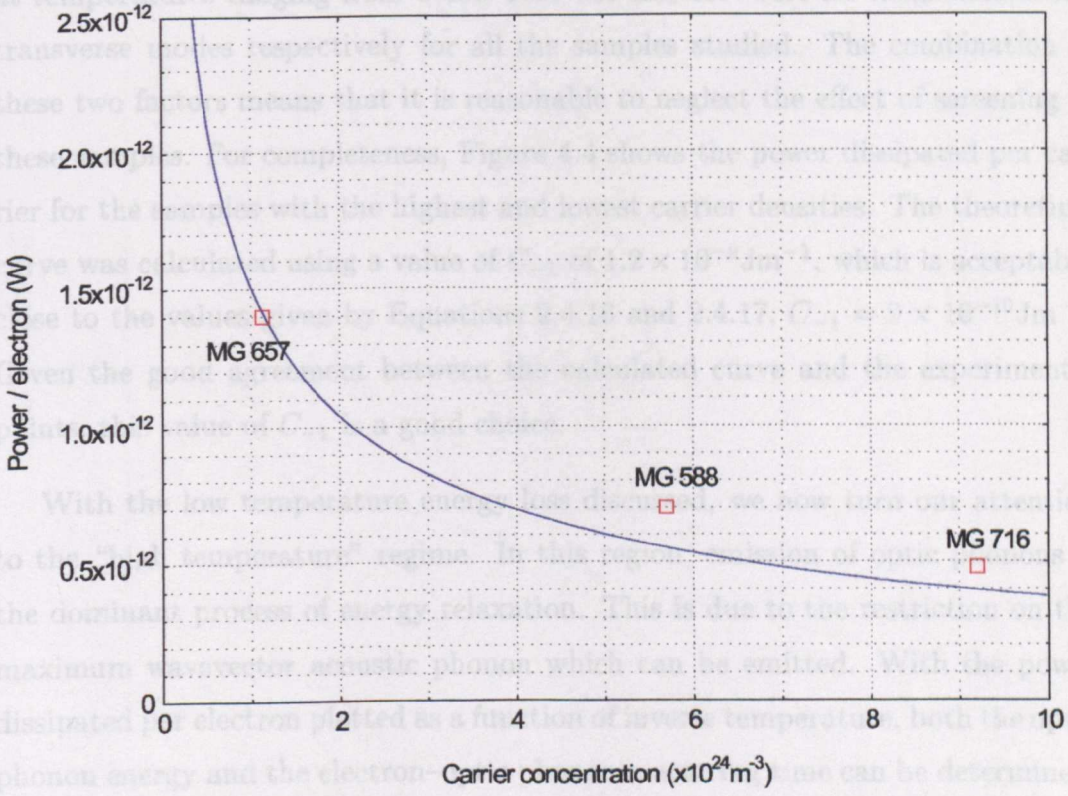

Figure 4.2: The power dissipated per carrier as a function of carrier concentration for an electron temperature of 10K. The theoretical curve is calculated from Equation 2.4.19.

longitudinal and transverse modes respectively. The second occurs in systems with strong defect and impurity scattering. The effective reduction in screening occurs when $q\ell$ <1, where ℓ is the electron mean free path, since the electrons cannot respond sufficiently quickly to screen the fields. The mobilities in the samples studied ranged from 31 to 200 $cm^2V^{-1}s^{-1}$, and the corresponding mean free paths therefore ranged from 1–8 nm. This corresponds to a reduction in screening at temperatures ranging from below 15K–3K and 6K–<1K for longitudinal and transverse modes respectively for all the samples studied. The combination of these two factors means that it is reasonable to neglect the effect of screening in these samples. For completeness, Figure 4.4 shows the power dissipated per carrier for the samples with the highest and lowest carrier densities. The theoretical curve was calculated using a value of C_{-1} of $1.2 \times 10^{-9}Jm^{-1}$, which is acceptably close to the values given by Equations 2.4.16 and 2.4.17, $C_{-1} = 9 \times 10^{-10}Jm^{-1}$. Given the good agreement between the calculated curve and the experimental points, this value of C_{-1} is a good choice.

With the low temperature energy loss discussed, we now turn our attention to the "high temperature" regime. In this region, emission of optic phonons is the dominant process of energy relaxation. This is due to the restriction on the maximum wavevector acoustic phonon which can be emitted. With the power dissipated per electron plotted as a function of inverse temperature, both the optic phonon energy and the electron–optic phonon scattering time can be determined. The relationship (as in Equation 2.4.41) is given again here for ease of reference (see, for example, [2]).

$$P_e = \frac{\hbar\omega_{LO}}{\tau} exp\left(\frac{-\hbar\omega_{LO}}{k_B T_e}\right)$$

Initially, the maximum amplitude voltage pulse that could be applied to the samples was 80V, and the device active area was 50×50μm. At these powers, and for samples with high carrier density, even at the maximum voltage, the electron temperature was not sufficiently high to fit the above expression to the experimental curves. For this reason, the active area was reduced to 10×10μm and the maximum voltage was increased to 160V using the amplifier described

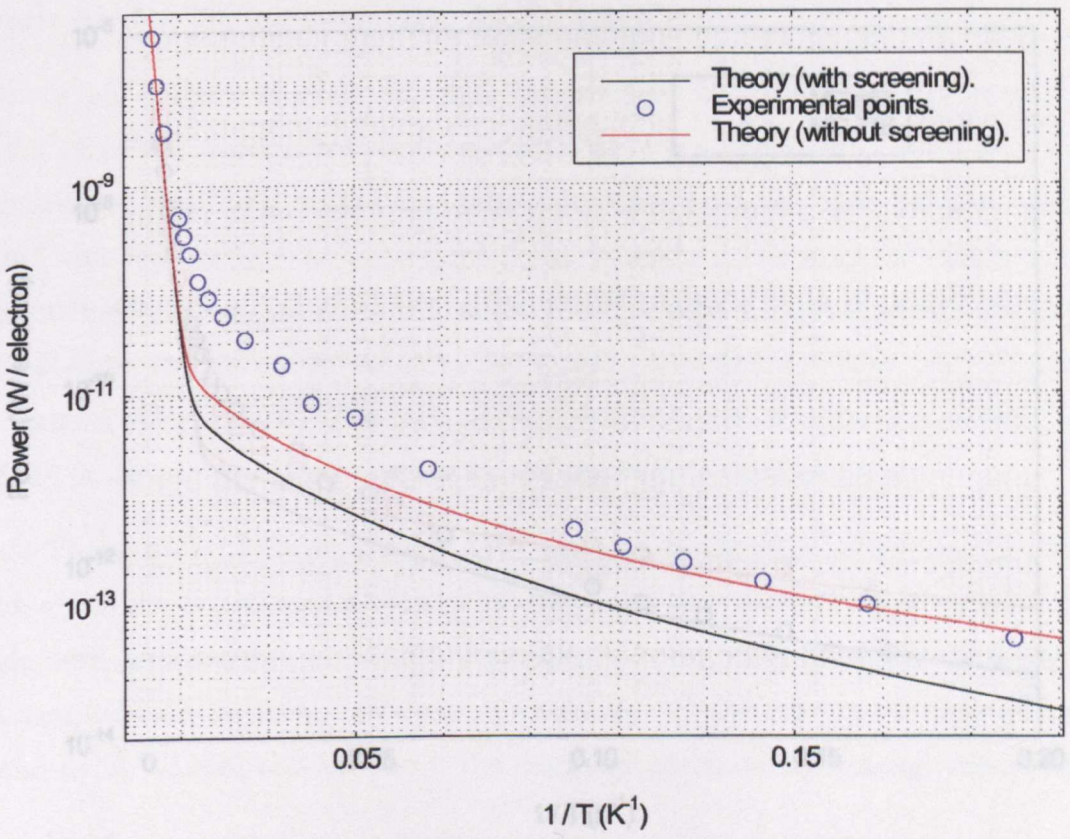

Figure 4.3: The effect of screening on the power loss (for sample MG 716). As can be seen, the experimental points are in much better agreement with the curve calculated without the inclusion of screening.

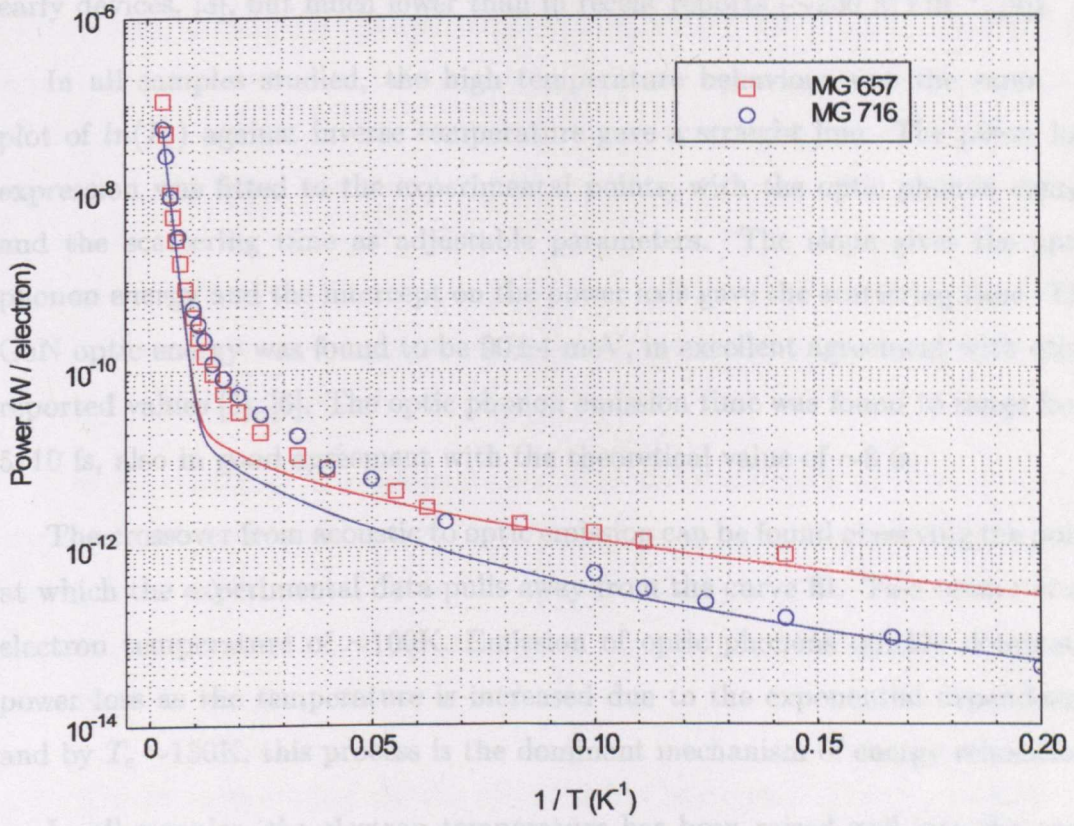

Figure 4.4: Energy relaxation rates as a function of electron temperature for the lowest and highest carrier density samples. As can be seen, the theory curves agree well with both samples.

in Section 3.3.3. This allowed the carriers to be heated to an extent such that optic emission was the dominant energy loss mechanism. Indeed, pulsing the smaller samples at the higher voltages resulted in the destruction of many of the samples studied, which allowed the determination of the breakdown field of the samples. Typically, the devices failed when the applied voltage was $\sim$ 120V. This corresponds to a field of $\sim$12 MVm^{-1}, comparable with the value obtained in early devices, [3], but much lower than in recent reports ($\sim$230 MVm^{-1}, [4]).

In all samples studied, the high temperature behaviour was the same. A plot of $ln(P_e)$ against inverse temperature gave a straight line. The power loss expression was fitted to the experimental points, with the optic phonon energy and the scattering time as adjustable parameters. The slope gives the optic phonon energy and the intercept on the power axis gave the scattering time. The GaN optic energy was found to be 90$\pm$4 meV, in excellent agreement with other reported values [5], [6]. The optic phonon emission time was found to range from 5–10 fs, also in good agreement with the theoretical value of $\sim$8 fs.

The crossover from acoustic to optic emission can be found observing the point at which the experimental data pulls away from the curve fit. This occurs at an electron temperature of $\sim$100K. Emission of optic phonons quickly dominates power loss as the temperature is increased due to the exponential dependence, and by T_e $\sim$130K, this process is the dominant mechanism of energy relaxation.

In all samples, the electron temperature has been raised well into the optic emission region. In high carrier density GaAs, when the electron temperature is very high, the energy relaxation rate is seen to decrease as the temperature increases, a phenomenon termed the "hot–phonon effect" [7], [8], [9]. As the electron temperature increases, so does the number of electrons capable of emitting an optic phonon. As previously discussed, optic phonons are almost dispersionless; the group velocity is practically zero. So for energy loss to occur, the emitted optic phonon must downconvert via anharmonic interactions to a high frequency acoustic mode and a TO phonon, which then downconverts to another acoustic phonon. As the electrons emit more optic phonons, a situation is reached where the energy relaxation rate is limited by the time taken for downconversion to

occur. In this non–equilibrium phonon distribution, the probability of phonon re–absorption by the electron gas is increased due to an increase in the local lattice temperature, and so the time taken to dissipate the power increases.

Experimentally, this effect would manifest itself as an increase in the relaxation time τ in the energy relaxation curves. In GaAs, a scattering time of ~3ps was obtained using the same experimental technique. For the GaN samples studied, even at the highest temperatures and for the highest densities, the experimental points sit on the theoretical curve. This suggests that hot–phonon effects are not present in these samples, in contrast to other studies on GaN epilayers [10], [11] (and probably accounts for the large value of τ_{e-LO} in [12]). It is possible that by raising the electron temperature further, allowing more high temperature points to be added, would allow any deviation from the theory curve to be observed. However, as previously mentioned, samples were often destroyed during this high voltage pulse measurement.

The experimental measurements and theoretical calculations agree well with one another in the extremes of the temperature range. The mid–temperature region, from ~30K to ~100K, is more enigmatic. In all of the samples studied, the measured energy loss rates are greater than the predicted values. There are three possible causes of the observed behaviour;

1. The samples studied exhibit strong defect scattering. The $2k_F$ momentum relaxation selection rule could be relaxed, allowing acoustic phonons to contribute to energy loss at higher electron temperatures than expected.

2. There is enhanced emission due to coupled LO phonon–plasmon modes, evidence of which has been observed in GaAs [13], [14], [15] and also in Raman studies of this material [16], [17].

3. Unlike the situation in GaAs, emission of TO phonons is possible in wurtzite GaN.

Since both the TO phonons and the coupled modes have a lower energy than the optic phonon, both of these modes could contribute to the energy loss in

the temperature range of interest. The possible mechanisms for describing the observed behaviour will be discussed separately.

Relaxation of the $2k_F$ cut–off would allow acoustic phonon emission at higher temperatures than would be expected. Due to smearing of the Fermi surface at high temperatures, this cut–off will never be very sharp. The $2k_F$ cut–off is relaxed when $(2k_F)^{-1} \geq \ell$, where ℓ is the electron mean free path. This is dependent on both the carrier density and the mobility. Figure 4.5 shows the energy relaxation rate for the highest and lowest mobility samples, with the theory line corresponding to the average carrier density in the two materials.

The mean free path of an electron is given by

$$\ell = v_F \tau \tag{4.2.1}$$

where v_F is the Fermi velocity $(= (2E_F/m^*)^{1/2})$ and τ is the mean scattering time, given by

$$\tau = \frac{m^* \mu}{e} \tag{4.2.2}$$

For a carrier density of $n = 6{\times}10^{24}\mathrm{m}^{-3}$, the condition for relaxation of the $2k_F$ cut–off will be satisfied for mobilities of $\mu \leq 0.003$. This is a similar mobility to that of MG 588 ($\mu = 0.0031$). Therefore, one would expect to observe the largest deviation from theory in the mid–temperature region in the lower mobility sample. As can be seen in Figure 4.5, this is clearly not the case. There is no correlation between the deviation from theory and mobility; relaxation of the $2k_F$ cut–off is unlikely to be the only cause of the observed deviation.

Phonon coupled modes have been discussed in Section 3.3.7. As described, these modes cause enhanced energy relaxation at lower temperatures than by bare LO phonon emission alone. Because plasmon modes also have a characteristic decay time, it may be possible to observe these modes by considering the "slope" of the high temperature data in the same manner as the optic phonon scattering time was obtained–fitting Equation 2.4.41 over the mid–temperature range might be expected to reveal the energy of the coupled mode and its decay time. However, due to the weighting of emission as given in Equation 2.4.44, at high temperatures

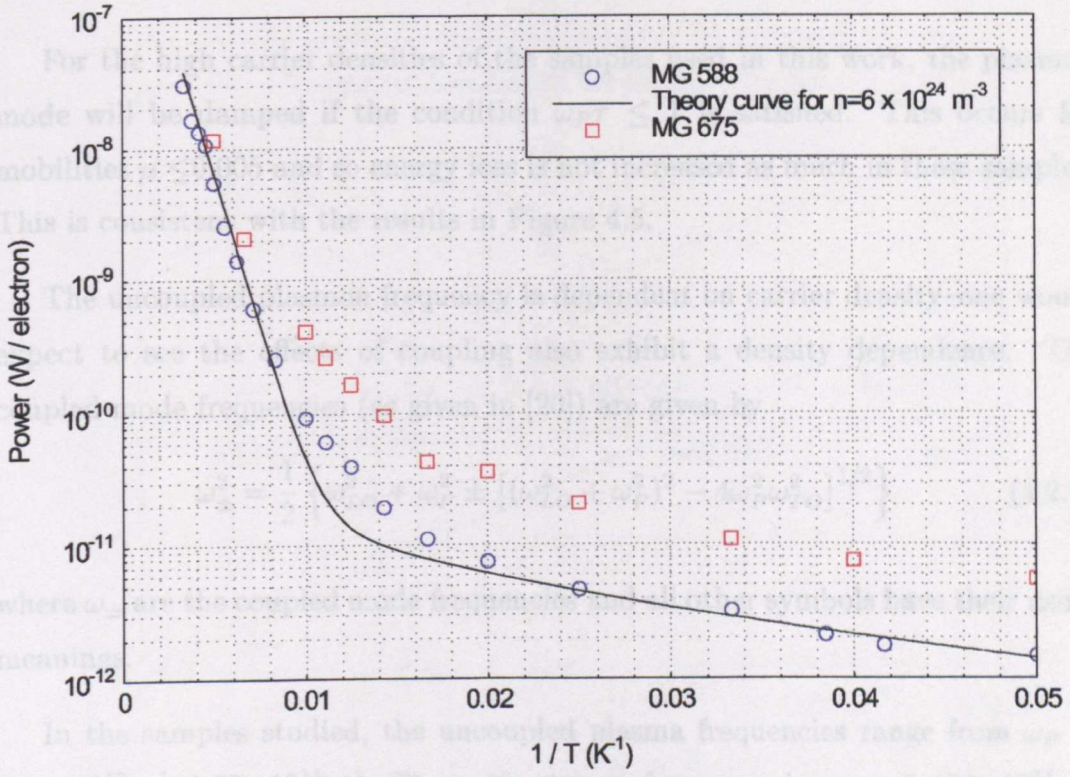

Figure 4.5: Energy relaxation rates as a function of electron temperature for the lowest and highest mobility samples. The theory curves is calculated for the average carrier density in the samples.

the emission is dominated by the bare LO–like mode. Relaxation due to emission of plasmon coupled modes will therefore not be evident from τ values alone [18], [19].

The bare plasmon frequency is given by (as in Equation 2.4.43)

$$\omega_p^2 = \sqrt{\frac{Ne^2}{m^*\varepsilon_\infty}}$$

For the high carrier densities of the samples used in this work, the plasmon mode will be damped if the condition $\omega_P\tau \leq 1$ is satisfied. This occurs for mobilities $\mu \leq 0.005$ and so energy loss is not increased as much in these samples. This is consistent with the results in Figure 4.5.

The uncoupled plasmon frequency is dependent on carrier density–one would expect to see the effects of coupling also exhibit a density dependence. The coupled mode frequencies (as given in [20]) are given by

$$\omega_\pm^2 = \frac{1}{2}\left\{\omega_{LO}^2 + \omega_P^2 \pm \left[(\omega_{LO}^2 + \omega_P^2)^2 - 4\omega_P^2\omega_{TO}^2\right]^{1/2}\right\} \qquad (4.2.3)$$

where $\omega_\pm$ are the coupled mode frequencies and all other symbols have their usual meanings.

In the samples studied, the uncoupled plasma frequencies range from $\omega_P \sim 5.4 \times 10^{13}\text{s}^{-1}$–$1.65\times10^{14}\text{s}^{-1}$. The optic phonon frequency is $\omega_{LO} \sim 1.402\times10^{14}\text{s}^{-1}$ for comparison. Figure 4.6 shows the dependence of the uncoupled and coupled plasmon frequencies as a function of carrier density.

In the highest carrier density samples studied, the plasmon frequency is greater than the LO phonon frequency, whereas in the lowest density samples the optic frequency is greater than ω_P. Following the argument of Das Sarma (as outlined in Section 3.3.7), the coupled mode can be considered as a phonon–like mode and a plasmon–like mode. Figure 4.6 shows that at low densities, $\omega_+ \sim \omega_{LO}$ and $\omega_- \sim \omega_P$, and at high densities $\omega_+ > \omega_{LO}$ and $\omega_- < \omega_P$. Thus at low electron densities, the mode frequency is similar to that of the bare LO phonon and the energy relaxation rate should be close to that predicted by theory.

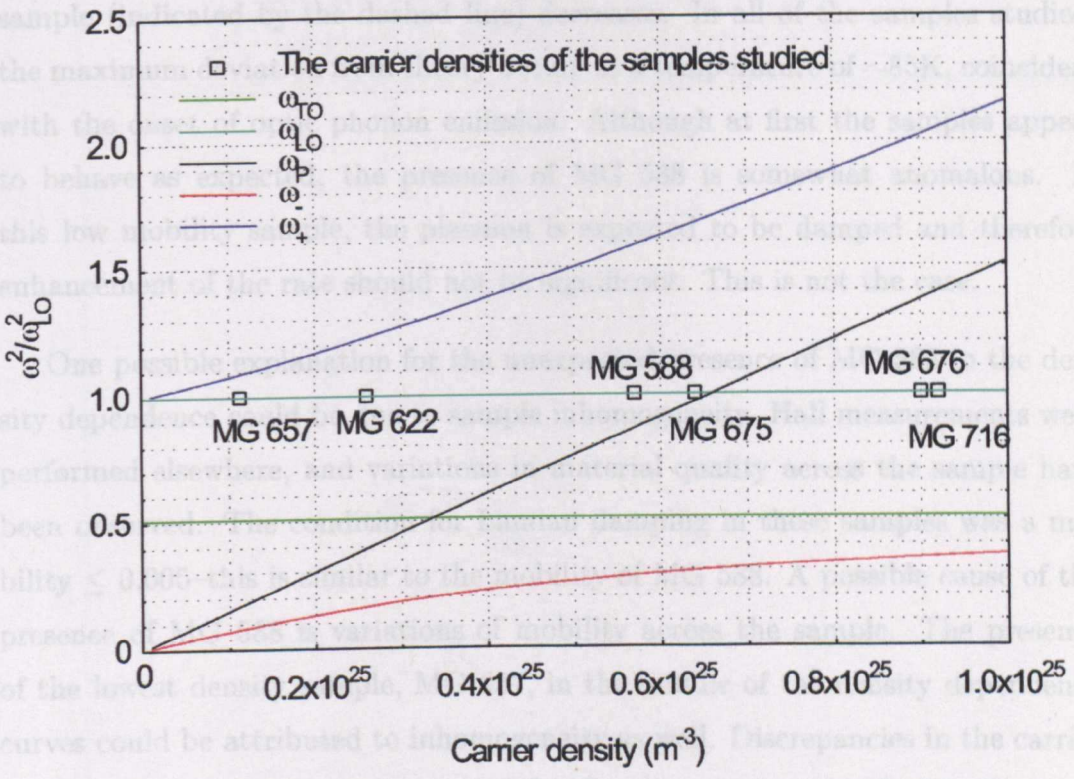

Figure 4.6: Coupled mode and bare plasma frequencies as a function of carrier density (from evaluation of Equation 4.2.3).

In the range of samples studied, the plasma frequency crosses through the optic phonon frequency. By considering the inequality, $\omega_P \tau \leq 1$, it is seen that in all but one sample, the plasmon coupled mode should not be damped. Figure 4.7 shows the ratio of the experimental rate and predicted energy loss as a function of carrier density. The solid lines are guides to the eye. As can be seen from the Figure, there is a carrier density dependence on the deviation from theory. As the carrier density is lowered, the ratio of experiment and theory in all but one sample (indicated by the dashed line) decreases. In all of the samples studied, the maximum deviation from theory occurs at a temperature of ~85K, coincident with the onset of optic phonon emission. Although at first the samples appear to behave as expected, the presence of MG 588 is somewhat anomalous. In this low mobility sample, the plasmon is expected to be damped and therefore enhancement of the rate should not be significant. This is not the case.

One possible explanation for the unexpected presence of MG 588 in the density dependence could be due to sample inhomogeneity. Hall measurements were performed elsewhere, and variations in material quality across the sample have been observed. The condition for Landau damping in these samples was a mobility ≤ 0.005–this is similar to the mobility of MG 588. A possible cause of the presence of MG 588 is variations of mobility across the sample. The presence of the lowest density sample, MG 657, in the middle of the density dependence curves could be attributed to inhomogeneity as well. Discrepancies in the carrier density could, in principle, be responsible for the position of MG 657. However, if the relaxation curves shown in Figure 4.4 are considered, then it is clear that at high and low temperatures, the experimental and theory curves agree well. If the carrier density was erroneous, the experimental curve would be shifted along the y–axis direction. The thickness and dimensions are known accurately. The effect of increasing the carrier concentration is seen in Figure 4.8.

The effect is quite clear. While the data retains its "shape", the re–calculated theory curve shows a different dependence on temperature. Since MG 657 matches theory well at high and low temperatures, there is no justification for attributing the deviation from theory to variations in carrier density.

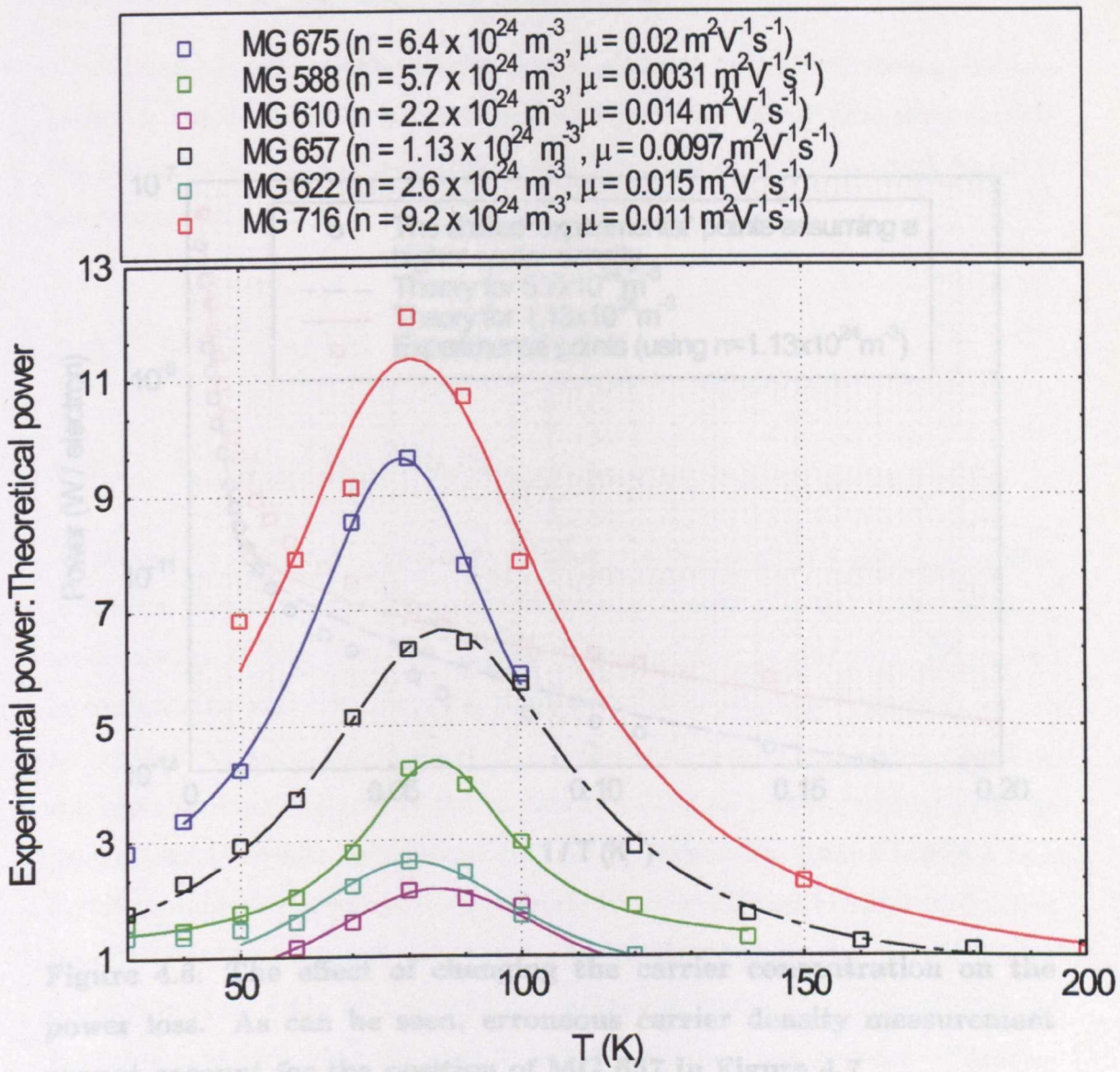

Figure 4.7: The ratio of measured energy loss and predicted values as a function of electron temperature.

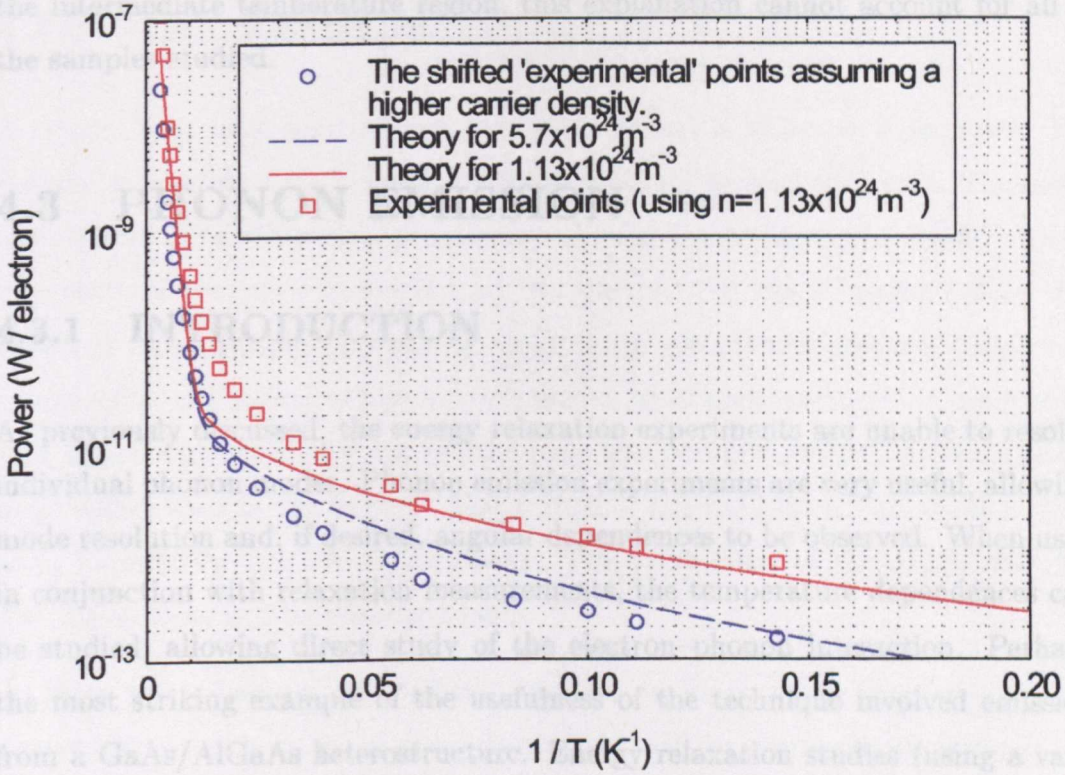

Figure 4.8: The effect of changing the carrier concentration on the power loss. As can be seen, erroneous carrier density measurement cannot account for the position of MG 657 in Figure 4.7

The final possibility for the enhancement of energy loss rate is due to the emission of TO phonons, which is allowed in wurtzite GaN. Since there should be no mobility dependence on the strength of this process, TO phonon emission cannot account for the energy loss in this region.

Although is seems likely that emission of plasmon–coupled modes is a probable cause for the deviation in experimental and predicted energy relaxation rates in the intermediate temperature region, this explanation cannot account for all of the samples studied.

4.3 PHONON EMISSION

4.3.1 INTRODUCTION

As previously discussed, the energy relaxation experiments are unable to resolve individual phonon modes. Phonon emission experiments are very useful, allowing mode resolution and, if desired, angular dependences to be observed. When used in conjunction with relaxation measurements, the temperature dependences can be studied, allowing direct study of the electron–phonon interaction. Perhaps the most striking example of the usefulness of the technique involved emission from a GaAs/AlGaAs heterostructure. Energy relaxation studies (using a variety of techniques including PL, transport, IR emission and Shubnikov–de Haas measurements) agreed well with theory, but predicted the dominance of LA DP coupled modes. Only by resolving the individual modes was it found that the LA mode was *very* weak and that in fact TA emission was stronger. A number of studies concerning the "missing mode" have since been performed [21], [22].

Emission results presented here consist of work performed using two samples, MG 588 and MG 657 (both Si doped samples). Two types of bolometric detection were used; MG 588 utilised the superconducting aluminium bolometer while MG 657 was studied with both an aluminium and a CdS bolometer. As discussed in Section 3.3.5, this means more information at high electron temperatures is

available for MG 657.

The same samples that were used in the energy relaxation measurements were used in emission experiments. This allows direct comparison with the results obtained previously. The devices were pulsed as earlier described, which allows the signals to be studied with respect to power/electron or to electron temperature.

4.3.2 THE RESULTS

A typical heat pulse signal (after bias subtraction) is shown in Figure 4.9. The bolometer was fabricated directly opposite the GaN device active area. The peaks corresponding to the arrival of ballistic LA and TA phonons are clearly visible. The start of the pulse is marked on the Figure. For the following ~35ns, the effects of electrical pick–up can be seen. Since the phonon signal is very small compared to the electrical pick–up, the technique of bias subtraction is employed. Any apparently small difference in the pick–up upon bias reversal appears as the large spikes seen in the Figure. The arrival of the ballistic LA phonons is then seen, followed by the TA phonon peak. The appearance of the signal after the TA arrival time will be discussed later.

With the bolometer appropriately biassed, as discussed in Section 3.3.5, the analysis method must be decided upon. As will be discussed in Section 4.5, careful consideration must be given to this subject. The standard method is to gate the signal and to average the signal between the gates. The difficulty arises in choosing the position of the gates [23]. In emission experiments where the device is electrically pulsed, the phonon source is fixed. This alleviates one of the potential problems since the changes in times of flight observed in imaging experiments will not occur here. The high phonon velocities in sapphire and the thickness of the substrates used means that, in general, the phonon peaks are not well separated as in other systems, where not only is the ratio of velocities favourable, but thicker substrates have been used. (For comparison, assuming a 400μm GaAs substrate, the LA and TA arrival times are $\sim$ 72ns and $\sim$ 121ns respectively). However, it is still possible to gate the rising edges of the ballistic

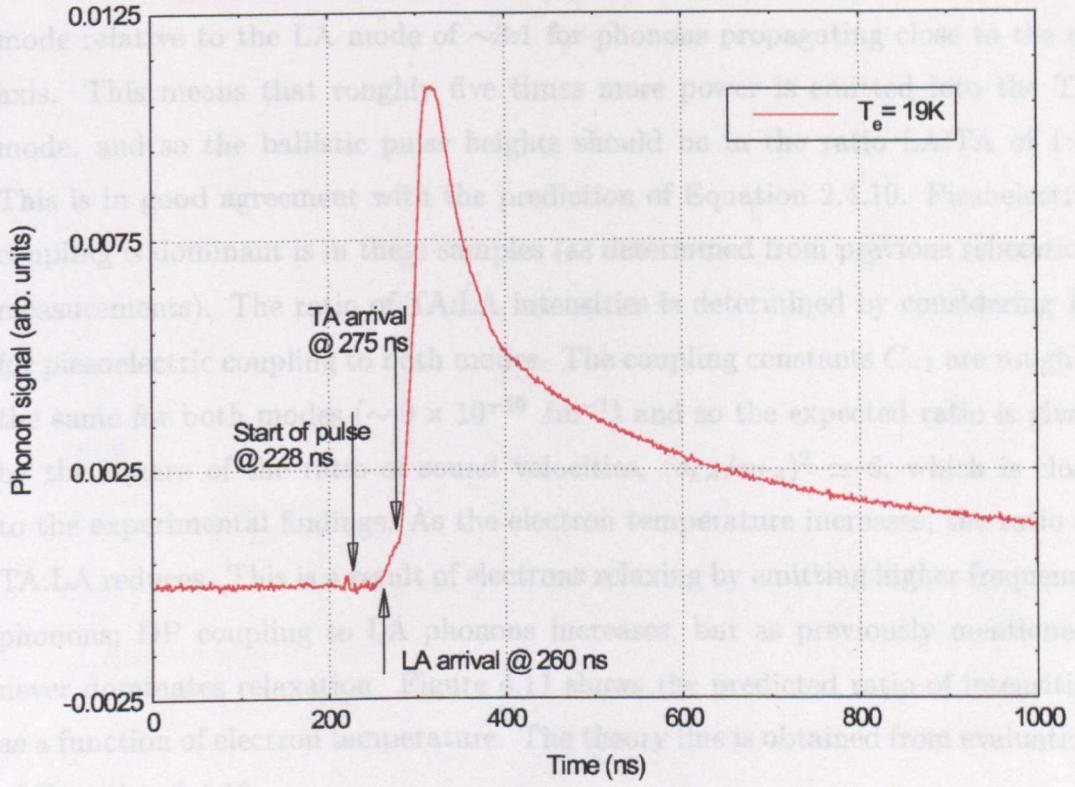

Figure 4.9: A typical heat pulse signal. The start of the pulse is marked, along with the ballistic arrival times.

peaks, a method which has been employed in this work, along with using the peak heights taken directly from the heat pulse traces.

Figure 4.10 shows heat pulse signals for MG 657, in the low power regime where $T_e \leq 31$K. The ballistic LA and TA phonon peaks are visible. The LA signal is appearing as the small shoulder on the rising edge of the TA signal. Considering the peak heights, the ratio of LA:TA is approximately 1:15 at the lowest power. The focussing effects of the sapphire substrate cause an enhancement of the TA mode relative to the LA mode of ~3:1 for phonons propagating close to the c–axis. This means that roughly five times more power is emitted into the TA mode, and so the ballistic pulse heights should be in the ratio LA:TA of 1:5. This is in good agreement with the prediction of Equation 2.4.19. Piezoelectric coupling is dominant is in these samples (as determined from previous relaxation measurements). The ratio of TA:LA intensities is determined by considering P_e for piezoelectric coupling to both modes. The coupling constants C_{-1} are roughly the same for both modes ($\sim 9 \times 10^{-10}$ Jm^{-1}) and so the expected ratio is given by the square of the ratio of sound velocities, $(v_{LA}/v_{TA})^2 \simeq 6$, which is close to the experimental findings. As the electron temperature increases, the ratio of TA:LA reduces. This is a result of electrons relaxing by emitting higher frequency phonons; DP coupling to LA phonons increases, but as previously mentioned, never dominates relaxation. Figure 4.11 shows the predicted ratio of intensities as a function of electron temperature. The theory line is obtained from evaluation of Equation 2.4.19.

The next set of heat pulse signals was obtained in the intermediate electron temperature region, from T_e ~40K–100K. Figure 4.12 shows the heat pulse signals as the electron temperature is raised. In this set of curves, in addition to the ballistic peaks, a third peak around ~450ns is observed. The presence of a peak in the tail of the signal, occurring at roughly three times the arrival time of the ballistic phonons is generally attributed to reflected phonons. These are phonons which reach the bolometer after multiple reflections [24]. This peak in the tail is not to be confused with a general increase in tail intensity, which will be discussed shortly.

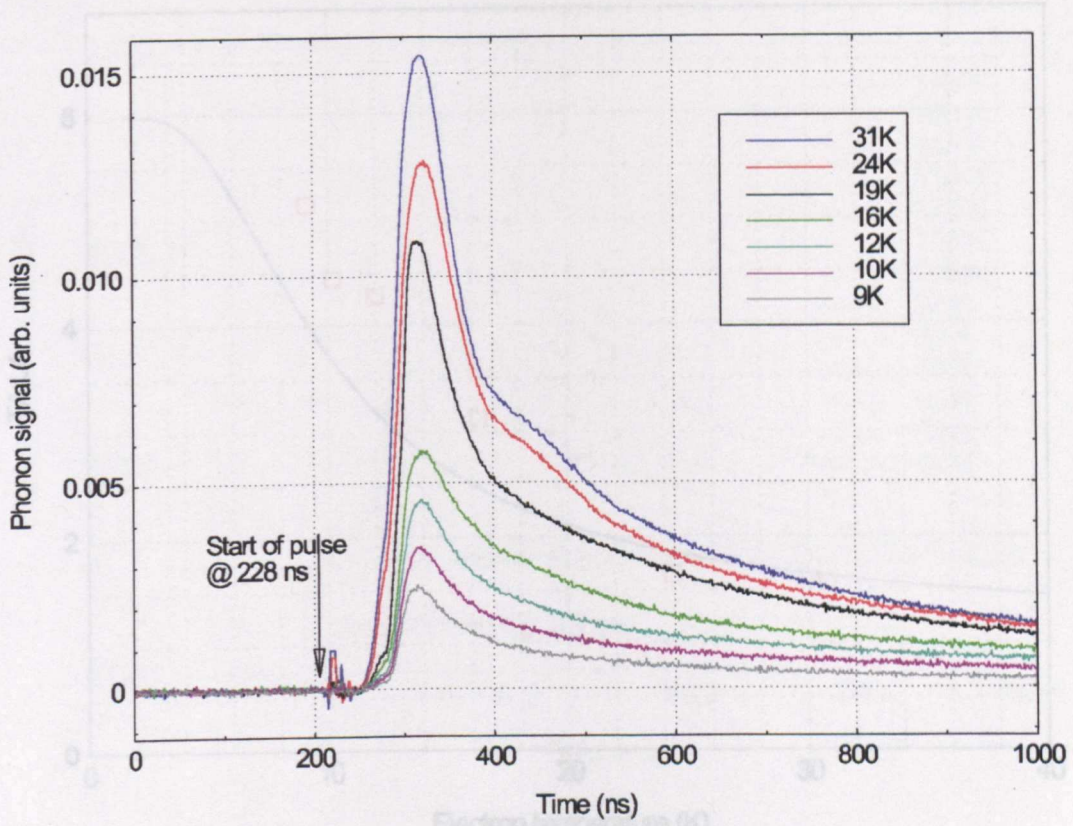

Figure 4.10: The low power traces for MG 657, obtained using an aluminium bolometer as a detector.

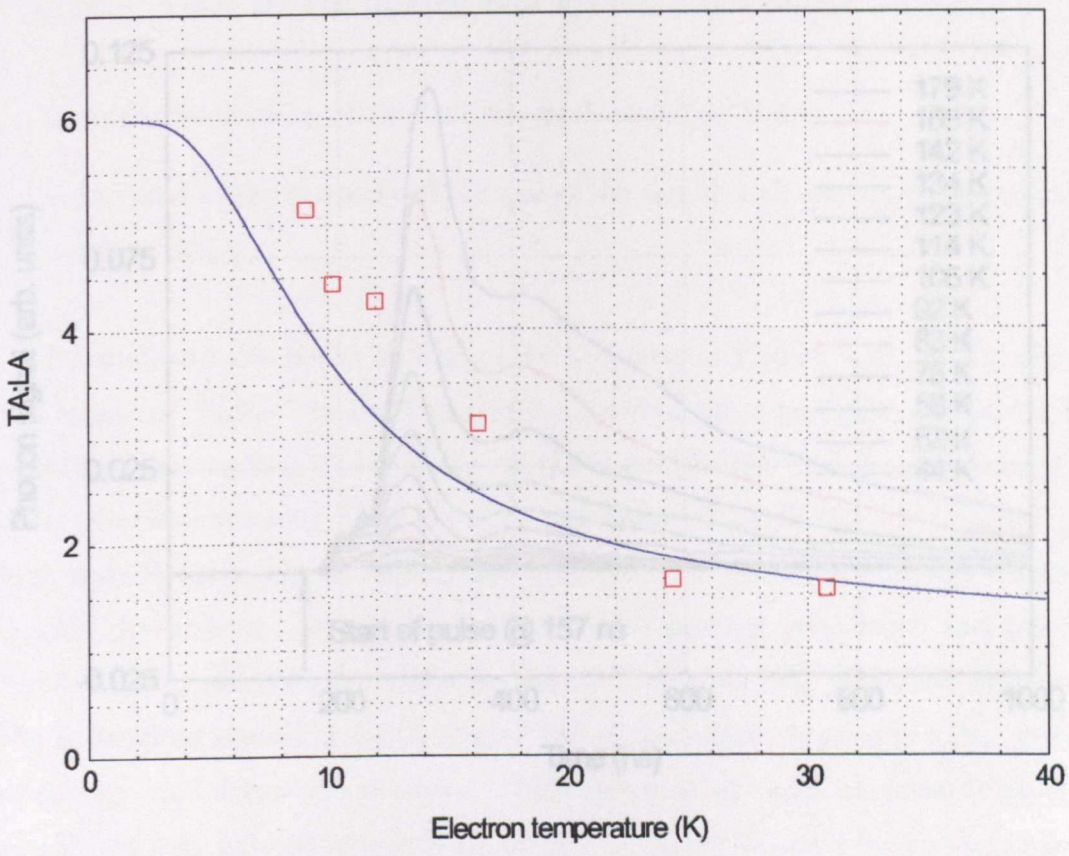

Figure 4.11: Ratio of mode heights TA:LA as a function of electron temperature compared with the results of the theory (solid line).

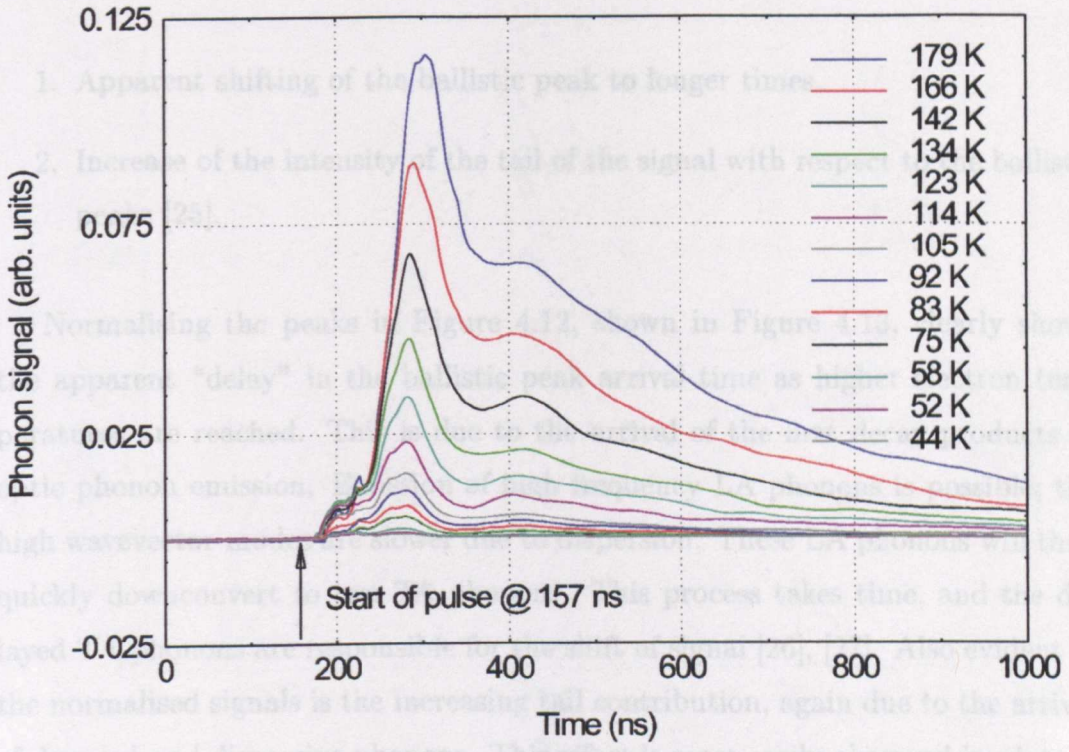

Figure 4.12: Signals obtained in the intermediate electron temperature regime. The third peak, due to the arrival of reflected phonons can be clearly seen.

A closer inspection of the signals in Figure 4.12 shows the ballistic TA peak appearing to shift to longer times. Since the arrival time of the ballistic peak is obviously determined only from the TA velocity and the substrate thickness, the shifted peak is indicative of a change in the nature of the emission process. Optic phonons have a *very* low velocity, and energy relaxation by this process requires the decay of these modes into acoustic phonons which can be detected by the bolometer. There are two characteristic signs of optic emission occurring;

1. Apparent shifting of the ballistic peak to longer times.
2. Increase of the intensity of the tail of the signal with respect to the ballistic peaks [25].

Normalising the peaks in Figure 4.12, shown in Figure 4.13, clearly shows the apparent "delay" in the ballistic peak arrival time as higher electron temperatures are reached. This is due to the arrival of the first decay products of optic phonon emission. Emission of high frequency LA phonons is possible; the high wavevector modes are slower due to dispersion. These LA phonons will then quickly downconvert to two TA phonons. This process takes time, and the delayed TA phonons are responsible for the shift of signal [26], [27]. Also evident in the normalised signals is the increasing tail contribution, again due to the arrival of decayed and dispersive phonons. This effect is most easily observed in plots of signal intensity against temperature or P_e–the change of slope indicates a change in emission process, as in [28].

From Figure 4.12 another feature is visible on the TA peak. For electron temperatures as low as 44K, the peak appears to be split. At first, one might attribute the splitting to the arrival of FTA and STA modes. However, along directions of high symmetry, these modes are degenerate. It has been previously suggested that this first peak is the true ballistic signal due to ballistic TA phonon arrival and that the second peak is further evidence of downconverted products [23].

The normalised traces of Figure 4.10, shown in Figure 4.14, there is also

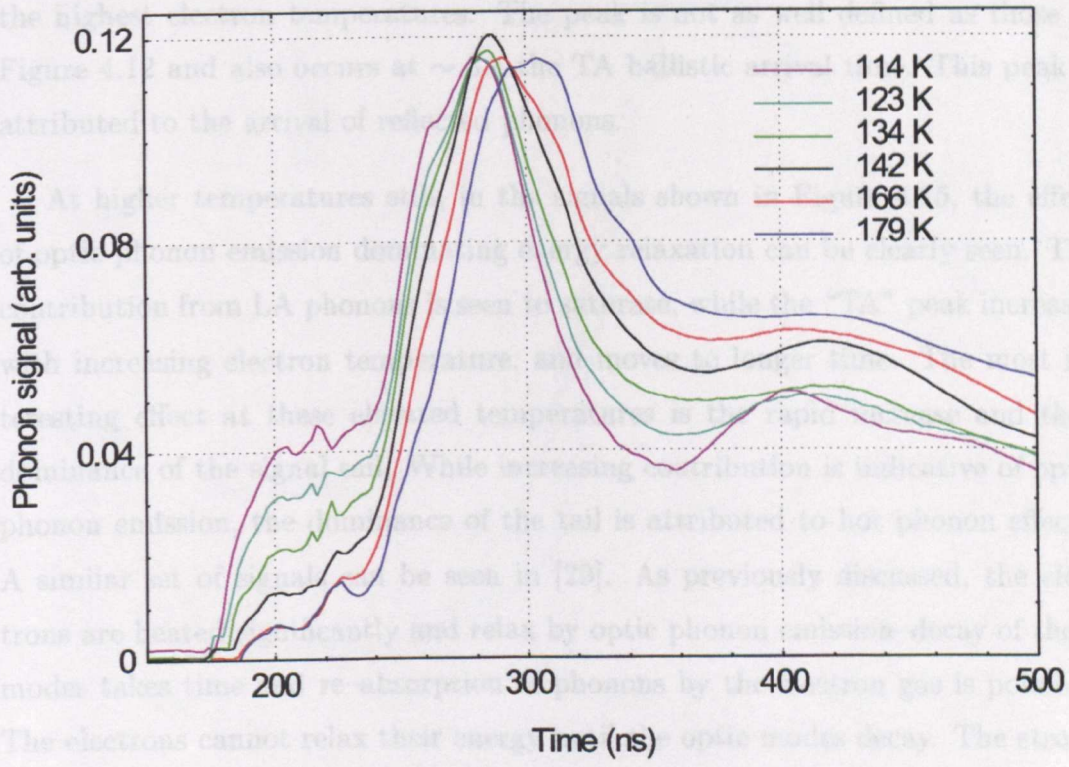

Figure 4.13: Normalised signals showing the shifting of the TA ballistic peak arrival time in MG 657.

evidence of the "TA" peak shifting to longer times. At these low temperatures, the crossover to optic phonon emission has not occurred. This could be further evidence of the emission of plasmon coupled modes. These coupled modes decay into acoustic phonons which arrive at the bolometer slightly delayed from the ballistic peak. If the decay products of coupled modes are responsible then, in principle, one should be able to observe them as two "crossovers" in a plot of intensity against power. A third "peak" in the tail of the signal appears at the highest electron temperatures. The peak is not as well defined as those in Figure 4.12 and also occurs at $\sim 3\times$ the TA ballistic arrival time. This peak is attributed to the arrival of reflected phonons.

At higher temperatures still, in the signals shown in Figure 4.15, the effect of optic phonon emission dominating energy relaxation can be clearly seen. The contribution from LA phonons is seen to saturate, while the "TA" peak increases with increasing electron temperature, and moves to longer time. The most interesting effect at these elevated temperatures is the rapid increase and then dominance of the signal tail. While increasing contribution is indicative of optic phonon emission, the dominance of the tail is attributed to hot phonon effects. A similar set of signals can be seen in [29]. As previously discussed, the electrons are heated significantly and relax by optic phonon emission–decay of these modes takes time and re–absorption of phonons by the electron gas is possible. The electrons cannot relax their energy until the optic modes decay. The strong phonon–phonon scattering results in a much delayed and broadened signal. The tail of the signal is dominant at $T_e \sim 200$K. This corresponds to a power dissipation of $P_e \sim 8\times10^{-9}$W. These effects were not observable in the energy relaxation experiments, as the devices failed before enough data was collected that the effects of an increased electron temperature could be seen. Figure 4.16 shows the ballistic TA intensity as a function of power dissipated. The increase in intensity starts to fall away at a power of $\sim 4 \times 10^{-9}$ W/electron, corresponding to an electron temperature of $\sim$ 100K. Again, this is indication of the onset of optic phonon emission. The appearance of the third "peak" in the low power traces is therefore due to reflections

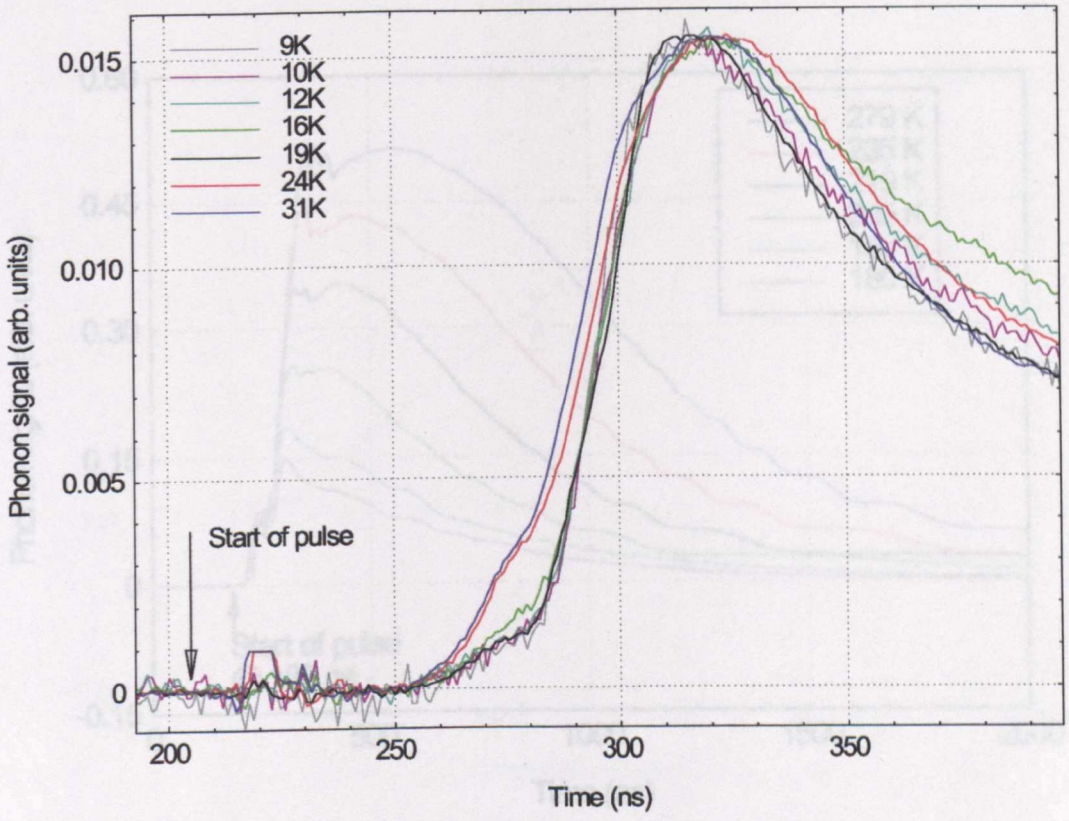

Figure 4.14: Normalised signals showing the apparent shifting of the TA ballistic peak arrival time for lower electron temperatures in MG 657.

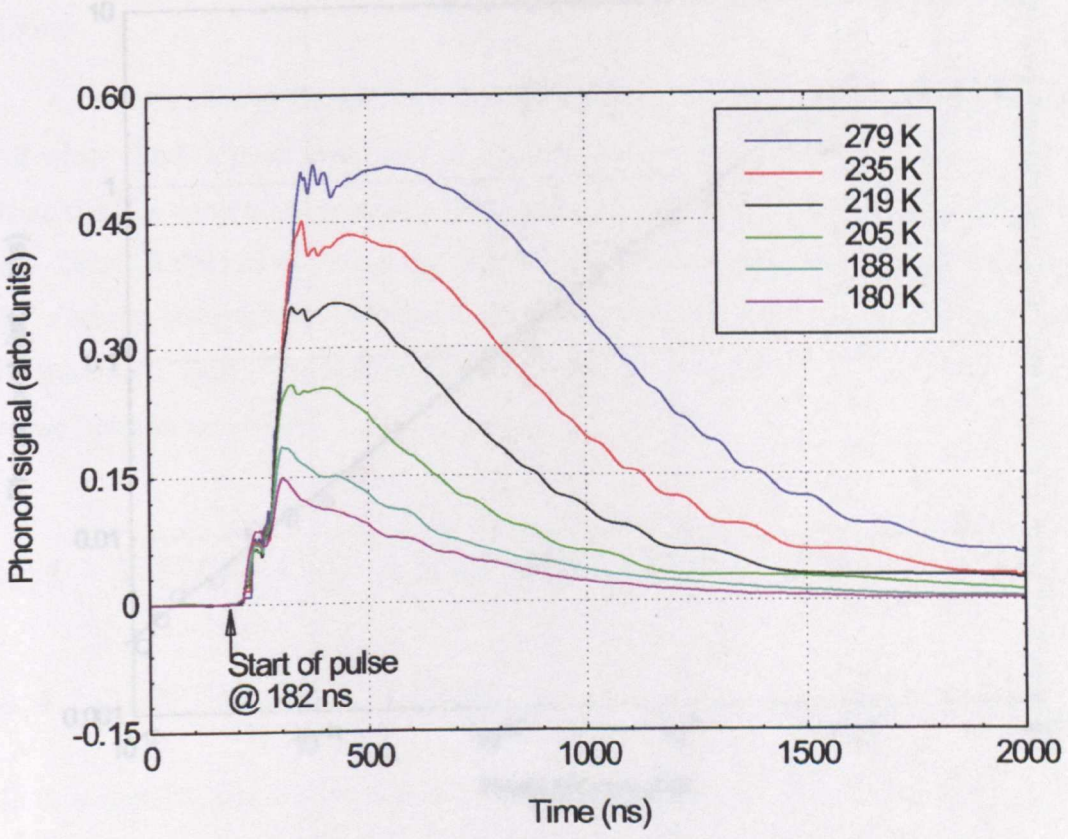

Figure 4.15: Normalised signals showing the apparent shifting of the TA ballistic peak arrival time in MG 657.

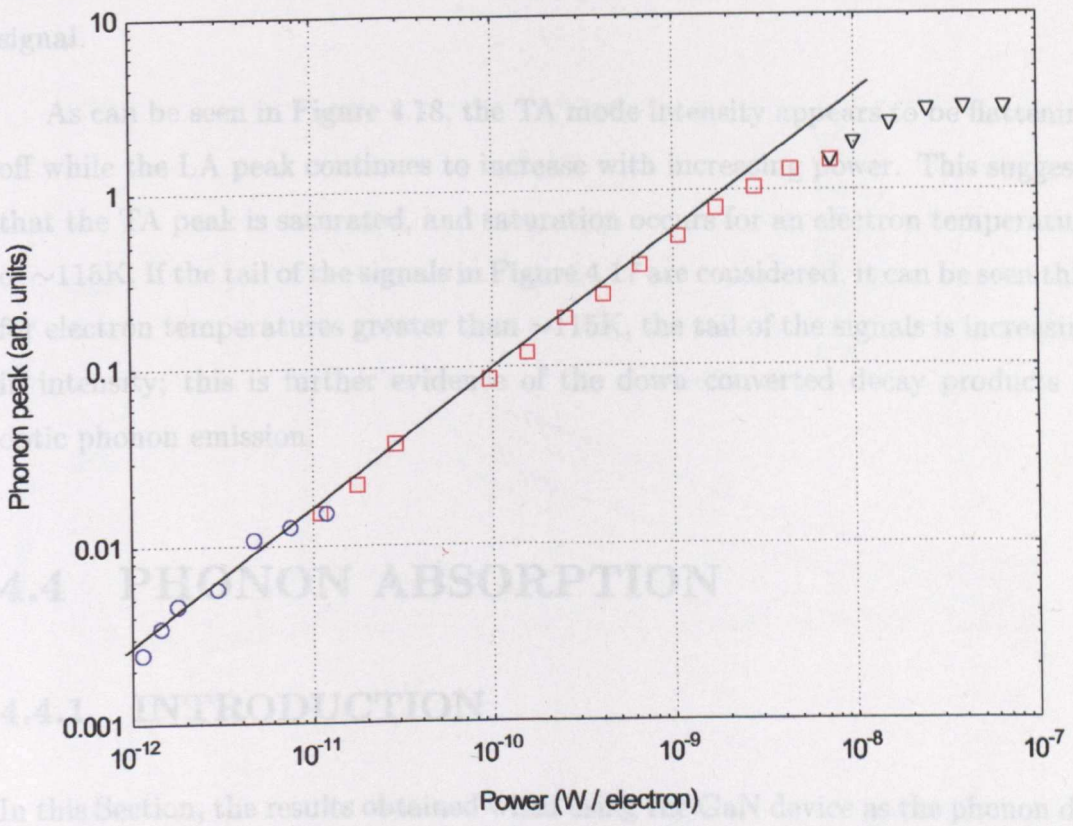

Figure 4.16: The TA ballistic peak intensity as a function of power dissipated per electron for MG 657. The three different symbols represent the low, intermediate and high temperature measurements. The line is a guide to the eye.

The heat pulse signals obtained by pulsing MG 588 are shown in Figure 4.17. Again, LA and TA ballistic peaks are clearly visible and are better resolved than in MG 657. The same characteristics are observed. Immediately noticeable is the relative intensity of LA:TA – the ballistic LA signal is much stronger in this sample. An obvious reason for the apparent increase in LA:TA , which was not observed in MG 657 in the same temperature region, is saturation of the TA signal.

As can be seen in Figure 4.18, the TA mode intensity appears to be flattening off while the LA peak continues to increase with increasing power. This suggests that the TA peak is saturated, and saturation occurs for an electron temperature of ~115K. If the tail of the signals in Figure 4.17 are considered, it can be seen that for electron temperatures greater than ~115K, the tail of the signals is increasing in intensity; this is further evidence of the down–converted decay products of optic phonon emission.

4.4 PHONON ABSORPTION

4.4.1 INTRODUCTION

In this Section, the results obtained when using the GaN device as the phonon detector are presented. The advantage of absorption experiments over emission for direct study of the electron–phonon interaction is that in emission, the electrons are heated above the lattice temperature, whereas in absorption, the electrons and lattice are at the same low temperature. The result is that thermal broadening effects are less important in absorption experiments, and consequently the cut–off of the interaction should be sharper. The experiment requires two measurements to be made; the variation of heat pulse signal with heater voltage and also a temperature calibration of the device. Absorption experiments were performed on a number of samples (MG 588, 657, 676 and 716), with material parameters given in Table 4.1. All results described in this Section were obtained by electrical pulsing of a metal heater, and experiments have been performed under a variety

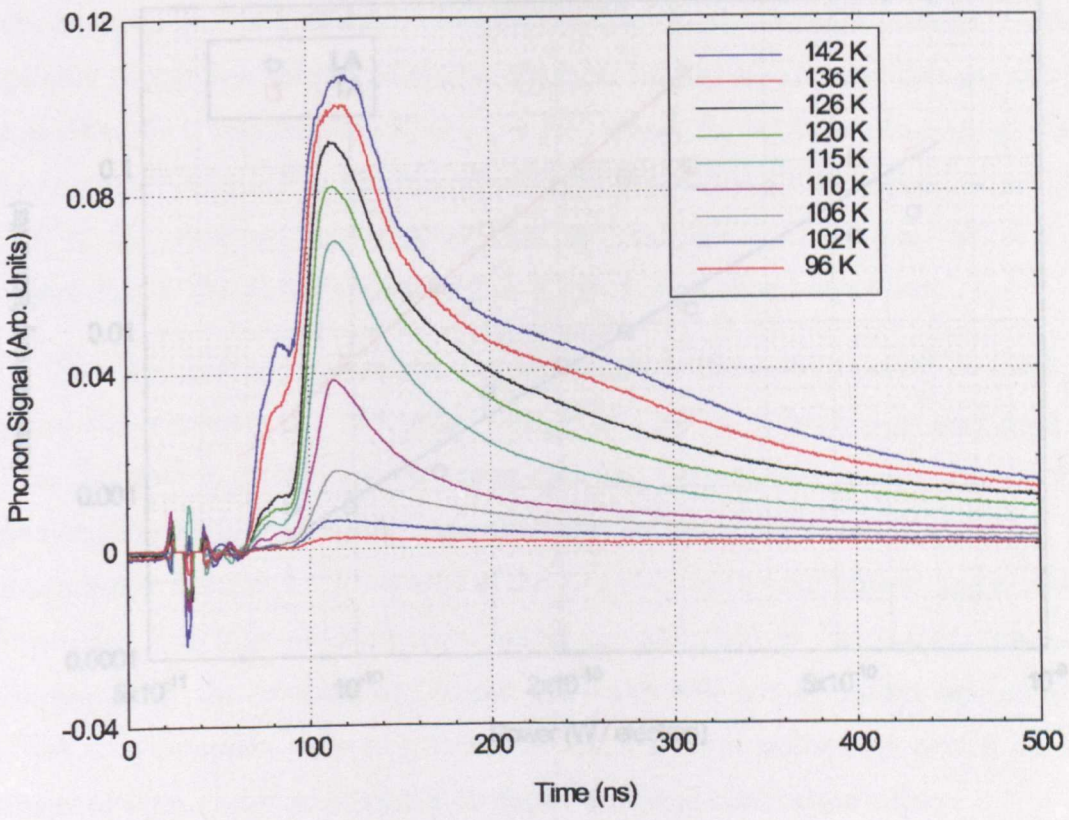

Figure 4.17: Heat pulse signals for MG 588.

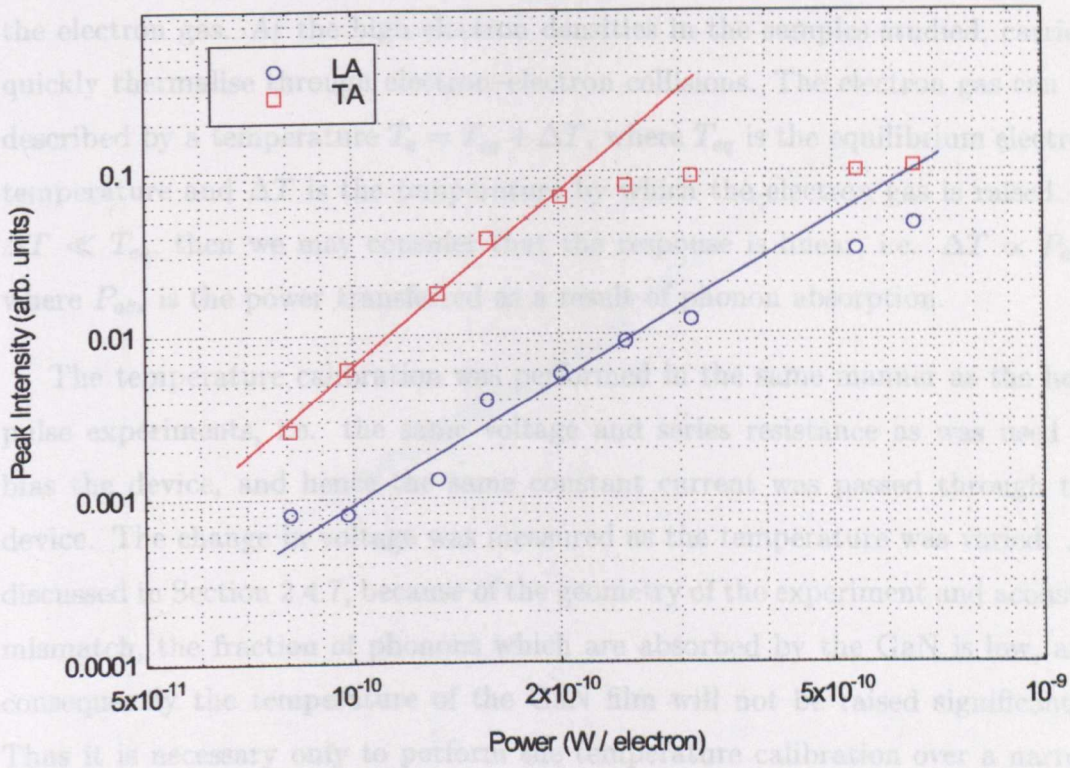

Figure 4.18: TA and LA mode intensities as a function of power per electron for MG 588 (the solid lines are a guide to the eye).

of conditions; at base temperature, 1.6K, with applied magnetic field and with the samples illuminated. Absorption studies using optical excitation techniques will be discussed in the following Section.

4.4.2 TEMPERATURE CALIBRATION

Absorption of non–equilibrium phonons in the GaN epilayer results in heating of the electron gas. At the high electron densities in the samples studied, carriers quickly thermalise through electron–electron collisions. The electron gas can be described by a temperature $T_e = T_{eq} + \Delta T$, where T_{eq} is the equilibrium electron temperature and ΔT is the temperature by which the electron gas is raised. If $\Delta T \ll T_{eq}$, then we may consider that the response is linear, i.e. $\Delta T \propto P_{abs}$, where P_{abs} is the power transferred as a result of phonon absorption.

The temperature calibration was performed in the same manner as the heat pulse experiments, i.e. the same voltage and series resistance as was used to bias the device, and hence the same constant current was passed through the device. The change in voltage was measured as the temperature was varied. As discussed in Section 2.4.7, because of the geometry of the experiment and acoustic mismatch, the fraction of phonons which are absorbed by the GaN is low, and consequently the temperature of the GaN film will not be raised significantly. Thus it is necessary only to perform the temperature calibration over a narrow range of temperatures. Figure 4.19 shows a typical calibration curve.

4.4.3 THE RESULTS

Figure 4.20 shows a set of phonoconductivity traces, obtained using MG 588. As with emission experiments, there are two peaks, corresponding to LA and TA modes. The modes are clearly resolved. As in emission, signals are obtained by bias reversal and subtraction. One of the major difficulties in the analysis is well illustrated in the Figure. Electrical pick–up is clearly visible and persists for ~35 ns after the start of the pulse. The arrival time of the LA phonons is also ~35

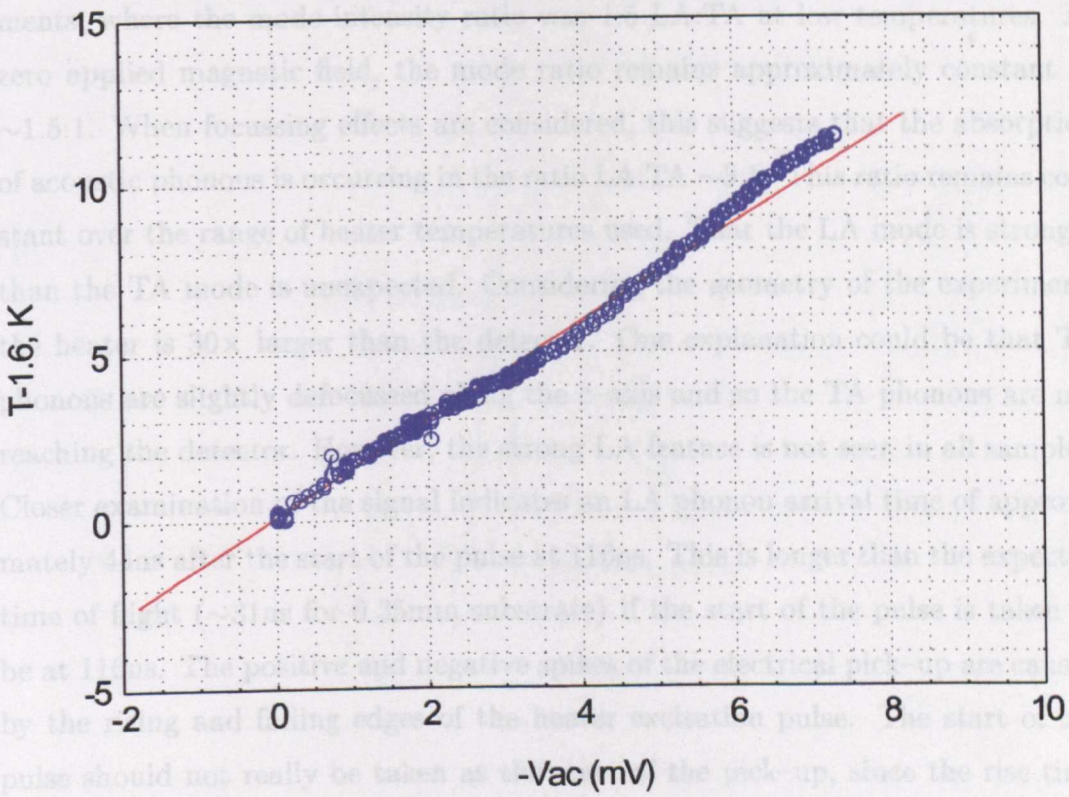

Figure 4.19: A typical temperature calibration curve.

ns, slightly faster than in the emission experiments (due to the substrate being a little thinner). The result is that pick–up obscures the rising edge of the LA peak. Although the arrival time can be calculated, gating the signal becomes difficult and inaccurate. Signals have been recorded at zero bias in an attempt to minimise pick–up effects, although this is not practical in all experiments.

At the first look, the most noticeable difference in these traces is the relative intensity of the LA and TA modes. This is in contrast with emission experiments, where the mode intensity ratio was 1:5 LA:TA at low temperatures. At zero applied magnetic field, the mode ratio remains approximately constant at ~1.5:1. When focussing effects are considered, this suggests that the absorption of acoustic phonons is occurring in the ratio LA:TA ~5:1. This ratio remains constant over the range of heater temperatures used. That the LA mode is stronger than the TA mode is unexpected. Considering the geometry of the experiment, the heater is 30× larger than the detector. One explanation could be that TA phonons are slightly defocussed along the c–axis and so the TA phonons are not reaching the detector. However, the strong LA feature is not seen in all samples. Closer examination of the signal indicates an LA phonon arrival time of approximately 44ns after the start of the pulse at 116ns. This is longer than the expected time of flight (~31ns for 0.35mm substrate) if the start of the pulse is taken to be at 116ns. The positive and negative spikes of the electrical pick–up are caused by the rising and falling edges of the heater excitation pulse. The start of the pulse should not really be taken as the start of the pick–up, since the rise time of the heater pulse should also be considered. It is, therefore, more appropriate to take the start of the pulse at the peak of the first "pick–up spike". The group velocity is also direction dependent. Taking these points into consideration leads to the signals occurring at the expected arrival times but does not explain the ratio of signal intensities.

Using the theory outlined in Section 2.4.7, for low heater temperatures, when $3k_BT_h \ll \hbar\omega_{max}$, the dependence of intensity on T_h is described by $\Delta V \propto T_h^{\alpha}$. For piezoelectric coupling, α=5, while for deformation potential, α=7. The inclusion of screening increases the exponent. At higher heater temperatures, when

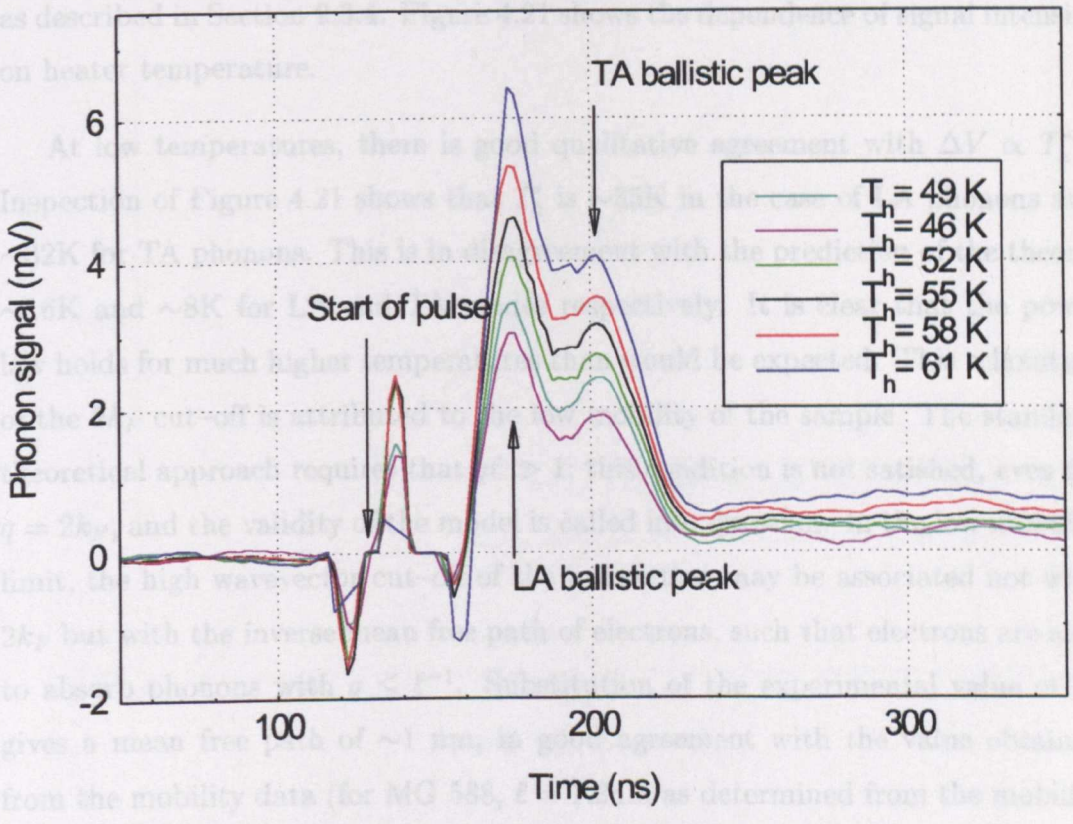

Figure 4.20: Heat pulse signals for several heater temperatures.

$3k_BT_h > \hbar\omega_{max}$, the equipartition regime is entered and a linear dependence of intensity on heater temperature is expected. The crossover from the power law dependence occurs at a temperature T_h', given by

$$T_h' \simeq \frac{2\hbar v_s k_F}{3k_B} \tag{4.4.1}$$

Gating the signals on the rising edge allows plots of signal intensity against heater voltage to be obtained. The heater voltage is converted into a temperature as described in Section 2.3.4. Figure 4.21 shows the dependence of signal intensity on heater temperature.

At low temperatures, there is good qualitative agreement with $\Delta V \propto T_h^{\sim 5}$. Inspection of Figure 4.21 shows that T_h' is ~35K in the case of LA phonons and ~32K for TA phonons. This is in disagreement with the prediction of the theory, ~16K and ~8K for LA and TA modes respectively. It is clear that the power law holds for much higher temperatures than would be expected. This relaxation of the $2k_F$ cut–off is attributed to the low mobility of the sample. The standard theoretical approach requires that $q\ell \gg 1$; this condition is not satisfied, even for $q = 2k_F$, and the validity of the model is called into question. In the low mobility limit, the high wavevector cut–off of the interaction may be associated not with $2k_F$ but with the inverse mean free path of electrons, such that electrons are able to absorb phonons with $q \leq \ell^{-1}$. Substitution of the experimental value of T_h' gives a mean free path of ~1 nm, in good agreement with the value obtained from the mobility data (for MG 588, $\ell = 1.2$nm as determined from the mobility data).

Illumination of the sample had no significant effect on either the signal intensity or the temperature dependence. Application of magnetic field (up to 6T) was seen to increase the signal intensity, while the temperature dependence remained, with α ~5. However, the ratio of modes was affected. Although the LA mode is still more intense, as the heater power is increased, the ratio of LA:TA decreases slightly with increasing heater temperature, as shown in Figure 4.22. The signals recorded with magnetic field show a more pronounced TA peak.

The behaviour of the absorption signal (from MG 588) whilst the field is be-

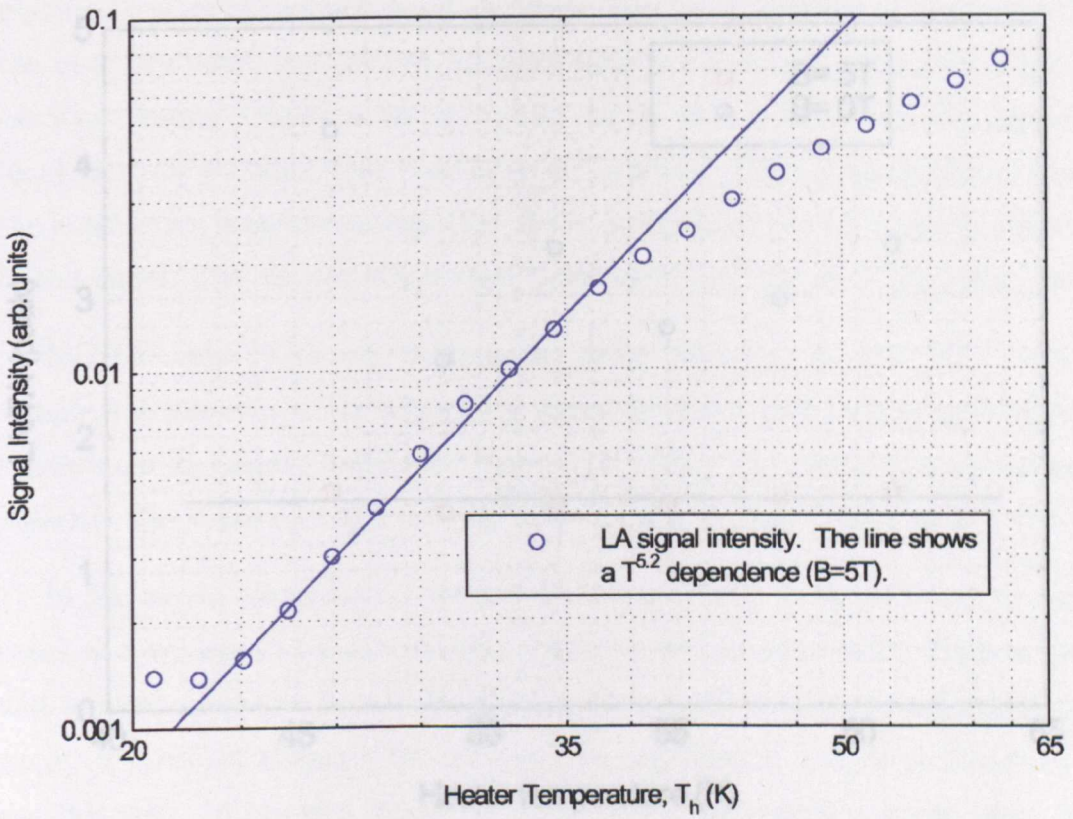

Figure 4.21: The dependence of signal intensity on heater temperature. The signal shows a $T^{5.2}$ dependence, and was recorded at a magnetic field of ~5T.

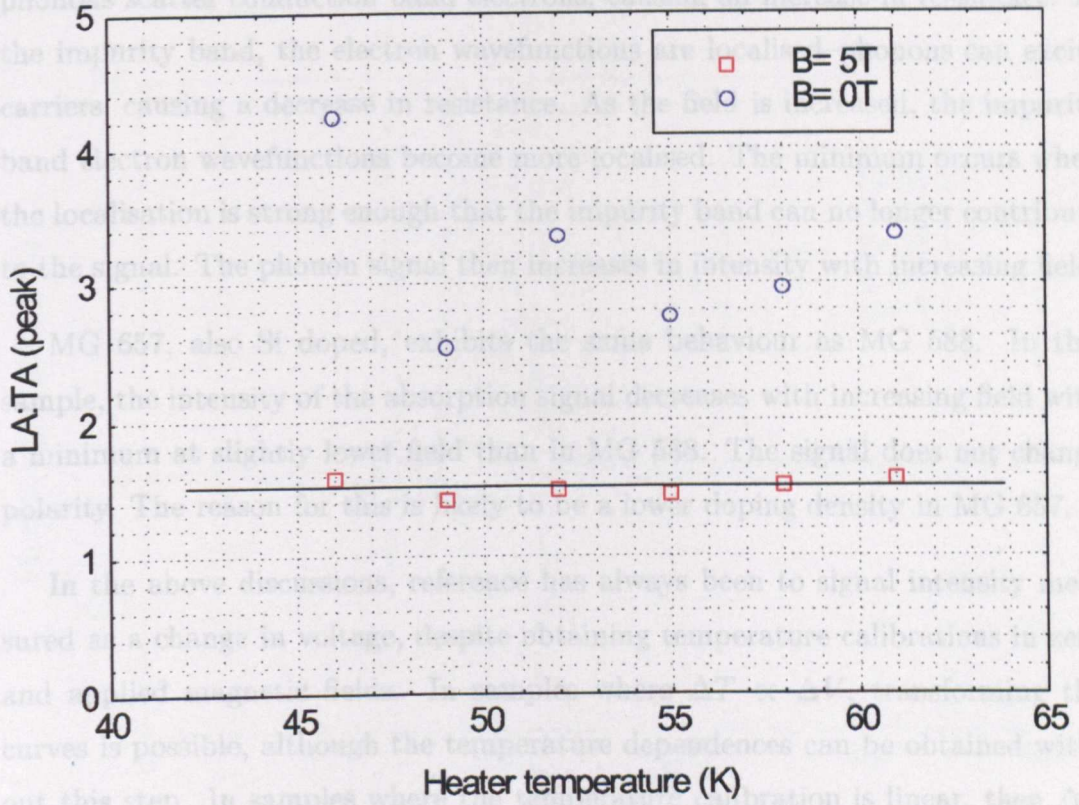

Figure 4.22: The ratio of signal intensity as the heater temperature is increased. At 5T, the ratio is constant and the intensity is twice that in zero field.

ing swept is shown in Figure 4.23. The signal initially decreases with increasing field, changes polarity, passes through a minimum at ~1.3T and then increases steadily with increasing field. The most plausible explanation for this behaviour is as follows. In this silicon doped sample, there are two competing contributions to the phonon induced signal – from the conduction band and from the impurity band, as previously discussed in Section 3.3.4. Without applied field, phonons scatter conduction band electrons, causing an increase in resistance. In the impurity band, the electron wavefunctions are localised–phonons can excite carriers, causing a decrease in resistance. As the field is increased, the impurity band electron wavefunctions become more localised. The minimum occurs when the localisation is strong enough that the impurity band can no longer contribute to the signal. The phonon signal then increases in intensity with increasing field.

MG 657, also Si doped, exhibits the same behaviour as MG 588. In this sample, the intensity of the absorption signal decreases with increasing field with a minimum at slightly lower field than in MG 588. The signal does not change polarity. The reason for this is likely to be a lower doping density in MG 657.

In the above discussions, reference has always been to signal intensity measured as a change in voltage, despite obtaining temperature calibrations in zero and applied magnetic fields. In samples where $\Delta T \propto \Delta V$, transforming the curves is possible, although the temperature dependences can be obtained without this step. In samples where the temperature calibration is linear, then ΔT is the temperature by which the system must be raised to cause the same effect as absorption. Using this analysis for MG 588, ΔT was approximately 1K at the highest heater temperatures. With such strong absorption, one needs to remember the initial comment that $\Delta T \ll T_{eq}$. In practice, it is advantageous to work at higher lattice temperatures, such that the inequality holds for higher powers. It must also be remembered that bias is applied to these samples – this heats the carriers. A problem is then encountered – are the electrons significantly warmed above the lattice temperature. This is probably the cause of the non–linearity which was observed in some samples. In this case, the use of ΔT is inappropriate.

In contrast to the doped samples, the undoped samples show the same depen-

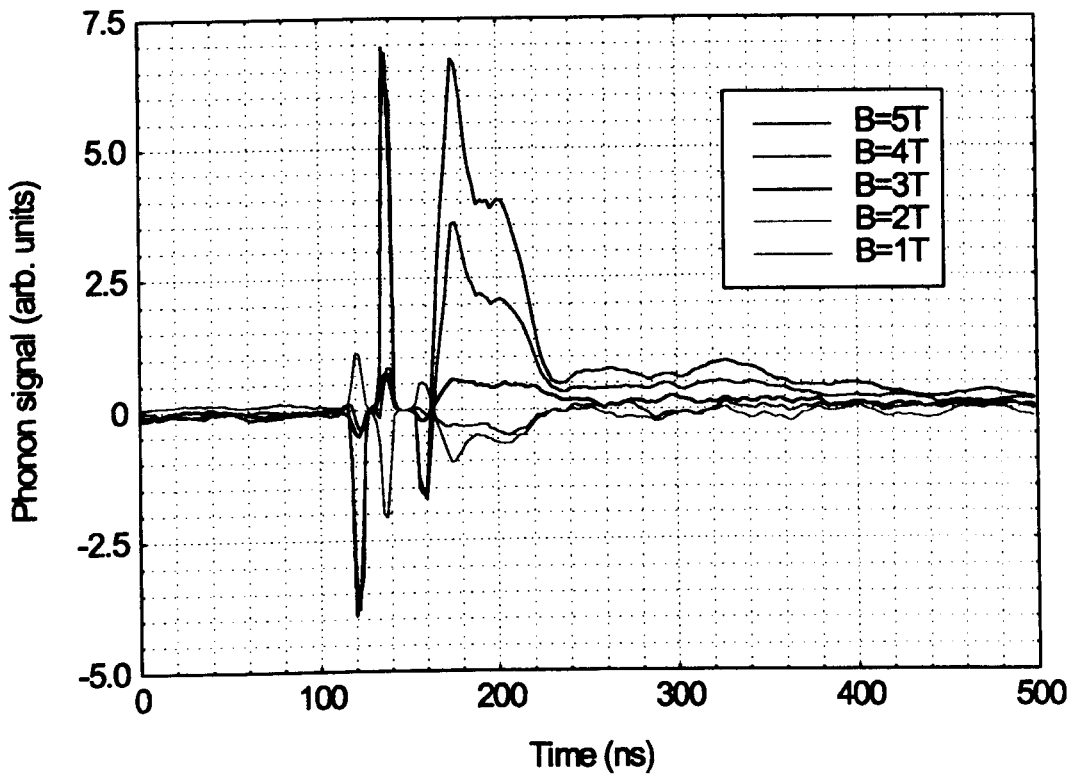

Figure 4.23: Heat pulse signals at different magnetic fields.

dence on heater temperature in zero and applied field. Illumination has no effect on intensity. The temperature dependence of all samples is shown in Figure 4.24 and Figure 4.25. The value of the α ranges from $\sim$ 4.1-5.9, and the power law falls away for heater temperatures $\geq$32K. This temperature is similar for both LA and TA modes, suggesting that relaxation of the cut–offs is occurring more strongly for TA phonons. The value of $\alpha \sim 5$ is indicative of piezoelectric coupling being dominant, in agreement with the results of emission experiments. However, there is no correlation between α and either carrier density or mobility. The reason for the different values is attributed to material characteristics which are not directly measured in these experiments. If non–equilibrium phonons are somehow trapped in the GaN layer, possibly as a result of defects, all the incident power would be absorbed by the GaN and blackbody behaviour would result, with a characteristic T^4 dependence. This may explain the dependence of MG 657, $\alpha \sim$ 4.1.

There is an apparent contradiction between these results and the results of emission experiments, where emission of LO–plasmon coupled modes was suggested as a probable cause of the deviation from the theory curves. In absorption, as previously discussed, the cut–off of the interaction is stronger since thermal broadening effects are not as important (the electrons are "cold"). The absorption results seem to indicate strongly that the $2k_F$ cut–off is relaxed. The effective value of k_F at high electron temperatures is given by

$$k_{eff} = k_F \left(1 + \frac{m^* k_B T_e}{\hbar^2 k_F^2}\right) \tag{4.4.2}$$

At an electron temperature of 50K, k_{eff} is only $\sim$ 4% larger than k_F for a carrier concentration of 5.7×10^{24} m^{-3}. Substituting the values of k_{eff} in place of k_F in $(2k_F)^{-1} \geq \ell$ has little effect on the condition for relaxation of the cut–off.

While the temperature dependences indicate that piezoelectric coupling dominates, the observed ratio of mode heights has not been discussed. In the absorption experiment, the electrons remain cold (in contrast to the situation in emission). In this regime, where the carriers are essentially localised in the impurity band, the conventional theories no longer apply. The use of the $2k_F$ cut–off

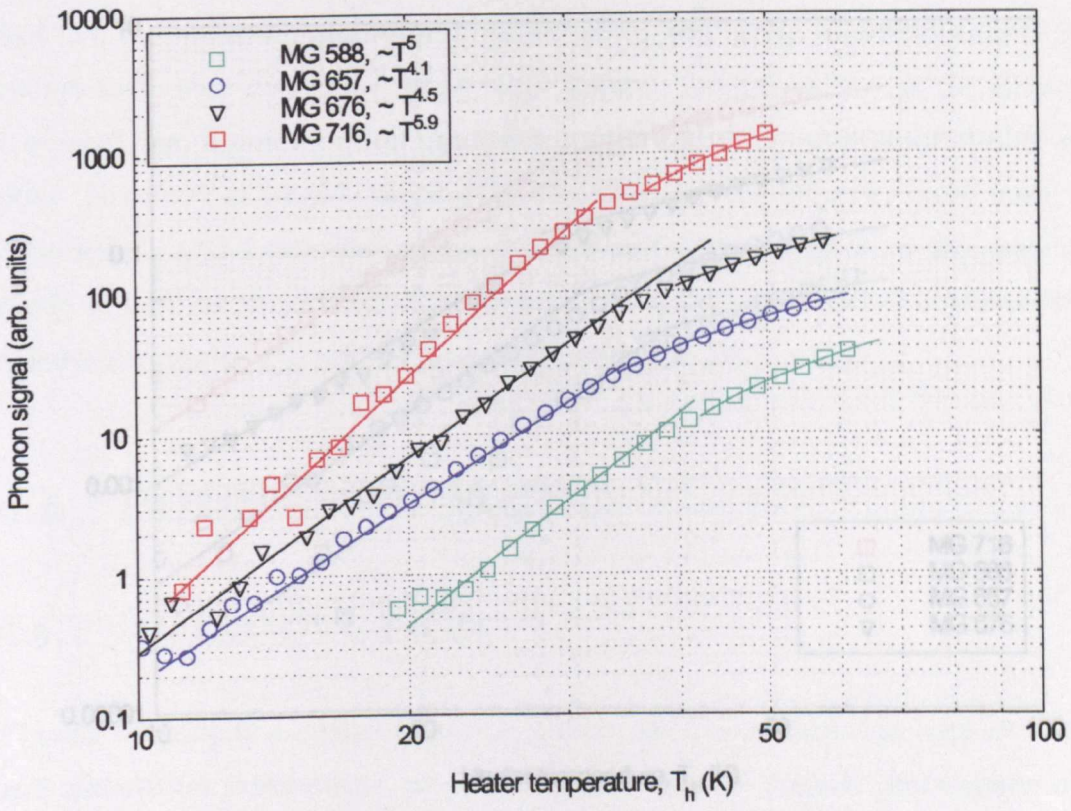

Figure 4.24: The dependence of LA phonon absorption on heater temperature for all samples studied.

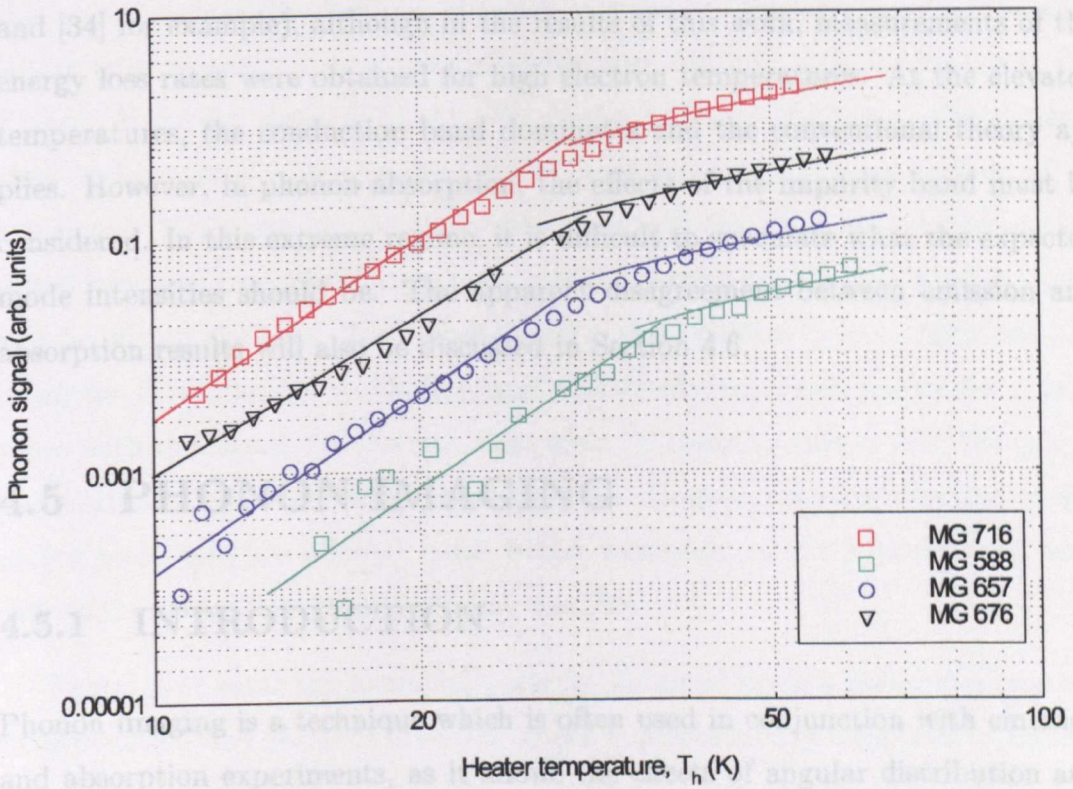

Figure 4.25: The dependence of TA phonon absorption on heater temperature for all samples studied.

is not appropriate. Indeed, the localisation will modify the electron–phonon coupling and also screening [30], [31]. To fully discuss the phonon absorption results presented here would require a more accurate theoretical model. The effects of the lack of an appropriate model can be seen through the spread of observed temperature dependences, centred around the T^5 dependence. No correlation between the dependences and material parameters was observed. The effects of impurities on phonon emission has been considered in other systems ([32], [33] and [34] for example), although in the results of this work, measurements of the energy loss rates were obtained for high electron temperatures. At the elevated temperatures, the conduction band dominates and the conventional theory applies. However, in phonon absorption, the effects of the impurity band must be considered. In this extreme regime, it is difficult to speculate what the expected mode intensities should be. The apparent disagreement between emission and absorption results will also be discussed in Section 4.6.

4.5 PHONON IMAGING

4.5.1 INTRODUCTION

Phonon imaging is a technique which is often used in conjunction with emission and absorption experiments, as it allows the effects of angular distribution and focussing to be studied. This Section presents the results of imaging experiments performed by a variety of methods on sapphire and on GaN on sapphire. Although sapphire received a great deal of attention in the early days of the field, reproduction of the work of Every, Koos and Wolfe [35] is useful as it allows us to demonstrate the usefulness of the technique in studying these thin layers, even when the measurement is severely complicated, as well as determining that the experiments are accurate. Comparison of the images with those of GaN allow discussion of the interactions in GaN. The images are presented in the next Section.

4.5.2 IMAGING THE INTERACTION IN GaN

Phonon imaging in sapphire has been previously studied using samples which were typically 2–3mm thick, allowing good resolution of the LA and TA modes [35]. In this work, the thicknesses of the samples are $< 400\mu$m. A typical signal is shown in Figure 4.26. The major problem in imaging experiments is where to position the gate. When the phonon source is at large angles to the bolometer, the arrival time of the ballistic phonons is shifted to longer times (as the path length is increased). Gating the signal becomes difficult, as is illustrated in the Figure. If the LA signal is gated over the leading edge until the ballistic peak, then at large angles, the peak is shifted and the gate does not include all of the signal. If a wider gate is used, then there will also be a contribution to the signal intensity from the TA phonons, while at larger angles, only the LA signal will be within the gate. In thicker samples, this problem is less important. To overcome this difficulty, a "sliding gate" was developed, which allows the gate to move with the signal. In practice, care must be taken to ensure that the gate is appropriately positioned throughout the scan. However, the introduction of this gating technique has allowed much better resolution of the contributions from individual modes than was previously possible.

Figure 4.27 show the focussing patterns obtained when a metal film was optically excited and phonons detected on the opposite face of a sapphire substrate using a superconducting aluminium bolometer. These images show similar features to those obtained in previous studies–the finer detail that has been observed previously arises due to better separation of the phonon modes due to the use of thicker samples. The main features of the images are as follows. The LA mode appears roughly triangular in shape. Originally, it was suspected that this was due to a contribution to the gated signal from TA phonons. However, if the Monte Carlo simulation results of Figures 2.2 and 2.3 are studied, the same features are observed. More detail is visible in the TA phonon image. A remarkable amount of detail can be seen in this image (given the sapphire substrate is so thin). The TA pattern is triangular and shows the same features as seen in Figure 2.3.

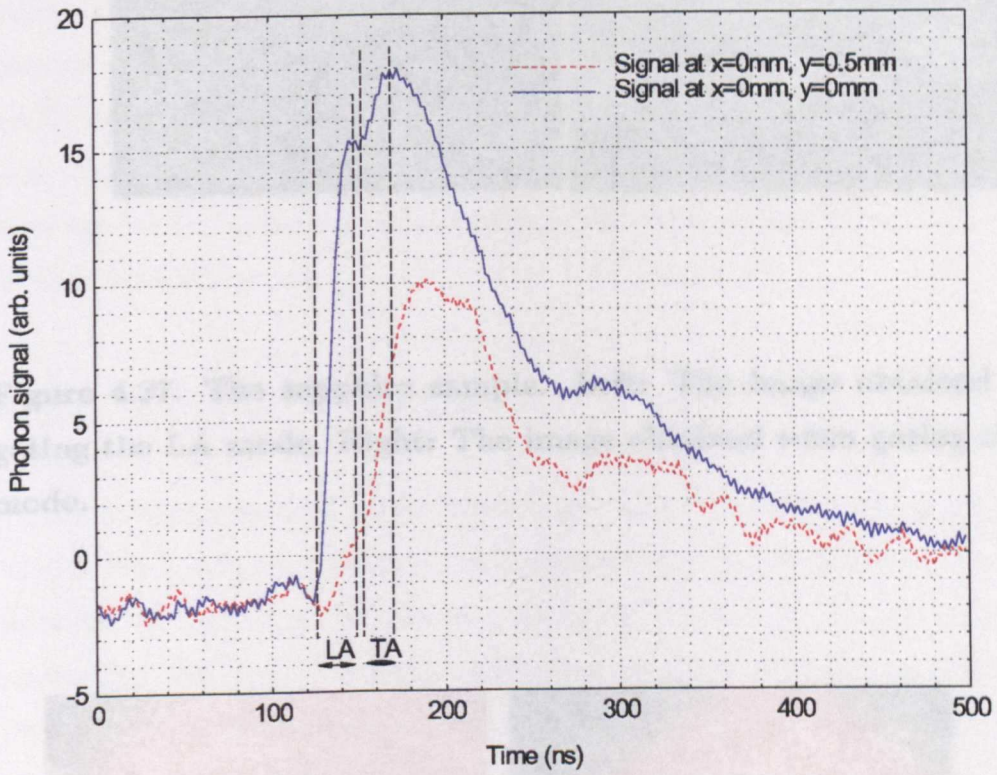

Figure 4.26: Signals obtained from MG 657 illustrating the problem of gating signals. The black vertical lines indicate the possible position of gates over the LA and TA ballistic peaks. At large angles, the gates are no longer appropriately positioned.

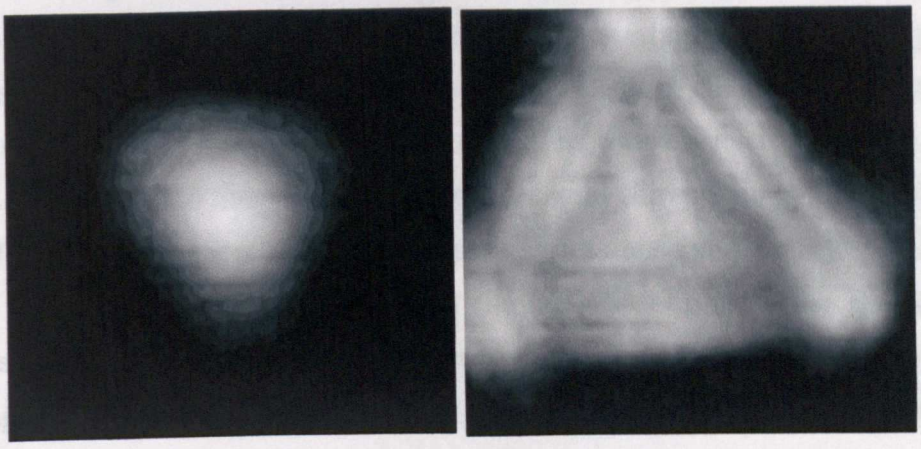

Figure 4.27: The sapphire sample. Left: The image obtained when gating the LA mode. Right: The image obtained when gating the TA mode.

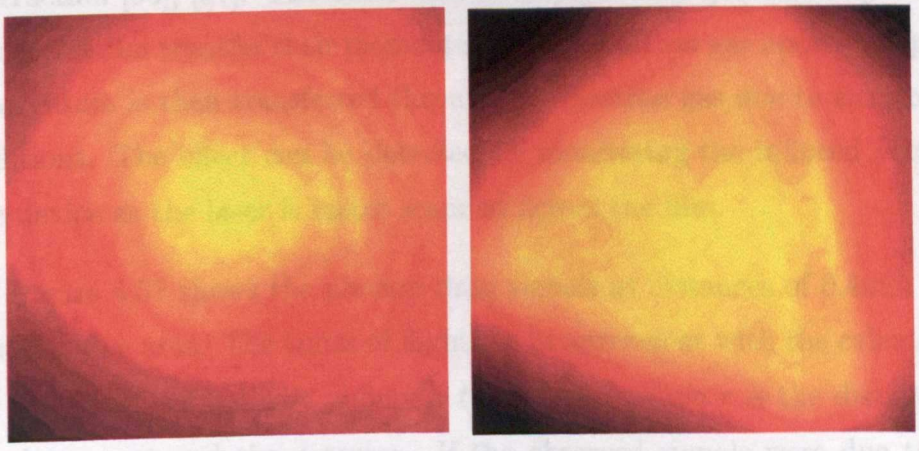

Figure 4.28: Images of MG 657. Left: The image obtained when gating the LA mode. Right: The image obtained when gating the TA mode.

Figures 4.28 and 4.29 show the phonon images obtained under the same conditions as in Figure 4.27. The LA image shows a large intensity when the laser is directly opposite the bolometer. The image shows a faint triangular shape, as did the sapphire image. The three features on the edges of the triangle are due to contributions to the signal from the TA mode. The concentric circles are an artefact of the sliding gate measurement. The TA signal shows triangular shape; the edges of the triangle show the same features as was observed with the sapphire sample. Slightly more detail is visible in the images obtained using the thicker (AXT) sample. Figure 4.30 shows the images obtained when the constantan film was evaporated onto the sapphire and the device used as the detector. The images are similar to those obtained using a bolometer, although there is less detail in the absorption images.

4.5.3 PHONON DRAG

Whilst imaging provides useful insight into phonon focussing effects and can be used to study phonon absorption and emission, imaging phonon drag can provide information regarding the effectiveness of the cut–offs of the electron–phonon interaction [36], [37]. The basic idea is that phonons generated by excitation of the metal film transfer their momentum to the electron gas upon absorption. This momentum is then transferred through the electron gas due to electron–electron collisions. The effect can be detected by monitoring the induced voltage across the device as the laser is raster scanned across the film.

Figure 4.31 shows the phonon drag signals at distances of 0.4mm either side of the active area. The times of flight are in agreement with the calculated values for the arrival of ballistic phonons, $t = r/v_{sTA}$, where r is the distance between the laser spot and the detector. If the observed signals were due to effects in the contacts, the signal arrival time would be shorter, $t = d/v_{sTA}$ where d is the thickness of the sapphire substrate.

Figure 4.32 shows the image of the induced voltage for MG 657. The orientation of the device is marked. The image displays a triangular shape, as was seen

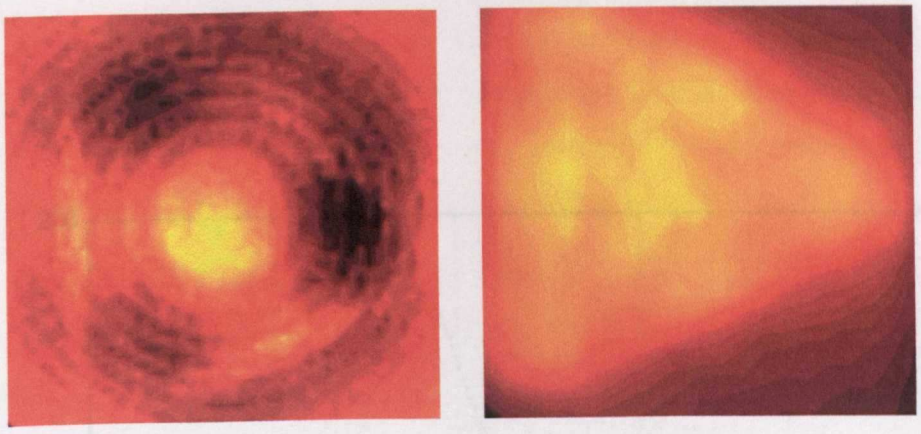

Figure 4.29: Images of the AXT layer. Left: The image obtained when gating the LA mode. Right: The image obtained when gating the TA mode.

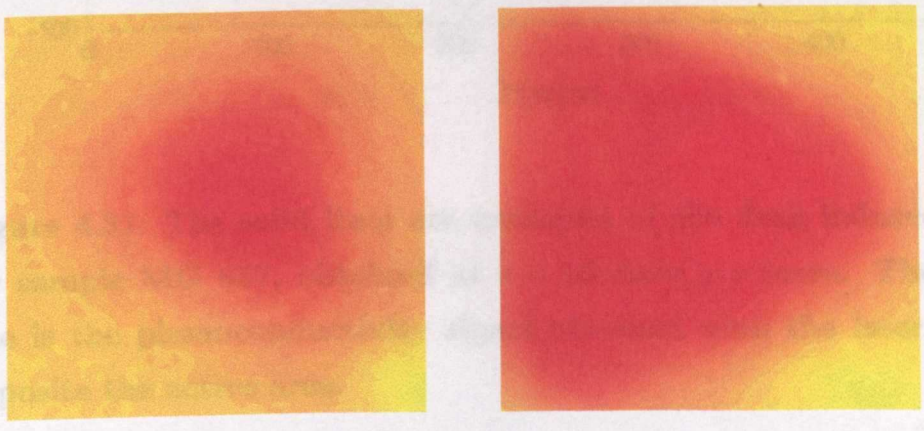

Figure 4.30: Images of MG 657. Left: The image obtained when gating the LA mode. Right: The image obtained when gating the TA mode.

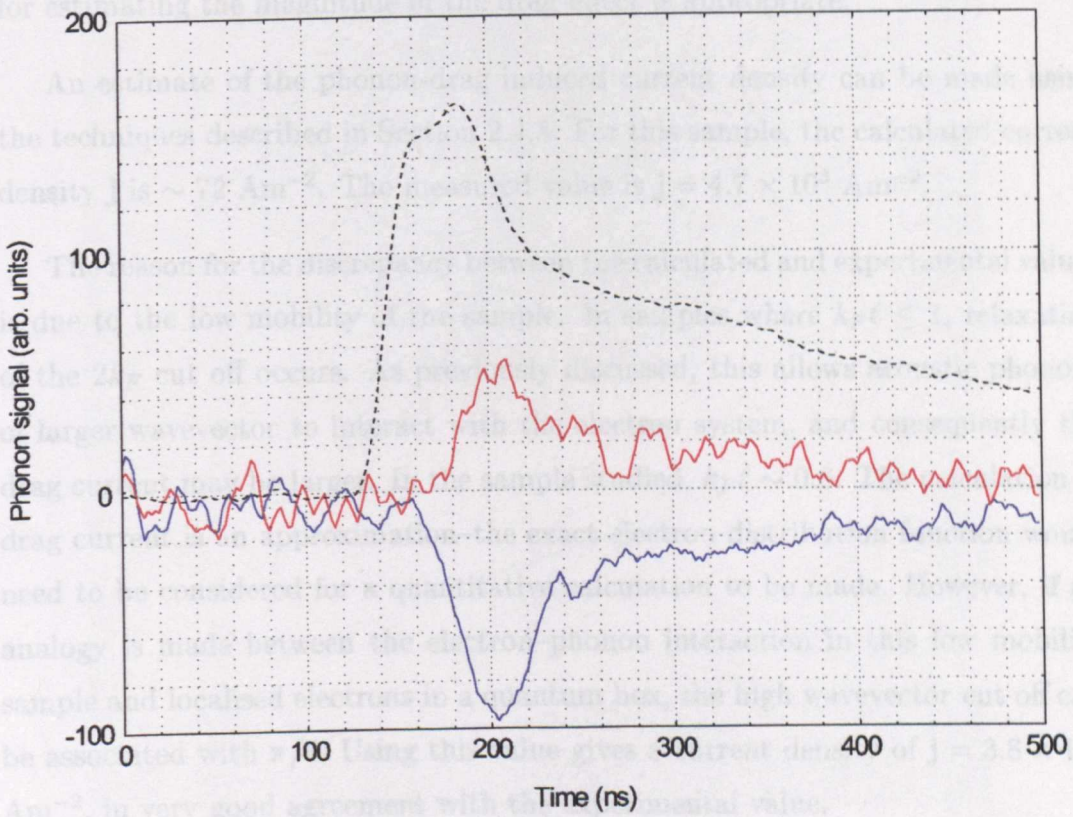

Figure 4.31: The solid lines are examples of the drag induced signals for sample MG 657, obtained at $x = \pm 0.4$mm, $y = 0$mm. The dashed line is the phonoconductivity signal obtained with the laser directly opposite the active area.

in phonoconductivity experiments when the signal was gated over the TA peak, suggesting the phonon drag effect is dominated by TA phonons.

In high mobility samples, the electron momentum is well defined and the condition $q\ell \gg 1$ is met. In the low mobility samples studied in this work, $q\ell < 1$ even for $q \sim 2k_F$ and the question arises as to whether the conventional approach for estimating the magnitude of the drag effect is appropriate.

An estimate of the phonon-drag induced current density can be made using the techniques described in Section 2.4.8. For this sample, the calculated current density $\mathbf{j}$ is ~ 72 Am^{-2}. The measured value is $\mathbf{j} = 4.7 \times 10^3$ Am^{-2}.

The reason for the discrepancy between the calculated and experimental values is due to the low mobility of the sample. In samples where $k_F\ell \leq 1$, relaxation of the $2k_F$ cut off occurs. As previously discussed, this allows acoustic phonons of larger wavevector to interact with the electron system, and consequently the drag current may be larger. In the sample studied, $k_F\ell \sim 0.6$. The calculation of drag current is an approximation–the exact electron distribution function would need to be considered for a quantitative calculation to be made. However, if an analogy is made between the electron–phonon interaction in this low mobility sample and localised electrons in a quantum box, the high wavevector cut off can be associated with π/ℓ. Using this value gives a current density of $\mathbf{j} = 3.8 \times 10^3$ Am^{-2}, in very good agreement with the experimental value.

4.6 SUMMARY OF RESULTS

Energy relaxation measurements were performed over the temperature range $\sim$ 20K–250K. For all samples studied, good agreement with the predicted energy loss rate was observed at the highest and lowest electron temperatures. The optic phonon energy, 90±4meV, and electron–optic phonon scattering time, 8 fs, were both in good agreement with the values obtained by other methods. In the intermediate range of temperatures, between $T_e \sim$ 40K–100K, the measured energy relaxation rate is higher (in some cases by an order of magnitude) than predicted

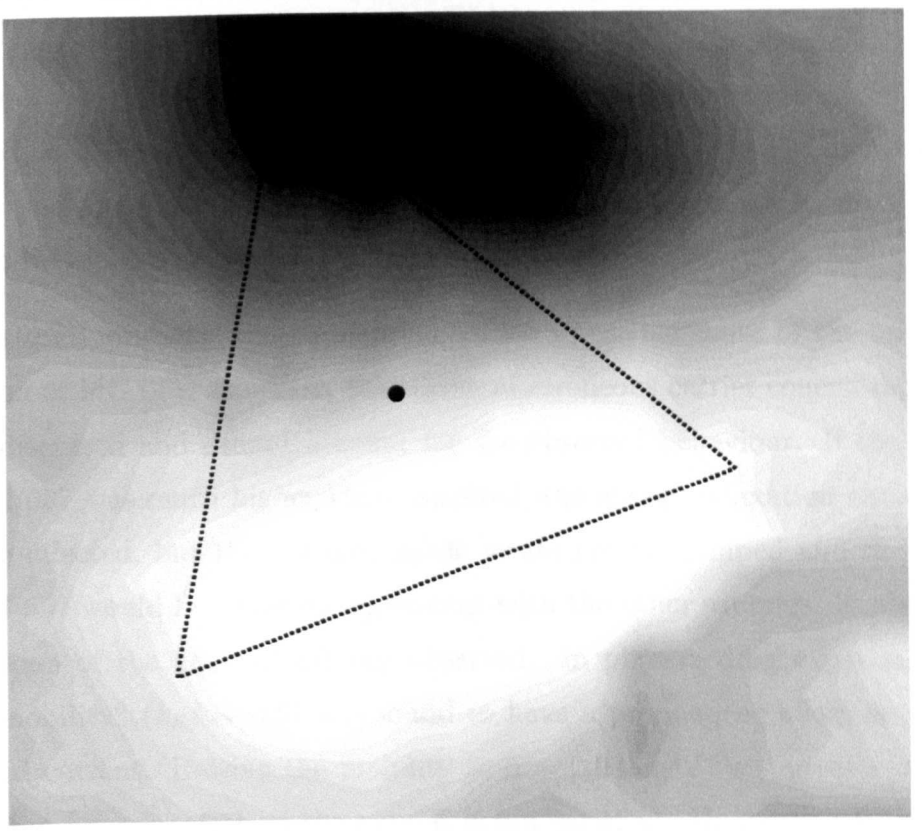

Figure 4.32: The phonon drag image for MG 657. The scan area is $1 \times 1\text{mm}^2$. The circle shows the position of the centre of the active area of the GaN device, while the dashed line shows the outline of the TA phonoconductivity image (shown in Figure 4.30).

by theory. The possible causes of the deviation were discussed. Relaxation of the $2k_F$ cut–off could not account for the observed behaviour. The deviation from predicted behaviour exhibited a density dependence, and so enhanced energy loss due to emission of plasmon–LO coupled modes seemed a reasonable cause. However, the position of MG 588 (where energy loss via coupled modes should have been suppressed) and MG 657 (the lowest density sample measured) in the plot of the deviation for all samples was not accounted for. The density dependence is followed by all samples except MG 657. This was the lowest density sample studied, and should show the smallest deviation from theory. The deviation from theory scaled by the carrier density ($\times 10^{24}\mathrm{m}^{-3}$) is the same, $\simeq$1, in all samples except MG 657.

Material inhomogeneity was proposed as a possible cause of the unexpected position of MG 657. However, the effects of erroneous carrier concentration have been discussed and cannot account for the observed behaviour. If the mobility of MG 657 was much higher than expected, the energy relaxation curves would not be affected, but the plasmon mode would not be damped and the position of MG 657 would be in better agreement with the other samples. In absorption, relaxation of the $2k_F$ cut–off was observed. In phonon drag experiments, the "low mobility" ($k_F\ell \sim 0.6$) was found to have a pronounced effect on the drag induced current. Raising the mobility to $\mu = 0.035\mathrm{m}^2\mathrm{V}^{-1}\mathrm{s}^{-1}$ gives $k_F\ell \sim$3–the condition for relaxation of the cut–off is not satisfied. However, relaxation and emission and absorption and drag experiments were performed on two different samples (due to destruction of the samples at the high electron temperatures). Material inhomogeneity across the wafer can therefore account for the observed behaviour.

Phonon emission experiments complemented the energy relaxation measurements. The crossover from acoustic to optic phonon emission, occurring at $T_e \sim$100K, was determined. TA phonon emission was found to dominate energy relaxation at low $T_e \leq$ 20K. At higher temperatures, the contribution from LA modes increased. In contrast to relaxation measurements, evidence of hot phonon effects was observed at the highest electron temperatures.

Phonon absorption experiments, performed using a fixed phonon source, showed the cut–off of the interaction occurring at much higher temperatures than expected. Absorption of phonons with a higher wavevector than expected suggested that the $2k_F$ cut–off was relaxed in all samples studied.

The apparent contradiction between absorption and energy relaxation measurements can be resolved by considering the nature of both the GaN system and the nature of the measurements. The electrons are believed to occupy two energy bands; the conduction band, where carriers are free and the impurity band, where carriers are essentially localised and conduction occurs via hopping. The effect of the two band model on Hall measurements was considered in [38]. At high temperatures, as in emission experiments, the conduction band dominates since carriers are thermally activated from the impurity band into the conduction band. In this case, the conventional theory is valid. In the emission measurements, there is no evidence of the $2k_F$ cut–off being relaxed. (It is assumed that electron–electron interactions between bands ensures thermal equilibrium). At low temperatures, as in absorption and drag experiments, carriers are localised in the impurity band. The impurity band dominates and the description of the system as a free electron gas is no longer valid. This can also be seen in the temperature calibration, where the resistance of many of the samples increased rapidly for $T \leq$20K. The use of the $2k_F$ cut–off is not appropriate and so the cut–off is better described by consideration of the mean free path (phonons with a wavevector $q \geq (\ell)^{-1}$ cannot be absorbed).

Phonon imaging techniques have allowed the study of the phonon drag effect in GaN. In the low mobility sample chosen, MG 657, the condition $k_F\ell \leq 1$ was satisfied. This allowed the electron–phonon interaction in the low mobility regime to be studied. It was found that the phonon drag induced current was due mainly to TA phonons, and that this current was much larger than predicted by conventional theory of electron–phonon interactions in "clean" systems.

REFERENCES

[1] B. K. Ridley. *Quantum Processes in Semiconductors (4th Edition), Clarendon Press, Oxford*, (1999).

[2] C. H. Yang, J. M. Calrson-Swindle, S. A. Lyon, and J. M. Worlock. *Phys. Rev. Lett*, **55**, 2359, (1985).

[3] M. A. Khan, J. N. Kuznia, A. R. Bhattari, and D. T. Olson. *Appl. Phys. Lett*, **62**, 12, (1993).

[4] Y. F. Yu, B. P. Keller, S. Keller, D. Kapolnek, P. Kodozoy, S. P. Denvaars, and U. K. Mishra. *Appl. Phys. Lett*, **69**, 1438, (1996).

[5] *Semiconductors: Basic data (edited by O. Madelung) Springer, Berlin*, (1996).

[6] *Gallium Nitride and Related Semiconductors (edited by J.H.Edgar, S.Strite, I.Akasaki, H.Amano and C.Wetzel, INSPEC, London*, (1999).

[7] X. Q. Zhou, W. W. Ruhle, P. Schullatz, P. Kovecar, H. M. van Driel, and K. Ploog. *Semi. Sci. Tech*, **9**, 704, (1994).

[8] W. Potz. *Phys. Rev. B*, **36**, 5016, (1987).

[9] E. Ozturk, A. Straw, N. Balkan, G. Jones, J. Frost, and D. Ritchie. *Semi. Sci. Tech*, **7**, 1417, (1992).

[10] S. Hess, R. A. Taylor, E. D. O'Sullivan, J. F. Ryan, N. J. Cain, V. Roberts, and J. S. Roberts. *phys. stat. sol (b)*, **216**, 51, (1999).

[11] H. Ye, G. W. Wick, and P. M. Fauchet. *Appl. Phys. Lett*, **74**, 711, (1999).

[12] K. T. Tsen, D. K. Ferry, A. Botchkarev, B. Sverdlov, A. Salvador, and H. Morkoc. *Appl. Phys. Lett*, **71**, 1852, (1997).

[13] H. Al Jawhari, A. G. Kozorezov, M. Sahraoui-Tahar, J. K. Wigmore, and C. D. W. Wilkinson. *Physica B*, **263-263**, 211, (1999).

[14] M. Giltrow, A. Kozorezov, M. Sahraoui-Tahar, J. K. Wigmore, J. H. Davies, C. R. Stanley, B. Vogel, and C. D. W. Wilkinson. *Phys. Rev. Lett*, **75**, 1827, (1995).

[15] A. G. Kozorezov, J. K. Wigmore, and M Giltrow. *J.Phys:Condens. Matter*, **9**, 4863, (1997).

[16] T. Kozawa, T. Kachi, H. Kano, Y. Taga, M. Hashimoto, N. Koide, and K. Manabe. *J. Appl. Phys*, **75**, 1098, (1993).

[17] F. Demangeot, J. Frandon, M. A. Renucci, N. Grandjean, B. Beaumont, J. Massies, and P. Gibart. *Solid State Commun.*, **106**, 491, (1998).

[18] S. Das Sarma, J. K. Jain, and R. Jalabert. *Phys. Rev. B*, **37**, 6290, (1988).

[19] S. Das Sarma, J. K. Jain, and R. Jalabert. *Phys. Rev. B*, **37**, 4560, (1988).

[20] P. Perlin, J. Camassel, W. Knap, T. Taliercio, J. C. Chervin, T. Suski, I. Grzegory, and S. Porovski. *Appl. Phys. Lett*, **67**, 2524, (1995).

[21] J. K. Wigmore, M. Erol, M. Sahraouitahar, M. Ari, C. D. W. Wilkinson, J. H. Davies, M. Holland, and C. Stanley. *Semi. Sci. Tech*, **8**, 322, (1993).

[22] A. J. Kent, A. Cross, P. Hawker, and M. Henini. *phys. stat. sol (b)*, **204**, 230, (1997).

[23] I. A. Pentland. *PhD thesis, University of Nottingham*, (2000).

[24] P. Hawker, A. J. Kent, T. S. Cheng, and C. T. Foxon. *Physica B*, **263-264**, 227, (1999).

[25] K. R. Strickland, R. E. George, M. Henini, and A. J. Kent. *Semi. Sci. Tech*, **9**, 786, (1994).

[26] R. G. Ulbrich. *Journal de Physique*, **C7**, 423, (1981).

[27] V. Narayanamurti. *Journal de Physique*, **C6**, 221, (1981).

[28] A. J. Kent, R. E. Strickland, K. R. Strickland, A. J. Cross, P. Hawker, and M. Henini. *Semi. Sci. Tech*, **12**, 849, (1997).

[29] P. Hawker, A. J. Kent, N. Hauser, and C. Jagadish. *Semi. Sci. Tech*, **10**, 601, (1995).

[30] B. L. Altshuler and A. G. Aronov. *in Electron-Electron Interactions in Disordered Systems, edited by A. L. Efros and M. Polak, North-Holland, Amsterdam*, (1985).

[31] E. Chow, H. P. Wei, S. M. Girvin, and M. Shayegan. *Phys. Rev. Lett*, **77**, 1143, (1996).

[32] D. V. Kveshchenko and M. Reiser. *Phys. Rev. B*, **56**, 15822, (1999).

[33] R. Fletcher, Y. Feng, C. T. Foxon, and J. J. Harris. *Phys. Rev. B*, **61**, 2028, (2000).

[34] E. Chow, H. P. Wei, S. M. Girvin, W. Jan, and J. E. Cunningham. *Phys. Rev. B*, **56**, (1997).

[35] A. G. Every, G. L. Koos, and J. P. Wolfe. *Phys. Rev. B*, **29**, 2190, (1984).

[36] C. Jasiukiewicz, D. Lehmann, and T. Paszkiewicz. *Z. Phys. B*, **86**, 225, (1992).

[37] W. M. Gancza, C. Jasiukiewicz, A. J. Kent, D. Lehmann, T. Paszkiewicz, K. R. Strickland, and R. E. Strickland. *Semi. Sci. Tech*, **11**, 1030, (1996).

[38] J. J. Harris, K. J. Lee, I. Harrison, L. B. Flannery, D. Korakakis, T. S. Cheng, C. T. Foxon, Z. Bougrioua, I. Moerman, W. Van der Stricht, E. J. Thrush, B. Hamilton, and K. Ferhah. *phys. stat. sol (a)*, **176**, 363, (1999).

Chapter 5

AlGaN/GaN HETEROSTRUCTURES

5.1 INTRODUCTION

This Chapter presents the results of experiments performed on AlGaN/GaN heterostructures. This system has been successfully exploited in the production of high power devices, although increased material quality should lead to improved device characteristics. All epilayers were grown on sapphire substrates by MOCVD. Characterisation of the samples will be discussed, along with some of the differences between 2DEG samples and bulk layers. A discussion of energy relaxation will be presented, including details of the temperature calibration. A preliminary study of phonon absorption by an AlGaN/GaN 2DEG is also included.

A multitude of studies have been performed on this system (see, for example, [1], [2] and [3] concerning transport properties of layers grown on SiC and sapphire, [4] – [6] for theoretical descriptions of the system and [7] – [10] for a discussion of the effect of polarity on 2DEG formation and quality). The energy relaxation results presented here are the first measurements of this kind on this system, and as will be seen complement other studies well. Phonon absorption

measurements are also the first of their type, and could provide useful information about the confinement of electrons in AlGaN/GaN 2DEG's.

5.2 LAYER CHARACTERISATION

5.2.1 INTRODUCTION

This Section describes the measurements made in order to characterise the samples. Because the AlGaN/GaN samples could not be etched using UV assisted wet etching techniques, devices must be either be etched by dry methods or the sample geometry must preclude etching. In practice, both etched devices and a variety of samples which were not etched were used. Although there are contact recipes for contacting to 2DEG's (for example [11], [12] and [13]), every evaporation and annealing system is different–contacting proved not to be a straightforward step. The characterisation of samples whose mobility and carrier density were provided by the growers allowed the quality of the contacts to be ascertained. Vast deviations in the measured carrier density and mobility suggested bad contacts, and allowed the contacting process to be developed. With the carrier density accurately determined, energy relaxation measurements could be performed.

5.2.2 MAGNETIC FIELD MEASUREMENTS

With the sample cooled to 1.6K, the device resistance is measured as a function of magnetic field. The observation of large magnetoresistance oscillations, called Shubnikov–de Haas oscillations, is indicative of a 2DEG. The resistance oscillates as a consequence of Landau levels passing through the Fermi level as the field increases. As the field is increased, the density of states of the Landau levels increases, and so the occupation of the levels changes since the Landau levels can accommodate more electrons.

Figure 5.1 shows the device resistance as a function of field. These oscillations are periodic in $1/B$, and by plotting the Landau level index against $1/B$, the carrier density can be extracted using

$$i = \frac{hn_s}{2e}\Delta\left(\frac{1}{B}\right) \tag{5.2.1}$$

where i is the Landau level index and all other symbols have their usual meanings.

In this sample, oscillations are visible from ~1.5T. The device was a Hall bar, with $R_\square$ ~180 Ω. The calculated sheet carrier density was found to be $n_s = 5.61 \times 10^{16}$ m^{-3}, giving a mobility of ~ 6000 cm^{2}V^{-1}s^{-1}. Recent advances in growth strategies have improved mobilities considerably. However, this sample was amongst the highest mobilities when grown ([14] and [15] report the properties of 2DEG's grown by the same group who provided J401).

The sample exhibits a slight negative magnetoresistance at low fields, and the minima in the oscillations decrease with increasing field. There is no evidence of parallel conduction in this sample, characterised by the oscillation riding on a background of positive magnetoresistance [16], [17].

Figure 5.2 shows the normalised Shubnikov–de Haas (SdH) oscillations for all the 2DEG samples studied. Both J401 and G 0–99 show similar behaviour, with apparently no parallel conduction. The oscillations in the other three samples are of much lower amplitude and start at much higher field. These samples all show a rise in the minima as the field is increased, with sample D982–AN26 showing strong positive magnetoresistance. Prior to illumination, there was no evidence of oscillatory behaviour in these samples. The plots shown in the Figure show the weak oscillations which were observed after illumination. The behaviour of the samples under illumination will be discussed in the following Section. Increasing the carrier density in AlGaAs/GaAs 2DEG's by illumination with a red LED is common practice. In samples where oscillations were visible without illumination, the effect of light was to increase the amplitude but not affect the period, suggesting that the sheet carrier density was not increased in these samples.

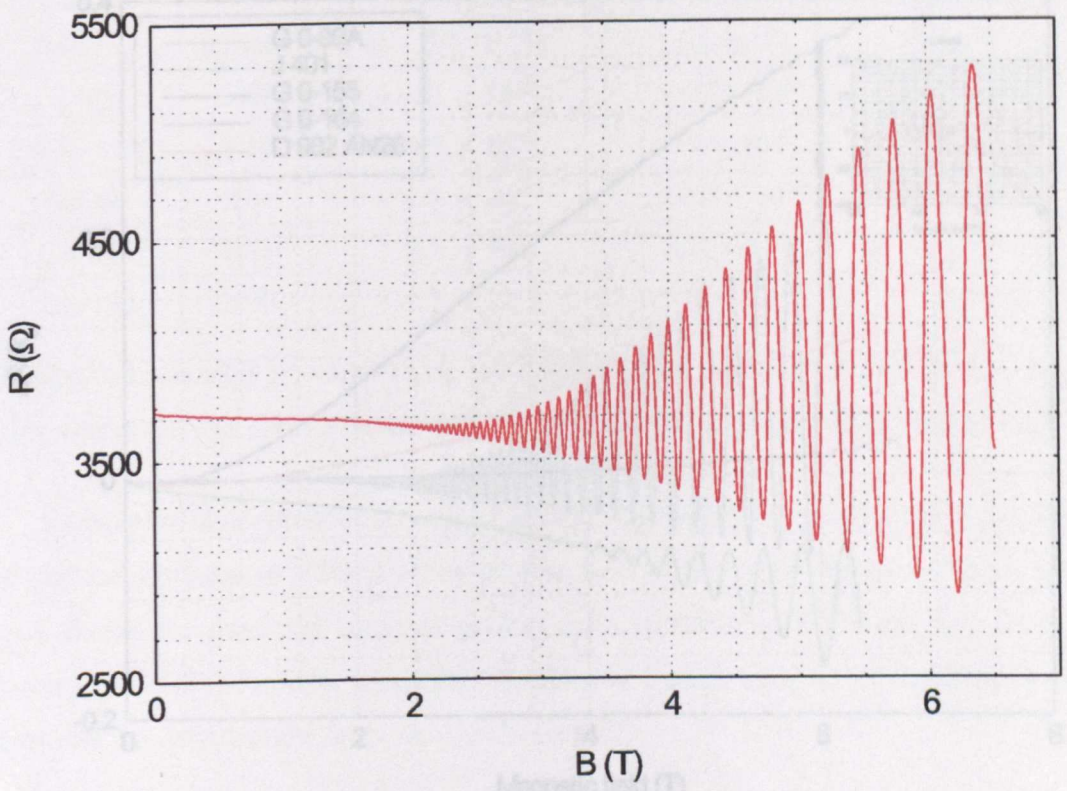

Figure 5.1: Device resistance as a function of magnetic field for sample J401.

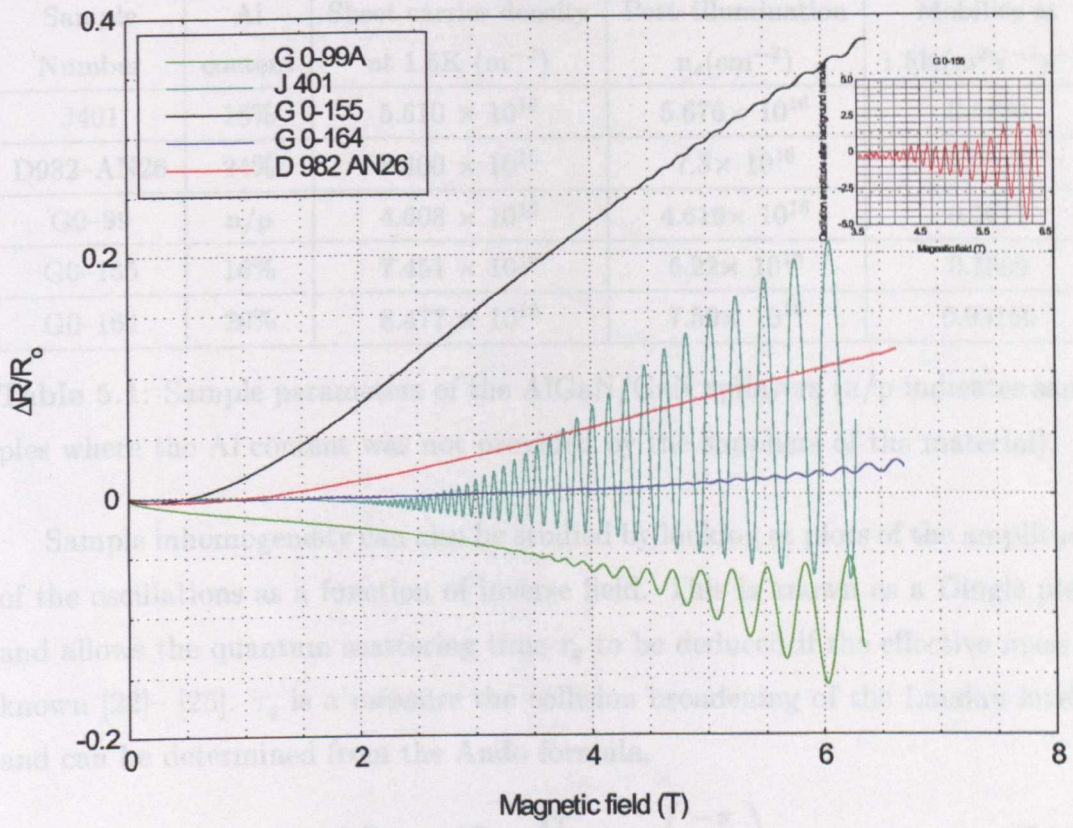

Figure 5.2: Device resistance as a function of magnetic field. The inset Figure shows oscillations from G 0-155 with the background removed.

There is no evidence of occupation of the second subband, nor any inhomogeneity in the sheet carrier density. When the second subband is occupied, the different carrier densities in each subband cause beating [18], [19], [20]. If there is inhomogeneity, with regions a varying carrier density, there would be a spread of frequencies that interfere with one another [21]. The material parameters are given in Table 5.1.

Sample Number	Al content	Sheet carrier density at 1.5K (m^{-2})	Post-illumination $n_s(cm^{-2})$	Mobility at 1.5K($m^2V^{-1}s^{-1}$)
J401	18%	5.610×10^{16}	5.676×10^{16}	0.5400
D982-AN26	24%	9.400×10^{16}	7.8×10^{16}	0.0557
G0-99	n/p	4.608×10^{16}	4.619×10^{16}	0.2019
G0-155	16%	7.451×10^{16}	6.22×10^{16}	0.1889
G0-164	20%	8.477×10^{16}	7.50×10^{16}	0.03166

Table 5.1: Sample parameters of the AlGaN/GaN epilayers (n/p indicates samples where the Al content was not provided by the suppliers of the material).

Sample inhomogeneity can also be studied by looking at plots of the amplitude of the oscillations as a function of inverse field. This is known as a Dingle plot, and allows the quantum scattering time τ_q to be deduced if the effective mass is known [22]- [25]. τ_q is a measure the collision broadening of the Landau levels, and can be determined from the Ando formula,

$$\Delta R_{xx} = 4R_o \frac{\chi_T}{\sinh \chi_T} exp\left(\frac{-\pi}{\omega_c \tau_q}\right) \tag{5.2.2}$$

where

$$\chi_T = \frac{2\pi^2 k_B T}{\hbar \omega_c} \tag{5.2.3}$$

and ω_c is the cyclotron frequency, given by eB/m^*.

The values of τ_q which were obtained from Figure 5.3 are comparable to those in [22]. This shows the improvement in material grown on sapphire in recent years; the lack of SdH oscillations in 2DEG's on sapphire was attributed to vastly

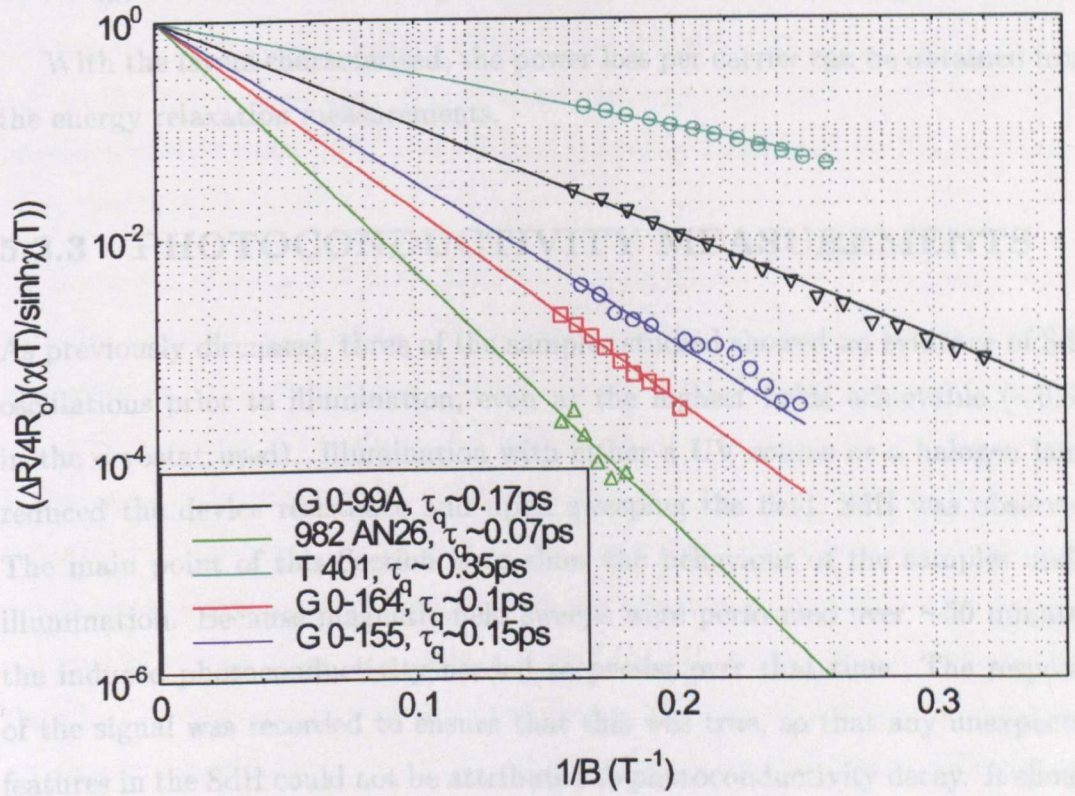

Figure 5.3: Oscillation amplitude as a function of inverse magnetic field.

different scattering times than 2DEG's on SiC (the carrier density and mobility of the samples was similar).

Comparing τ_q with τ_c, the classical scattering time, given by $\tau_c = \mu m^*/e$ can be used to infer the "quality" of the interface. Large values of τ_c/τ_q have been attributed to defect scattering at the interface [22]. In the samples studied here, the ratio never exceeds ~2.1, indicating that large angle scattering is dominant. This suggests that interface roughness scattering could be limiting the mobility.

With the layers characterised, the power loss per carrier can be obtained from the energy relaxation measurements.

5.2.3 PHOTOCONDUCTIVITY MEASUREMENTS

As previously discussed, three of the samples studied showed no evidence of SdH oscillations prior to illumination, even at the highest fields achievable (~6.5T in the cryostat used). Illumination with either a UV source or a halogen lamp reduced the device resistance and upon sweeping the field, SdH was observed. The main point of this Section is to show the behaviour of the samples under illumination. Because magnetic field sweeps were performed over ~50 minutes, the induced photoconductivity needed to persist over that time. The response of the signal was recorded to ensure that this was true, so that any unexpected features in the SdH could not be attributed to photoconductivity decay. It should be noted that these measurements were rather basic, although they do reveal some features of the persistent photoconductivity effect (PPC) in AlGaN/GaN 2DEG's. More detailed studies of PPC effects and the effects of illumination on device performance can be found in [26], [27], [28].

A typical plot is shown in Figure 5.4. The samples (at 1.6K) were illuminated with a UV lamp through the quartz windows of the cryostat. The illumination was continued until no appreciable change is device resistance occurred. As can be seen, the initial response of the device is a decrease in resistance of ~25% of the base temperature value. This reduction is quite small compared to the

behaviour of AlGaAs/GaAs structures, but was essential to observe SdH in the AlGaN/GaN samples.

Detailed studies of PPC effects in these systems can be found in the literature, [29], [30], [31]. In such studies, the main aim was to determine the origin of the mechanism. There are reports of PPC in bulk GaN, although when the GaN samples studied in this work were illuminated with the same halogen lamp as the 2DEG's, there was no appreciable change in resistance, and the device resistance quickly returned to the "dark" value. This immediately suggests the effect is due to the presence of the AlGaN, either through impurities in the layer or an interface phenomenon [32]. The effect is generally attributed to photoionisation of donors in AlGaN [33].

In the samples studied, there is no correlation between the % resistance change and any material parameters. The halogen lamp and UV lamp caused different behaviour in different samples. The time taken to reach the lowest resistance varied in each sample. The effects of illumination were persistent over long periods. If the sample was warmed to ~60K and cooled again, the device resistance was below the initial "dark" resistance value. When the sample was illuminated, the dependence of resistance on temperature did not change–the effect was merely to reduce the overall resistance. Measurement of SdH showed that in two samples, the effect of illumination was to increase the amplitude of oscillations but caused no appreciable change in n_s, while in the samples which required illuminating for SdH to be observable, the sheet carrier density which was obtained from the SdH was greater than values which has been provided by the Hall measurements performed by the growers.

The conclusion is that the reason for the PPC in the samples studied is not clear–a more detailed study is required to fully explain the behaviour. It was possible that the illumination is activating the contacts–illumination from both the AlGaN side and sapphire side was performed, and in both cases the device resistance was seen to drop, suggesting that contact effects were not responsible. However, the important point is that the sheet carrier density could be measured for all samples and that the PPC was persistent over the timescales necessary to

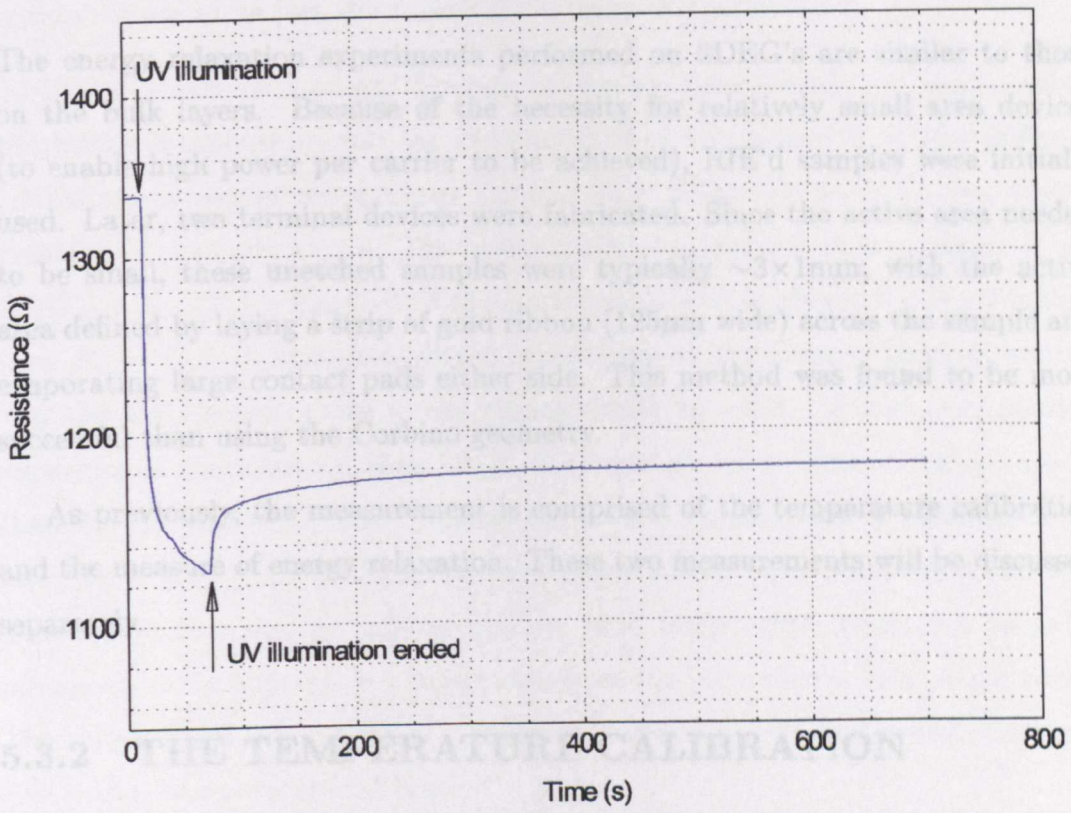

Figure 5.4: The device resistance as a function of time when the sample was illuminated. The start and end of the illumination are marked.

obtain accurate measurements of sample behaviour in magnetic field.

5.3 ENERGY RELAXATION IN 2DEG's

5.3.1 INTRODUCTION

The energy relaxation experiments performed on 2DEG's are similar to those on the bulk layers. Because of the necessity for relatively small area devices (to enable high power per carrier to be achieved), RIE'd samples were initially used. Later, two terminal devices were fabricated. Since the active area needed to be small, these unetched samples were typically ~3×1mm, with the active area defined by laying a strip of gold ribbon (125μm wide) across the sample and evaporating large contact pads either side. This method was found to be more successful than using the Corbino geometry.

As previously, the measurement is comprised of the temperature calibration and the measure of energy relaxation. These two measurements will be discussed separately.

5.3.2 THE TEMPERATURE CALIBRATION

In samples where impurity and defect scattering dominate over the contribution from phonon scattering, direct comparison between the measured two terminal device resistance and pulse measurements yield the power dissipation as a function of electron temperature. In AlGaAs/GaAs 2DEG's, this approach was found to be inaccurate and a method to separate the contributions was devised [34]. This method was originally employed in the temperature calibration of AlGaN/GaN heterostructures.

The contributions to the device resistance can be split into the contribution from impurities, R_{ex}, and the contribution from phonons, R_{em} and R_{abs} for emission and absorption respectively. If a small current is passed through the

device, the electrons are not heated above the ambient lattice temperature and so $T_e = T_\ell$. The measured resistance in this regime is R. In this situation the net rate of emission of phonons is zero; the emission rate from the carriers equals that for absorption and so $R_{em} = R_{abs}$. The device resistance can then be expressed as $R_D(T_\ell) = R_{ex}(T_\ell) + 2R_{abs}(T_\ell)$. Assuming that phonon scattering is negligible at very low temperatures, i.e. base temperature T_o, then the measured device resistance would be just the contribution from impurities.

If higher current is passed through the device, the electrons are heated above the lattice temperature and the resistances that are measured at two different lattice temperatures are denoted R_a and R_b. When $T_e > T_\ell, T_o$, stimulated emission of phonons occurs. The resistance of the device is then given by $R_D = R_{ex}(T_e) + R_{em}(T_e) + R_{abs}(T_\ell)$. If the contribution due to phonons was negligible, then $R_b \sim R_a$. In this case, direct comparison of the temperature calibration and the hot electron pulse measurement would be valid. If, however, phonon scattering is contributing, then for R_a measured at lower lattice temperature T_o than $R_b(T_\ell)$, $R_b > R_a$. Since R_{abs} at the lowest temperatures is assumed to be zero, $R_b - R_a = \Delta R \simeq R_{abs}(T_\ell)$. The contribution from phonons is ΔR and is therefore obtained by subtracting the base temperature resistance value as measured in the high current calibration from the high current calibration curve. The contribution from phonons is then subtracted from the low power curve and this is the "temperature calibration".

5.3.3 ENERGY RELAXATION CURVES

With the device resistance as a function of electron temperature obtained, the second stage of the measurement was performed. In the Hall bar samples, a four terminal measurement was made. A constant current source varied the current through the device and the voltage across two of the side contacts was recorded. The resulting "I–V" curve was transformed into device resistance against input power, and direct comparison with the temperature calibration allowed the power dissipated as a function of electron temperature to be obtained (a typical curve

is shown in Figure 5.5). With the two terminal devices, the pulse measurement was performed, as in the bulk layers (see Section 3.3.4).

Figure 5.6 shows the energy relaxation curves for sample J401. The experimental results show good agreement with the theoretical curve (including screening), calculated by numerical evaluation of Equation 2.4.28. Previous measurements on the same sample [35] have found a temperature dependence of $P_e \sim T^{4.4}$ for electron temperatures < 5K, and also show good agreement between the experimental data and the predicted energy loss rate. In the measurements performed in this work, for electron temperatures < 10K a $T^{\sim 4}$ dependence is observed, with $P_e \propto T_e$ at higher temperatures. As in the relaxation measurements of bulk GaN layers, as the electron temperature is increased, the dependence varies from the strong power law to linear, corresponding to the transition from the Bloch–Grüneisen into the equipartition regime. The Bloch–Grüneisen regime is characterised by $T_e \ll 2\hbar k_F v_s/k_B$; in this sample, to observe the strong power law dependence requires $T_e \ll 20$K, a condition which does not apply for the majority of the data.

In 2D systems, coupling via the unscreened piezoelectric interaction results in $P_e \propto T_e^3$; screening increases the exponent and $P_e \propto T_e^5$. Given the good agreement between experiment and theory, and the relatively "high" electron temperatures, it is concluded that the dominant energy relaxation mechanism in the sample is via emission of screened PZ modes.

Figures 5.7 and 5.8 show the results of measurements performed on D982–AN26 and G0–99. Again, good agreement with theory is seen. The observed temperature dependence is again indicative of screened piezoelectric coupling.

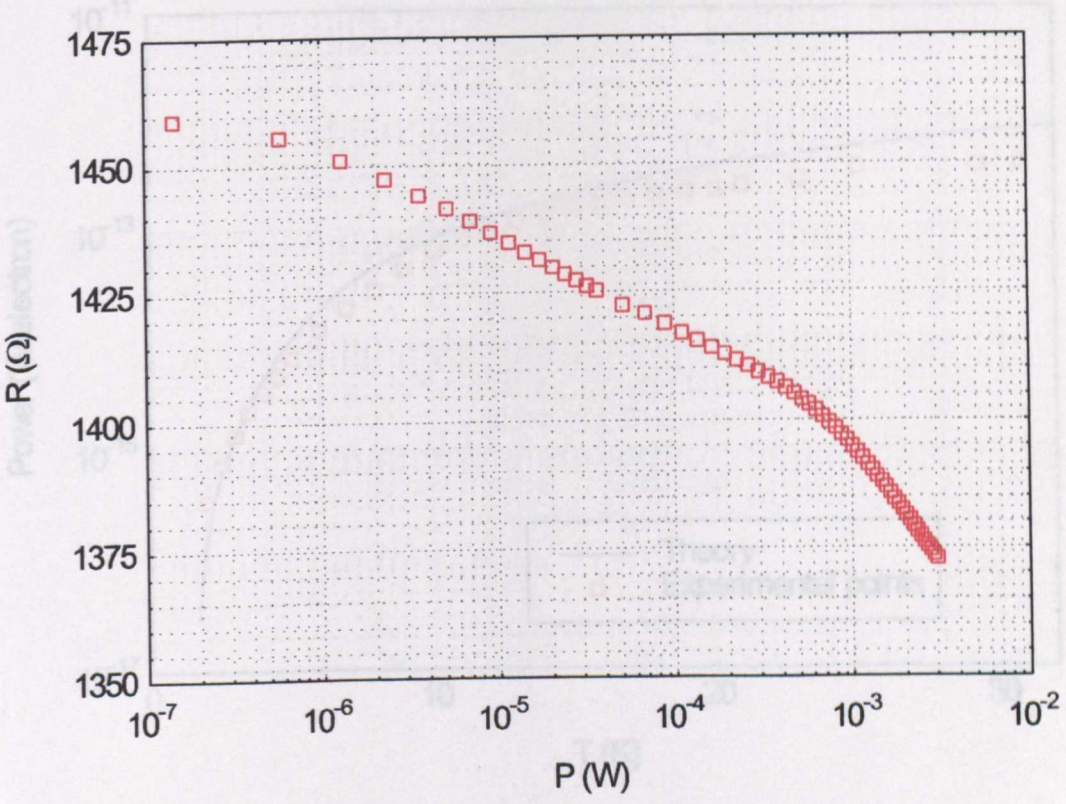

Figure 5.5: A plot of resistance against power for J401.

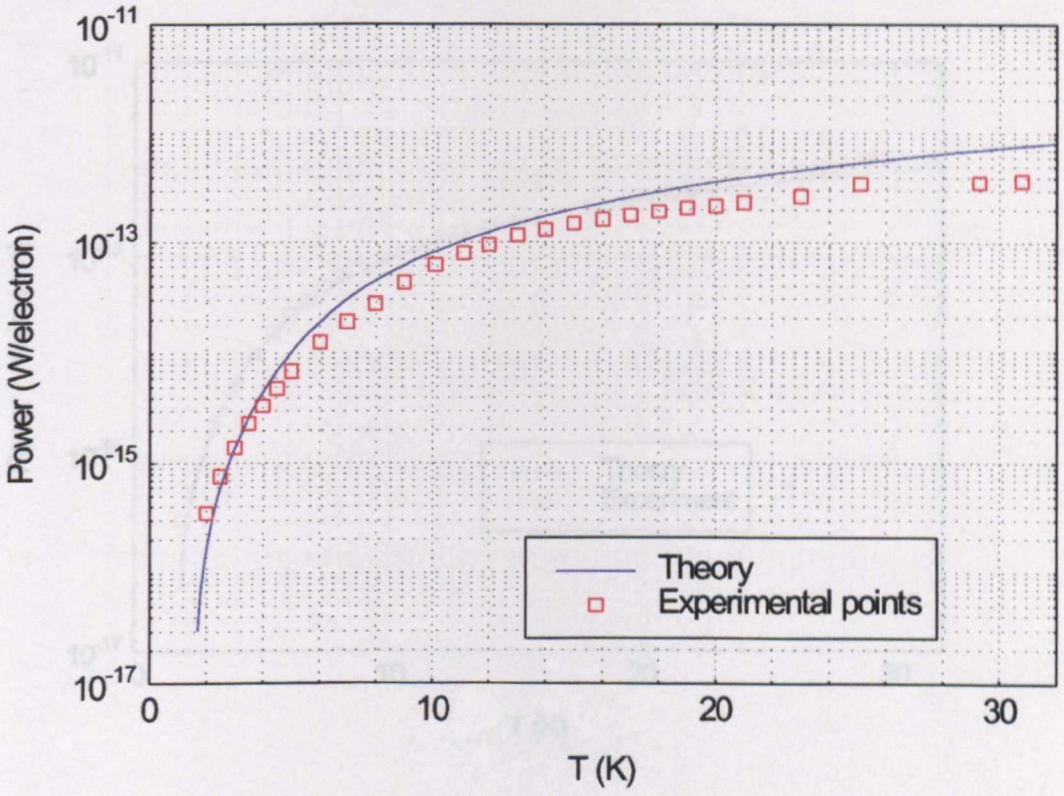

Figure 5.6: The power dissipated as a function of electron temperature for sample J401.

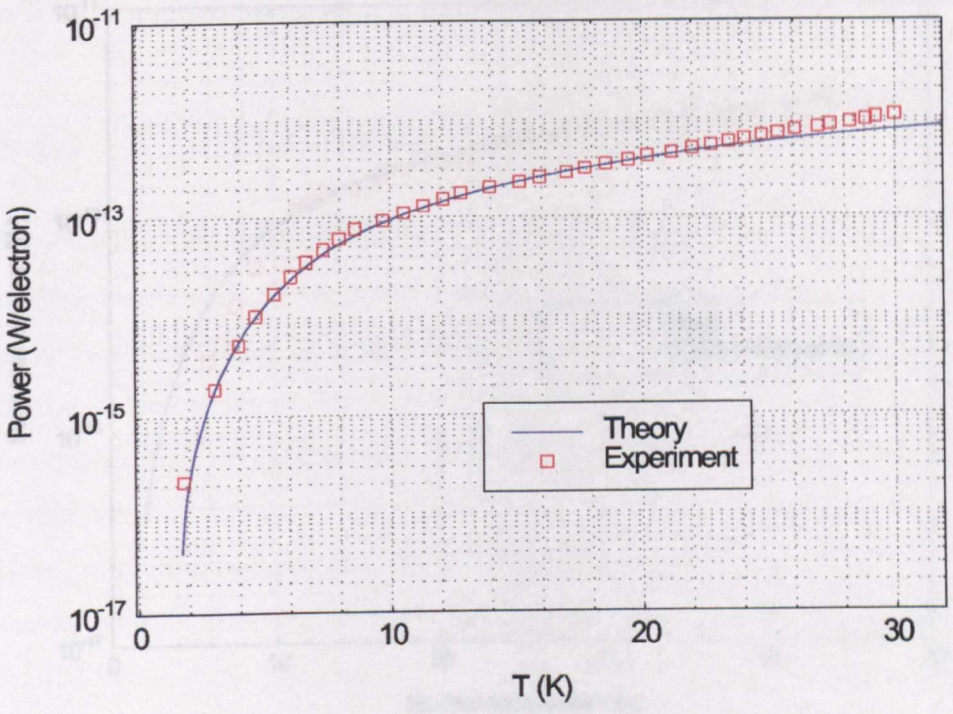

Figure 5.7: The power dissipated as a function of electron temperature for sample G 0–99.

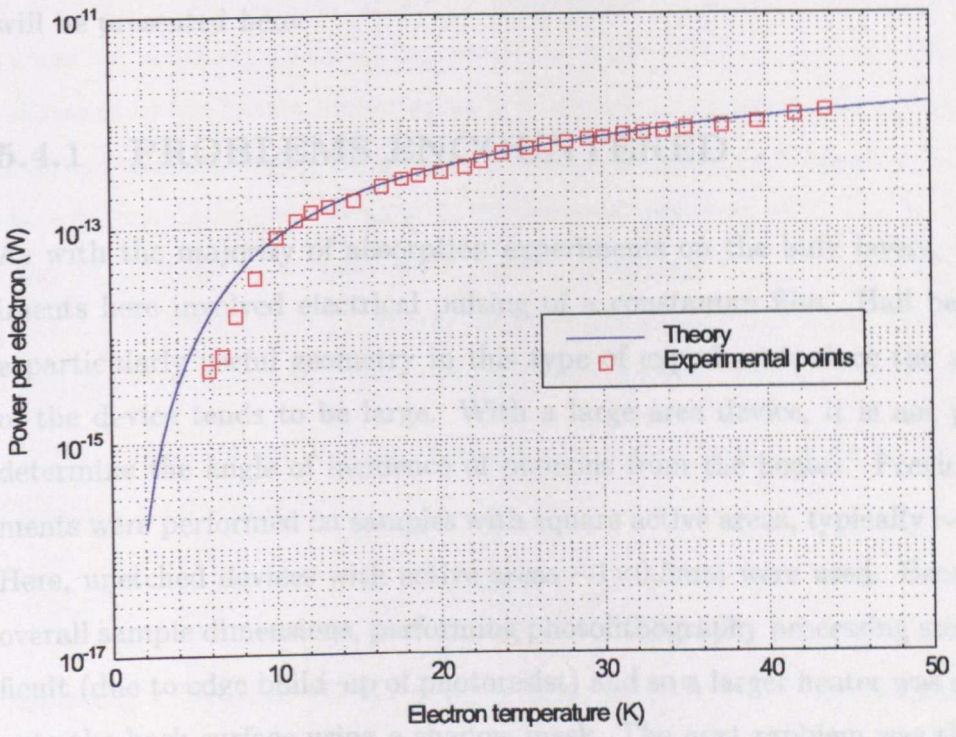

Figure 5.8: The power dissipated as a function of electron temperature for sample D982–AN26.

5.4 A PRELIMINARY STUDY OF PHONON ABSORPTION IN 2DEG's

This Section presents the results of the first phonon absorption experiments performed on AlGaN/GaN heterostructures. Two samples have been studied–the results obtained show very different behaviour. As this is an initial study, the purpose of which was to suggest future work, only a brief discussion of the results will be presented here.

5.4.1 PROBLEMS ENCOUNTERED

As with the majority of absorption experiments on the bulk layers, the experiments here involved electrical pulsing of a constantan film. Hall bars are not a particularly useful geometry in this type of experiment, since the active area of the device tends to be large. With a large area device, it is not possible to determine the angle of incidence of phonons from the heater. Previous experiments were performed on samples with square active areas, typically $\sim 10 \times 10 \mu$m. Here, unetched devices with active areas $\sim 1 \times 0.5$mm were used. Because of the overall sample dimensions, performing photolithography processing steps was difficult (due to edge build–up of photoresist) and so a larger heater was evaporated onto the back surface using a shadow mask. The next problem was that, due to samples being cut with the diamond saw, the edges were often a little chipped. Metal evaporated onto the back surface also sometimes coated the sample edges, making contact with the contact pads on the GaN side.

As previously, the technique of bias reversal and subtraction was employed to reduce pick–up effects. In these samples, even after subtraction, the effects of pick–up were still visible on the signal. A variant of the method is to reverse the heater pulse–in this case, the pick–up reverses but the phonon signal does not. Adding the two contributions should remove the effect of pick–up.

5.4.2 G0–40

The first 2DEG sample studied was G0–40. The sample was "characterised" using the same method as described previously. No Shubnikov–de Haas oscillations were visible in this sample. The sample was not illuminated. A typical heat pulse signal is shown in Figure 5.9.

The variation of the signal intensity with heater temperature is shown in Figure 5.10. The line shows a $T^{4.5}$ dependence. The temperature at which the power law dependence falls away occurs at ~27K. The ratio of the TA:LA modes decreases as the heater temperature is increased, as expected since the wavevector of TA phonons is higher than of LA phonons for the same frequency. The value of ω_{max} corresponding to the peak in the emitted spectrum at T_h can be determined from T_h'. Using $v_s = 2680$ ms^{-1}, this corresponds to $q \sim 4 \times 10^9$m^{-1}. Since phonons with wavevectors greater than $1/a_o$ cannot be absorbed, the value of the Fang–Howard parameter can be determined. In this sample, $a_o \sim 0.25$nm.

The predicted value of the Fang–Howard parameter can be calculated using Equation 5.4.1, from [36].

$$a_o = \left(\frac{48\pi m^* e^2 \frac{11}{32} n_s}{4\pi\varepsilon_r\varepsilon_o\hbar^2} \right)^{-1/3} \tag{5.4.1}$$

Assuming a "typical" carrier density of $n_s = 5 \times 10^{16}$m^{-2} and substituting the appropriate values into Equation 5.4.1, the Fang–Howard parameter is $a_o \sim 1$nm.

5.4.3 G0–155

Figure 5.11 shows the phonon absorption signal as a function of magnetic field. This was achieved by applying a constant heater voltage and gating the ballistic peak and recording the averaged intensity as the field was swept. In this measurement, the heater temperature was $T_h \sim 21$K, corresponding to a peak in phonon frequency of ~ 908GHz. Oscillations in the absorption are clearly visible. These oscillations are of large amplitude, suggesting the contacts to the 2DEG layer are of good quality. That these oscillations are of a much larger amplitude than

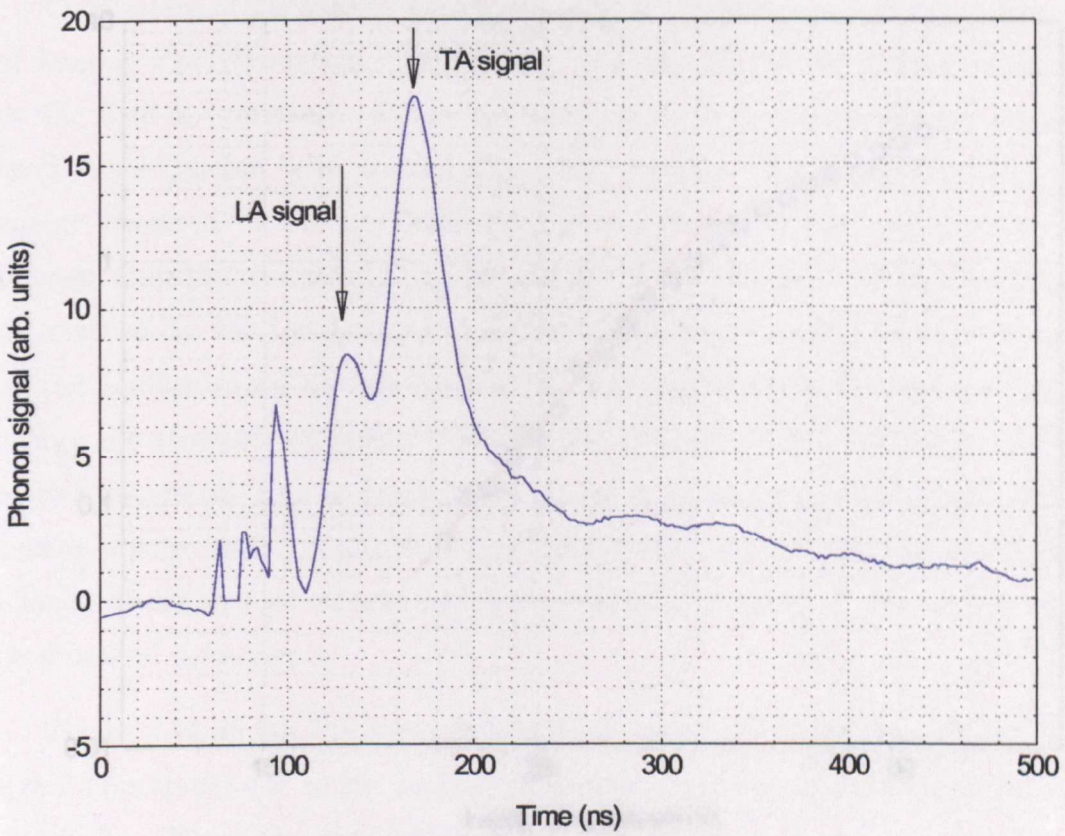

Figure 5.9: A typical heat pulse signal. The LA and TA peaks are marked. The effects of pick–up can be seen at ~60–110ns.

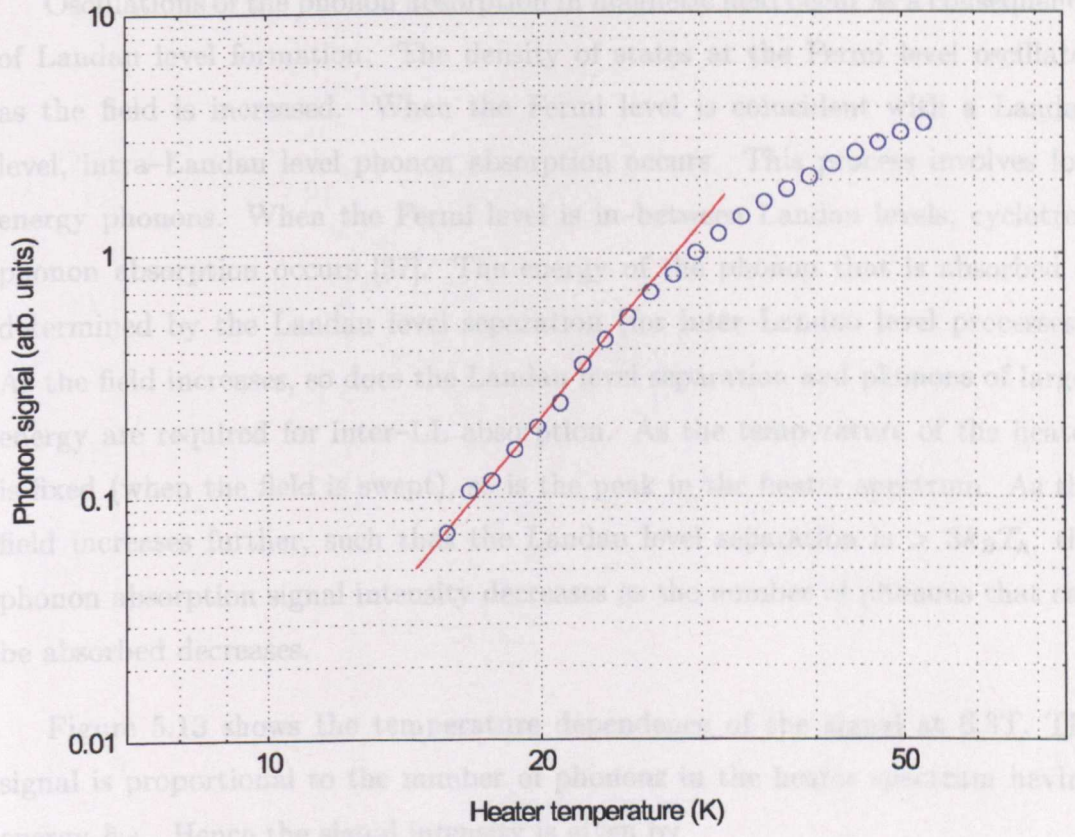

Figure 5.10: The dependence of signal intensity as a function of heater temperature for G0–40. The line shows a $T^{4.5}$ dependence.

in the SdH measurement demonstrates the sensitivity of the phonon absorption technique when measuring 2D systems, and arises due to the phonon absorption depending strongly on the density of states. The dependence of intensity on heater temperature was measured for several values of B. The temperature at which the curve falls away from the T^5 dependence as a function of field is shown in Figure 5.12.

Oscillations of the phonon absorption in magnetic field occur as a consequence of Landau level formation. The density of states at the Fermi level oscillates as the field is increased. When the Fermi level is coincident with a Landau level, intra–Landau level phonon absorption occurs. This process involves low energy phonons. When the Fermi level is in–between Landau levels, cyclotron phonon absorption occurs [37]. The energy of the phonon that is absorbed is determined by the Landau level separation (for inter–Landau level processes). As the field increases, so does the Landau level separation and phonons of larger energy are required for inter–LL absorption. As the temperature of the heater is fixed (when the field is swept), so is the peak in the heater spectrum. As the field increases further, such that the Landau level separation is $> 3k_BT_h$, the phonon absorption signal intensity decreases as the number of phonons that can be absorbed decreases.

Figure 5.13 shows the temperature dependence of the signal at 6.3T. The signal is proportional to the number of phonons in the heater spectrum having energy $\hbar\omega_c$. Hence the signal intensity is given by

$$Intensity \propto \frac{1}{exp\left(\frac{\hbar\omega_c}{k_BT_h}\right) - 1}$$

The solid line is a curve fit using the above expression. The cyclotron phonon absorption experiment allows the effective mass to be extracted [38]. Using the value obtained from the curve fit, the effective mass was determined, $m^* \sim 0.195m_e$.

Figure 5.14 shows the heater temperature dependence of G0–155 at zero field. The signal intensity falls away from a T^5 dependence at much lower temperatures

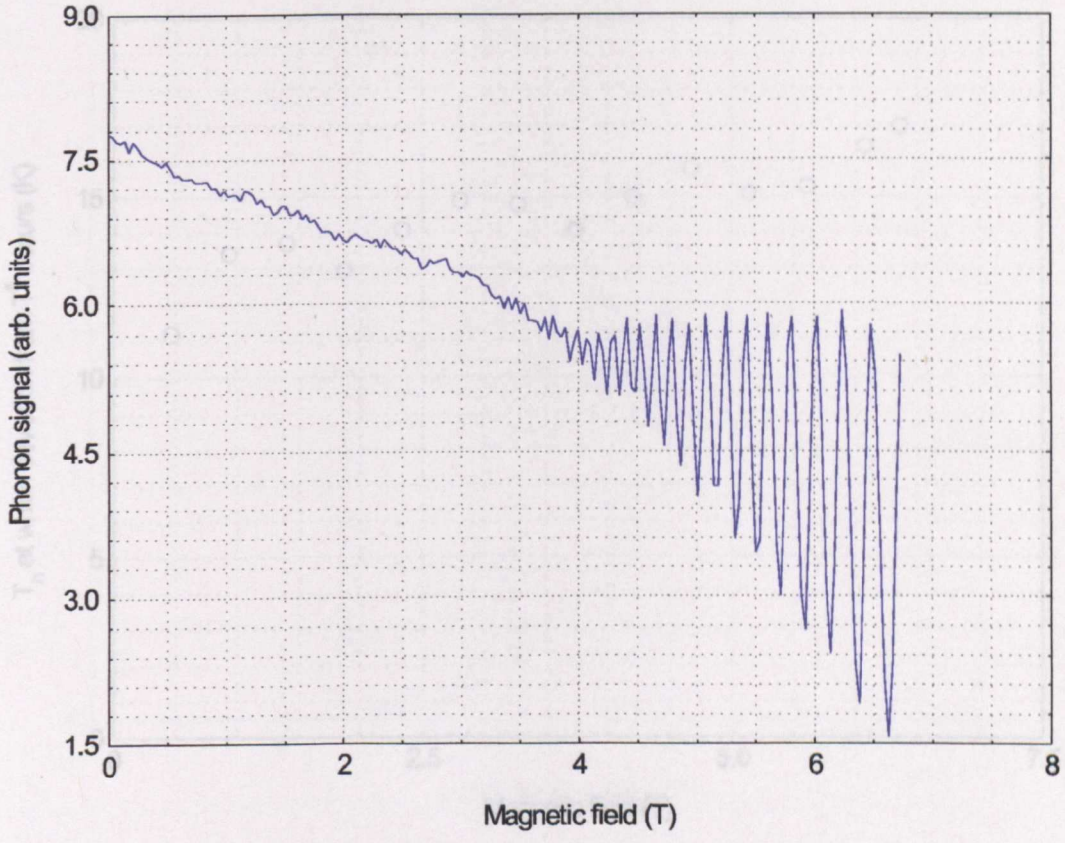

Figure 5.11: The dependence of signal intensity as a function of magnetic field for G0–155.

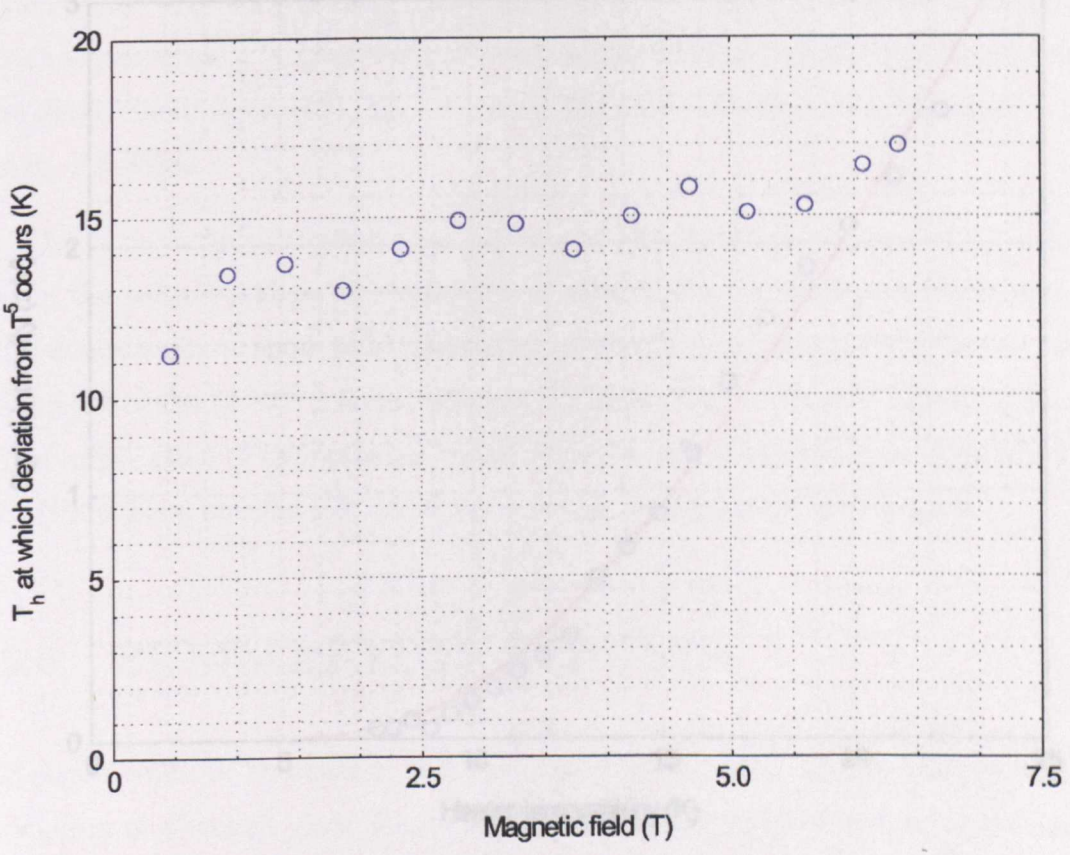

Figure 5.12: The temperature at which the sample falls away from T^5 dependence for G0–155.

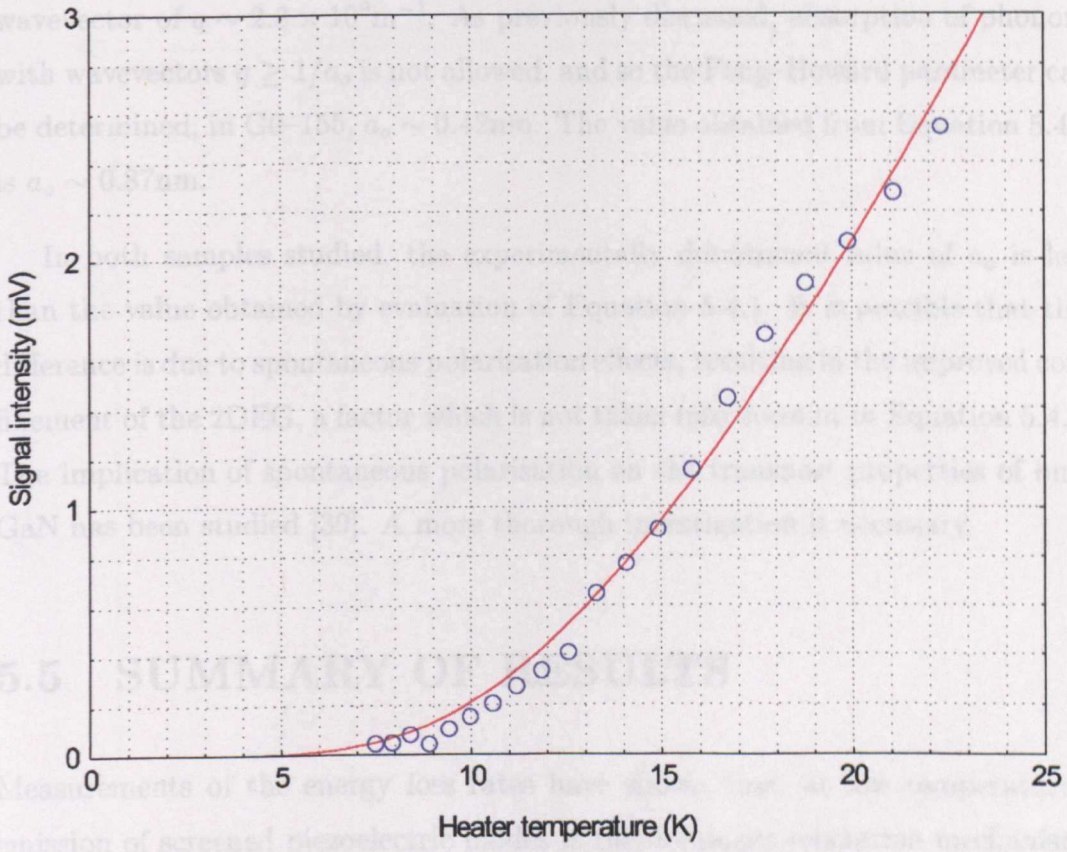

Figure 5.13: The dependence of signal intensity as a function of heater temperature for B = 6.3T. This field corresponds to a peak in the absorption signal.

than was seen in the bulk samples. In 2D electron systems, a T^5 is indicative of screened piezoelectric coupling. At higher heater temperatures, the dependence tends towards linear. As previously discussed, in 2D systems, knowing T_h' allows the "thickness" of the 2DEG to be calculated. (The carrier density, obtained previously from the Shubnikov–de Haas oscillation, is known). Experimentally, this temperature was observed to be ~16K. This corresponds to a maximum wavevector of $q \sim 2.3 \times 10^9 \mathrm{m}^{-1}$. As previously discussed, absorption of phonons with wavevectors $q \geq 1/a_o$ is not allowed, and so the Fang–Howard parameter can be determined; in G0–155, $a_o \sim 0.42\mathrm{nm}$. The value obtained from Equation 5.4.1 is $a_o \sim 0.87\mathrm{nm}$.

In both samples studied, the experimentally determined value of a_o is less than the value obtained by evaluation of Equation 5.4.1. It is possible that this difference is due to spontaneous polarisation effects, resulting in the improved confinement of the 2DEG, a factor which is not taken into account in Equation 5.4.1. The implication of spontaneous polarisation on the transport properties of bulk GaN has been studied [39]. A more thorough investigation is necessary.

5.5 SUMMARY OF RESULTS

Measurements of the energy loss rates have shown that, at low temperatures, emission of screened piezoelectric modes is the dominant relaxation mechanism. As the electron temperature is increased, the power loss approaches a linear dependence on T_e. The measurements, performed over a range of temperatures $T_e \sim$ 4K–35K, are in excellent agreement with the energy loss rates determined in a different experimental arrangement (for $T_e \sim$ 0.5K–10K).

Phonon absorption experiments, performed using a fixed phonon source, show at low heater temperatures, the absorption signal exhibits a T^5 dependence, indicative of absorption of TA phonons. Phonon absorption experiments have yielded the effective mass, $m^* \sim 0.195 m_e$, in good agreement with other reported values. The Fang–Howard parameter a_o, which is related to the "thickness" of

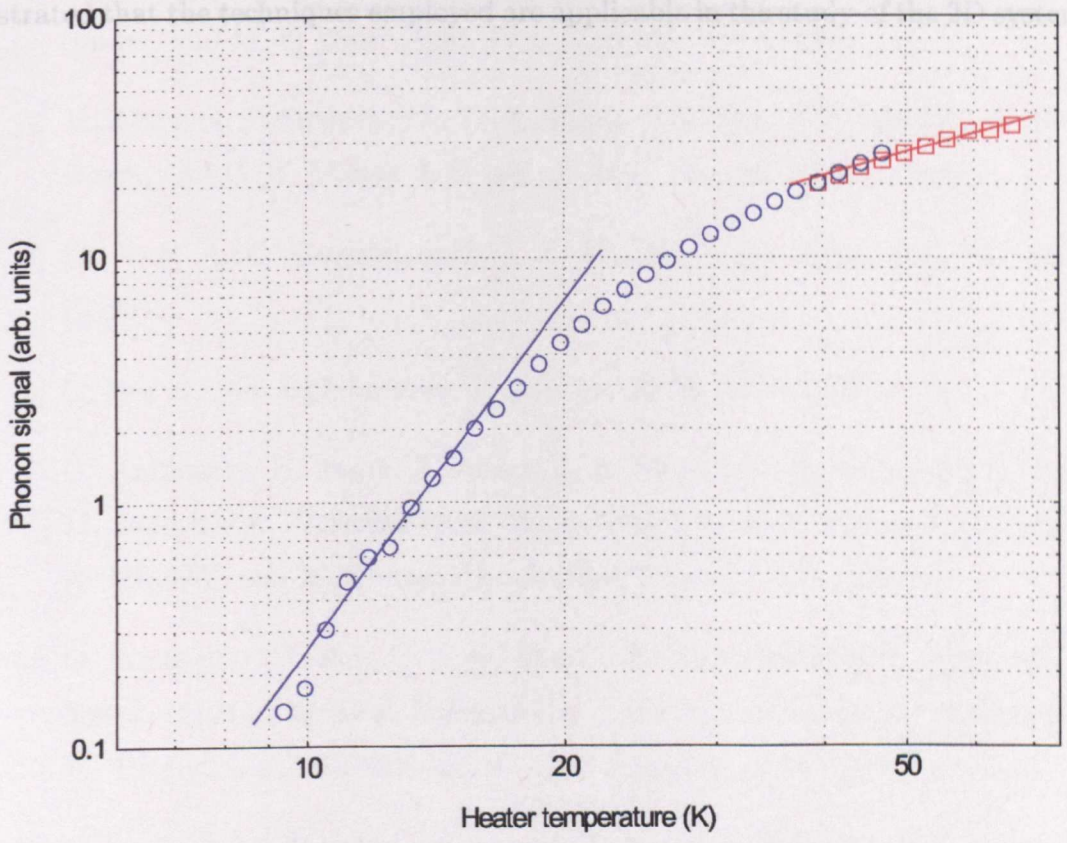

Figure 5.14: The dependence of signal intensity as a function of heater temperature for G0–155. The two symbols represent two data sets.

the 2D gas, has been determined experimentally. Comparison with the predictions of theory show that the confinement appears to be stronger than expected. This could be due to spontaneous polarisation effects in the AlGaN/GaN system causing improved confinement at the heterointerface.

The work presented here is of a preliminary nature – given the good agreement between the experimental data and predictions of theory, it has been demonstrated that the techniques employed are applicable in the study of the 2D system.

REFERENCES

[1] B. Shen, T. Someya, and Y. Arakawa. *Appl. Phys. Lett*, **76**, 2746, (2000).

[2] R. Gaska, M. S. Shur, A. D. Bykhovski, A. O. Orlov, and G. L. Snider. *Appl. Phys. Lett*, **74**, 287, (1999).

[3] R. Gaska, J. W. Yang, A. Osinsky, Q. Chen, M. A. Khan, A. O. Orlov, G. L. Snider, and M. S. Shur. *Appl. Phys. Lett*, **72**, 707, (1998).

[4] Y. Zhang, I. P. Smorchkova, C. R. Elsass, S. Keller, J. P. Ibbetson, S. DenBaars, and U. K. Mishra J. Singh. *J. Appl. Phys*, **87**, 7981, (2000).

[5] D. Jena, A. C. Gossard, and U. K. Mishra. *Appl. Phys. Lett*, **76**, 1707, (2000).

[6] L. Hsu and W. Walukiewicz. *Phys. Rev. B*, **56**, 1520, (1997).

[7] O. Ambacher, B. Foutz, J. Smart, J. R. Shealy, N. G. Weimann, K. Chu, M. Murphy, A. J. Sierakowski, W. J. Schaff, L. F. Eastman, R. Dmitrov, A. Mitchell, and M. Stutzmann. *J. Appl. Phys*, **87**, 334, (2000).

[8] O. Ambacher, J. Smart, J. R. Shealy, N. G. Weimann, K. Chu, W. J. Schaff, M. Murphy, L. F. Eastman, R. Dmitrov, L. Wittmer, M. Stutzmann, W. Rieger, and J. Hilsenbeck. *J. Appl. Phys*, **85**, 3222, (1999).

[9] R. Dmitrov, M. Murphy, J. Smart, W. J. Schaff, J. R. Shealy, L. F. Eastman, O. Ambacher, and M. Stutzmann. *J. Appl. Phys*, **87**, 3375, (2000).

[10] B. E. Foutz, O. Ambacher, M. J. Murphy, V. Tilak, and L. F. Eastman. *phys. stat. sol (b)*, **216**, 415, (1999).

[11] D. Qiao, L. S. Yu, S. S. Lau, G. J. Sullivan, S. Ruvimov, and Z. Liliental-Weber. *MRS Internet J.Nitride Semicond.Res.*, **4**, U62, (1999).

[12] Q. Z. Liu, L. S. Yu, F. Deng, S. S. Lau, Q. Chen, J. W. Yang, and M. A. Khan. *Appl. Phys. Lett*, **71**, 1658, (1997).

[13] D. Qiao, Z. F. Guan, J. Carlton, S. S. Lau, and G. J. Sullivan. *Appl. Phys. Lett*, **74**, 2652, (1999).

[14] T. Wang, Y. Ohno, M. Lachah, D. Nakagawa, T. Shirahama, S. Sakai, and H. Ohno. *phys. stat. sol (b)*, **216**, 743, (1999).

[15] T. Wang, Y. Ohno, M. Lachah, D. Nakagawa, T. Shirahama, S. Sakai, and H. Ohno. *Appl. Phys. Lett*, **74**, 3531, (1999).

[16] J. M. Redwing, M. A. Tischler, J. S. Flynn, S. Elhamri, M. Ahoujja, R. S. Newrock, and W. C. Mitchel. *Appl. Phys. Lett*, **69**, 963, (1996).

[17] S. Contreras, W. Knap, E. Frayssinet, M. L. Sadowski, M. Goiran, and M. Shur. *J. Appl. Phys*, **89**, 1251, (2001).

[18] Z. W. Zheng, B. Shen, R. Zhang, Y. S. Gui, C. P. Jiang, Z. X. Ma, G. Z. Zheng, S. L. Guo, Y. Shi, P. Han, Y. D. Zheng, T. Someya, and Y. Arakawa. *Phys. Rev. B*, **62**, R7739, (2000).

[19] H. van Houten, J. G. Williamson, M. E. I. Broekaart, C. T. Foxon, and J. J. Harris. *Phys. Rev. B*, **37**, 2756, (1988).

[20] A. Saxler, P. Debray, R. Perrin, S. Elhamri, W. C. Mitchel, C. R. Elsass, I. P. Smorchkova, B. Heying, E. Haus, P. Fini, J. P. Ibbeston, S. Keller, P. M. Petroff, S. P. DenBaars, U. K. Mishra, and J. S. Speck. *MRS Internet J.Nitride Semicond.Res.*, **F99**, W11.10, (1999).

[21] L. W. Wong, S. J. Cai, R. Li, K. Wang, H. W. Jiang, and M. Chen. *Appl. Phys. Lett*, **73**, 1391, (1998).

[22] S. Elhamri, R. S. Newrock, D. B. Mast, M. Ahoujja, W. C. Mitchel, J. M. Redwing, M. A. Tischler, and J. S. Flynn. *Phys. Rev. B*, **57**, 1374, (1998).

[23] T. Wang, J. Bai, S. Sakai, Y. Ohno, and H. Ohno. *Appl. Phys. Lett*, **76**, 2737, (2000).

[24] P. T. Coleridge. *Phys. Rev. B*, **44**, 3793, (1991).

[25] A. F. Brana, C. Diaz-Paniagua, F. Batallan, J. A. Garrido, E. Munoz, and F. Omnes. *J. Appl. Phys*, **88**, 932, (2000).

[26] H. X. Jiang M. A. Khan J. Z. Li, J. Y. Lin and Q. Chen. *Appl. Phys. Lett*, **72**, 2868, (1998).

[27] D. Meister, M. Topf, I. Dirnstorfer, B. K. Meyer, R. Schwarz, and M. Heuken. *phys. stat. sol (b)*, **216**, 749, (1999).

[28] R. Dietrich, A. Vescan, A. Wieszt, H. Leier, K. S. Boutros, J. M. Redwing, K. Kornitzer, R. Freitag, T. Ebner, and K. Thonke. *phys. stat. sol (a)*, **176**, 209, (1999).

[29] J. Y. Lin K. C. Zeng and H. X. Jiang. *Appl. Phys. Lett*, **76**, 1728, (2000).

[30] I. Shalish, L. Kronik, G. Segal, Y. Shapira, S. Zamir, B. Meyler, and J. Salzman. *Phys. Rev. B*, **61**, 15573, (2000).

[31] E. T. Yu K. S. Boutros X. Z. Dang, C. D. Wang and J. M. Redwing. *Appl. Phys. Lett*, **72**, 2745, (1998).

[32] O. P. Seifert, O. Kirfel, M. Munzel, M. T. Hirsch, J. Parisi, M. Kelly, O. Ambacher, and M. Stutzmann. *MRS Internet J.Nitride Semicond.Res.*, **4S1**, G5.5, (1998).

[33] H. X. Jiang M. A. Khan J. Z. Li, J. Y. Lin and Q. Chen. *J. Appl. Phys*, **82**, 1227, (1997).

[34] F. F. Ouali, H. R. Francis, and H. C. Rhodes. *Tr. J. of Physics*, **23**, 717, (1999).

[35] K. J. Lee, J. J. Harris, A. J. Kent, T. Wang, S. Sakai, D. K. Maude, and J. C. Portal. *Appl. Phys. Lett*, **78**, 2893, (2001).

[36] T. Ando, A. B. Fowler, and F. Stern. *Rev. Mod. Phys.*, **54**, 437, (1982).

[37] A. J. Kent, G. A. Hardy, P. Hawker, V. W. Rampton, M. I. Newton, P. A. Russell, and L. J. Challis. *Phys. Rev. Lett*, **61**, 180, (1988).

[38] A. J. Kent, R. E. Strickland, K. R. Strickland, and M. Henini. *Phys. Rev. B*, **54**, 2019, (1996).

[39] J. J. Harris, K. J. Lee, J. B. Webb, H. Tang, I. Harrison, L. B. Flannery, T. S. Cheng, and C. T. Foxon. *Semi. Sci. Tech*, **15**, 413, (2000).

Chapter 6

CONCLUSIONS AND FURTHER STUDY

6.1 SUMMARY OF RESULTS

The majority of work carried out has focussed on bulk GaN. Although some work has been performed on AlGaN/GaN 2DEG's, this work is of a preliminary nature, although early indications suggest that experiments and theory are in good agreement. With GaN devices successfully fabricated using wet etching methods, small area devices have been produced enabling high electron temperatures to be achieved.

The energy relaxation experiments, with the relaxation rate in GaN measured over a temperature range 1.5–250K, have yielded values of the optic phonon energy of 92 meV, in good agreement with theory and recent Raman studies. The crossover from acoustic phonon to optic phonon emission has been observed at $T \sim$100K, with optic emission becoming dominant at $T \sim$130K. The magnitude and temperature dependence of the energy relaxation are in good agreement with theoretical calculations using the literature value of the deformation potential constant and a modified piezoelectric coupling constant and neglecting screening. The electron–optic phonon relaxation time has been determined, and the values

of 5–10 fs obtained are again in good agreement with theory and Raman analysis. The absence of hot phonon effects up to the maximum electron temperature of ~300K in these measurements is noted. Deviations from theory, due primarily to emission of plasmon–LO phonon coupled modes is observed. Emission of TO modes and disorder induced relaxation of the $2k_F$ cut–off probably contributes in part to the deviation. Strong power law dependences occur in the low temperature regime that are consistent with the dominant coupling mechanism being the piezoelectric interaction.

Analysis of the heat pulse signals obtained in emission experiments have confirmed the findings of the relaxation experiments. Observation of shifts in the ballistic TA peak and the appearance of a large tail in the signals at temperatures of ~100K are consistent with the onset of optic phonon emission. Theoretical calculation of the TA:LA ratio at low temperatures are in good agreement with the observed values. In contrast to the energy relaxation experiments, at high electron temperatures, the nature of the heat pulse signals suggest hot phonon effects are present. The reason why this was not evident in transport measurements is due to destruction of the samples before enough high temperature measurements were made.

Absorption experiments have yielded further detailed information regarding the coupling mechanisms in GaN, and the nature of the cut–offs. Application of magnetic field enhanced the heat pulse signal, although illumination did not affect the signal intensities. Heat pulse signals obtained for the two doped samples as the field was varied show evidence of two competing contributions to the heat pulse signal. Weak localisation effects are expected to be important in these samples and could provide an explanation of the observed behaviour. No significant change in behaviour occurred when the field was applied parallel to (rather than the standard perpendicular to) the GaN/sapphire interface. The observed temperature dependences appear to be indicative of the dominance of coupling via the piezoelectric interaction. In undoped samples, the application of magnetic field had no effect on the observed heat pulses. The observed power law dependences show no correlation with sample carrier concentration or mobility,

and persist to much higher temperatures than theory predicts the $2k_F$ cut–off should allow. A linear dependence on temperature is observed at higher heater temperatures, characteristic of the equipartition regime. In these experiments, where the electrons remain cold, impurity band conduction is significant and the use of conventional theory is inappropriate. In this regime, the cut–off was associated not with $2k_F$, but with the electron mean free path, such that phonons with a wavevector $q \leq \ell^{-1}$ could be absorbed.

Imaging of sapphire using the sliding gate technique has proved successful, with detailed images of focussing for both modes. Images of the GaN epilayers have provided useful information about focussing in GaN. The transverse mode is similar to the pattern seen in pure sapphire. The LA mode images display features which are not seen in sapphire and further study is needed. Imaging of the phonon drag in GaN epilayers has further reinforced that, at low electron temperatures in these low mobility samples, conventional theory cannot be used.

Measurements of the energy relaxation rate in AlGaN/GaN heterostructures have provided excellent agreement between experiment and theory in the range 4K–$\sim$35K. Piezoelectric coupling is the dominant relaxation mechanism. The agreement between these measurements and other low temperature (mK to 4K) measurements is excellent. Extending the range of temperatures should be an obvious goal of future studies. The Fang–Howard parameter has been extracted from the phonon absorption results, as has the electron effective mass. In the samples studied, the Fang–Howard parameter was found to be $\sim$0.25nm in G0–40 and $\sim$0.5nm in G0-99, with both values lower than predicted. This is possibly due to the effects of spontaneous polarisation causing enhanced confinement of the 2DEG, which is not taken into account in the predicted value. The effective mass m^* was experimentally determined to be $\sim 0.195 m_e$, in good agreement with the accepted values.

6.2 FUTURE WORK AND UNFINISHED BUSINESS

It may prove useful to study emission in undoped samples, using aluminium and CdS bolometers, for completeness. Also, the higher density samples may provide useful information regarding the crossover from PZ to DP coupling. It is expected that for carrier concentrations higher than $\sim 1\times 10^{25}m^{-3}$, deformation potential coupling should be the dominant mechanism. The role of the GaN/sapphire interface is an unknown quantity. Reflection experiments could be performed (with a heater and bolometer on the same surface) which would help determine the quality of the interface [1]. Epilayers grown on thicker substrates would aid in reducing some of the problems associated with fast arrival times of the ballistic phonons. Phonon absorption experiments have shown that conventional theory cannot be applied to the low mobility samples, where impurity band conduction dominates at low temperatures. A better theoretical model is required when the condition $k_F\ell$ <1 is satisfied, using appropriate electron distribution functions and electron–phonon matrix elements.

The preliminary work on AlGaN/GaN heterostructures has proved successful. Performing absorption experiments has allowed the Fang–Howard parameter to be determined in two samples. This information may be of interest to growers, as the effects of strain relaxation and aluminium content on the 2DEG properties is still an area of discussion. An obvious extension to this preparatory study is to extend the energy relaxation measurements to higher carrier temperature. This will involve using a more sophisticated analysis method and adaptation of the experimental procedure. The success of the absorption experiments suggests that experiments to study phonon drag in these systems may yield further information regarding the cut–offs of the interaction. Widely studied in AlGaAs/GaAs heterostructures at low temperatures is the "dirty–limit"; it may be interesting to study the relatively low mobility AlGaN/GaN samples in detail–the change in temperature dependence associated with this limit should be measurable in the current experimental arrangement. Previous studies of AlGaAs/GaAs have

compared the angular dependence of emission and absorption processes with theoretical predictions. This has not yet been attempted in the samples studied in this work although small active area devices must be fabricated before these can be performed. The use of "inverted" heterostructures (a GaN/AlGaN/GaN sandwich) would possibly allow wet etching of small active area devices [2].

An obvious extension to this work is to use the techniques described in this work in the study of in other low dimensional systems. Similar techniques have been successfully employed in the study of GaAs based quantum wires and dots– the growth of GaN quantum dots is currently receiving much attention [3] - [6], and the study of this system would be of interest.

Bulk InGaN samples, grown by MBE, have been processed using RIE to define the active areas. Little is known about the quality of these samples, although recently there has been much speculation regarding phase separation of the system. It is believed that indium segregation leads to the formation of quantum dots in this material. It may be a useful exercise to perform the same experiments as in bulk GaN, especially since the MBE samples are of varying indium content (10%–50%). Theorists have predicted the values of the optic phonon energy for varying composition [7]. To date, there has been no study of the varying value with density.

There has been much interest recently in the emergence of the arsenide–nitride systems due to the relatively strong blue luminescence which has been observed [8], [9]. Again, compositions varying between 1% As and ~50% As in GaAsN have been grown by MBE and may be of interest to study.

The possibility of doping MBE GaN with manganese has also received attention recently due to its magnetic properties [10], [11]. The theoretical prediction is that the Curie temperature will be reasonably high compared to other materials. With the experimental set–up available, the study of this material could provide useful information about basic material properties.

The experiments to date have proved useful and instructive in understanding the fundamental behaviour of GaN and preliminary measurements of Al-

GaN/GaN heterostructures indicate the techniques used should be successful when applied to low dimensional systems.

REFERENCES

[1] A. G. Kozorezov and T. Miyasato J. K. Wigmore. *J.Phys:Condens. Matter*, **8**, 1, (1996).

[2] M. J. Murphy, K. Chu, H. Wu, W. Yeo, W. J. Schaff, O. Ambacher, J. Smart, J. R. Shealy, L. F. Eastman, and T. J. Eustis. *J. Vac. Sci. Technol. B*, **17**, 1252, (1999).

[3] B. Daudin, F. Widmann, G. Feuillet, C. Aldemann, Y. Samson, M. Arlery, and J. L. Rouviere. *Mat. Sci. Eng. B*, **50**, 8, (1997).

[4] S. Tanaka, I. Suemune, P. Ramvall, and Y. Aoyagi. *phys. stat. sol (b)*, **216**, 431, (1999).

[5] P. Ramvall, S. Tanaka, S. Nomura, P. Riblet, and Y. Aoyagi. *Appl. Phys. Lett*, **75**, 1935, (1999).

[6] P. Ramvall, P. Riblet, S. Nomura, Y. Aoyagi, and S. Tanaka. *J. Appl. Phys*, **87**, 3883, (2000).

[7] F. Bechstedt and H. Grille. *phys. stat. sol (b)*, **216**, 761, (1999).

[8] A. J. Winser, S. V. Novikov, C. S. Davis, T. S. Cheng, C. T. Foxon, and I. Harrison. *Appl. Phys. Lett*, **77**, 2506, (2000).

[9] S. V. Novikov, A. J. Winser, I. Harrison, C. S. Davis, and C. T. Foxon. *Semi. Sci. Tech*, **16**, 103, (2001).

[10] M. Zajac, R. Doradzinski, J. Gosk, J. Szczytko, M. Lefeld-Sosnowska, M. Kaminska, A. Twardowski, M. Palczewska, E. Grzanka, and W. Gebicki. *Appl. Phys. Lett*, **78**, 1276, (2001).

[11] C. Y. Fong, V. A. Gubanov, and C. Boekema. *J. Elec. Mat*, **29**, 1067, (2000).

APPENDIX I

.1 INTRODUCTION

The purpose of the Appendix is to discuss in detail the etching process used in the fabrication of GaN devices. Device manufacture was an important part of this work–preliminary energy relaxation experiments were performed using devices where the active area was defined by the contacts [1], and due to this area being large ($\sim 2 \times 10^{-7}\mathrm{m}^2$ compared with $\sim 1 \times 10^{-10}\mathrm{m}^2$ as used in the majority of experiments) the power input to the device was not sufficiently high to raise the electron temperature much above the crossover point where optic emission dominates.

Attempts to wet etch GaN had met with limited success until it was noted that photoenhancement of the etch gave etch rates which were comparable to, and in some cases greater than, dry etching techniques [2]. This prompted a number of investigations into wet etching methods, the majority on MOCVD material. The results of these studies are in some cases contradictory. (The interest in wet etching is due in part to the possibilty of dry etching causing appreciable damage to the sample and it is also often a lengthy process.) The desire for smaller active areas and in–house processing prompted an investigation into the possibilty of wet etching of MBE material. Characterisation of the etch was achieved using a Tencor alpha–step, SEM and AFM imaging.

.2 BACKGROUND

A variety of mineral acids and bases have been used in efforts to etch GaN. With the sample illuminated with a UV source, it was found that GaN could be etched with potassium hydroxide solution. Etching using hydrochloric acid [2], phosphoric acid [3], ethylene glycol and tartaric acid [4] have produced low etch rates or surface contamination requiring addition cleaning steps; the favoured etchant is potassium hydroxide, although recent work suggests sodium hydroxide as an alternative [5]. No etching was observed when GaN was illuminated with below band gap illumination. The majority of previous work uses a mercury arc lamp as the UV source (see, for example, [6], [7]), although helium–cadmium lasers have also been used [8].

The etch rate increases with increasing temperature–illuminating the sample causes no significant heating of the solution [2].

.3 THE RESULTS OF WET ETCHING

The first attempts to etch the samples followed the initial recipe as described in [9], an unstirred 0.04M KOH solution. When used to etch MOCVD material, an etch rate of $\sim$ 300nm min^{-1} was observed. This is in stark contrast to the behaviour with MBE material. With the etch depth checked at regular intervals, no etching was observed after 30 minutes in solution. Sample illumination was provided by a mercury arc lamp (with a characteristic wavelength of 365 nm). The intensity at the sample was $\sim$ 7mW cm^{-2}, lower than in other studies. Since the position of the lamp was fixed in the experimental arrangement used, a focussing lens was added, increasing the intensity at the sample to $\sim$ 12mW cm^{-2}. The solution concentration was increased to 0.2M and after 100 minutes, the recorded etch depth was 1.8μm. Increasing the concentration further was found to increase the etch rate–solutions above $\sim$0.5M were found to inhibit the etch rate. All further etching used a 0.5M stirred solution since this gave the maximum etch rate. The etching was performed at room temperature. A quartz

lens was added to the experimental arrangement to further focus the light onto the sample.

The most striking difference between material grown by MOCVD and MBE is the maximum etch rate attained; reported values for MOCVD material are as high as 400nm min^{-1}. The highest etch rate achieved in MBE material was $\sim$ 45nm min^{-1}. The "final" surface morphology was found to vary between samples which were etched under the same conditions. Figures .1 and .2 show an AFM image of the unetched surface and an SEM image of the surface after etching. Clearly visible are "whiskers"; these features are $\sim 2\mu$m in height. A previous study using MOCVD material has produced a similar surface. The formation of whiskers was observed under conditions of low concentration and illumination intensity with no stirring [10]. In contrast, higher solution strength and illumination intensity, with the solution stirred produced a smooth surface [9]. Surface contamination, either prior to etching or due to the products of the etch process, was proposed as a possible cause of whisker formation. To check that this was not responsible for the observed behaviour, the sample was suspended in solution at an angle of $\sim 45°$. If surface debris was the cause, then it was expected that the whiskers would be tilted also. SEM images showed no difference between the tilted and flat etches. The most favoured explanation of this behaviour is that the etch is revealing threading dislocations. Why dislocations are not etched is still an area of discussion. It is possible that the dislocations are trapping carriers and preventing any significant etching from occurring. This seems reasonable given the density of whiskers and the large density of dislocations in this material.

Figures .3 and .4 show the surface prior to etching and the post etching morphology for MG 675. The etch depth is $\sim 1.4\mu$m. The layer thickness provided by the growers is a little thicker, although variations in temperature across the substrate could account for differing growth rates and hence thickness. The edge walls are angled, as are the grains of remaining material. The reason for this crystallographic etch is not clear.

Figures .5 and .6 show pre and post etching surfaces for MG 676. In this case, the etch depth is $\sim 1.5\mu$m, and the surface shows similar, but much smaller,

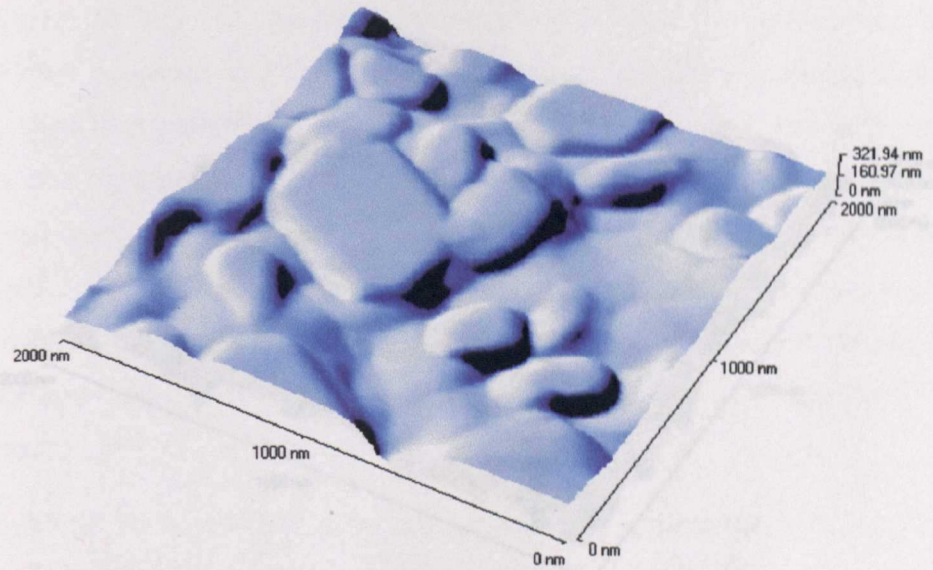

Figure .1: An AFM image of MG 716 prior to etching.

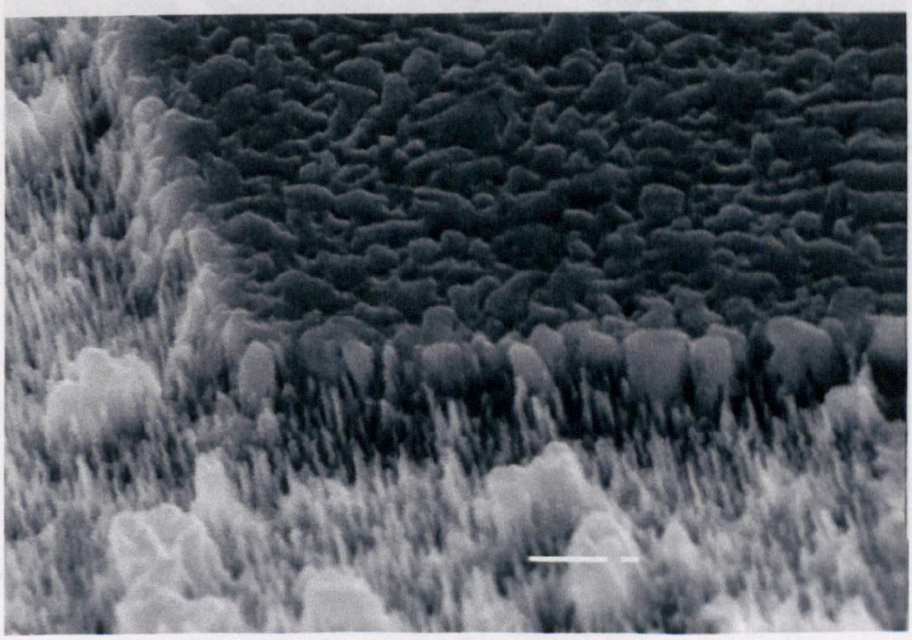

Figure .2: An SEM image of MG 716 after etching. The whiskers are clearly visible.

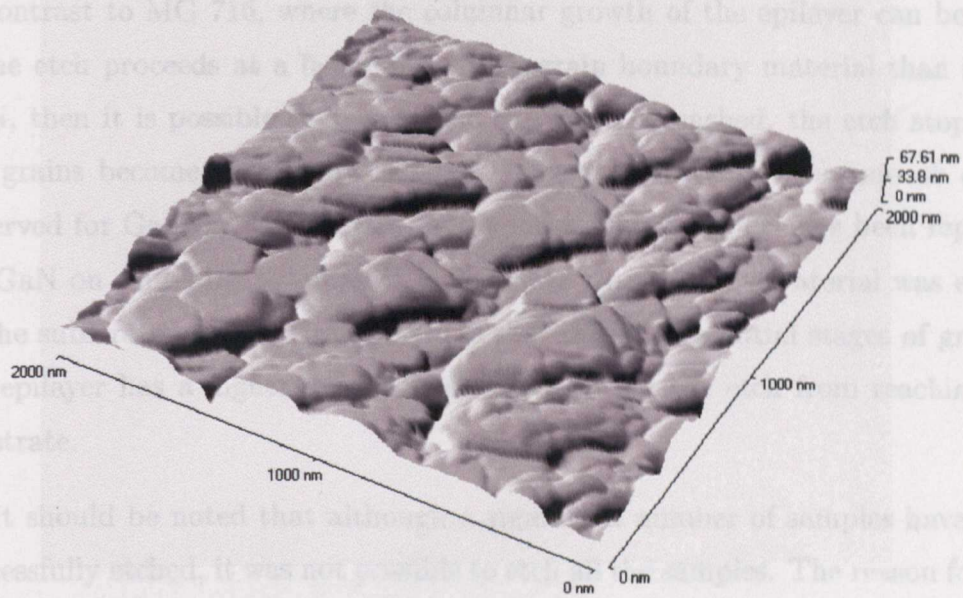

Figure .3: An AFM image of MG 675 prior to etching.

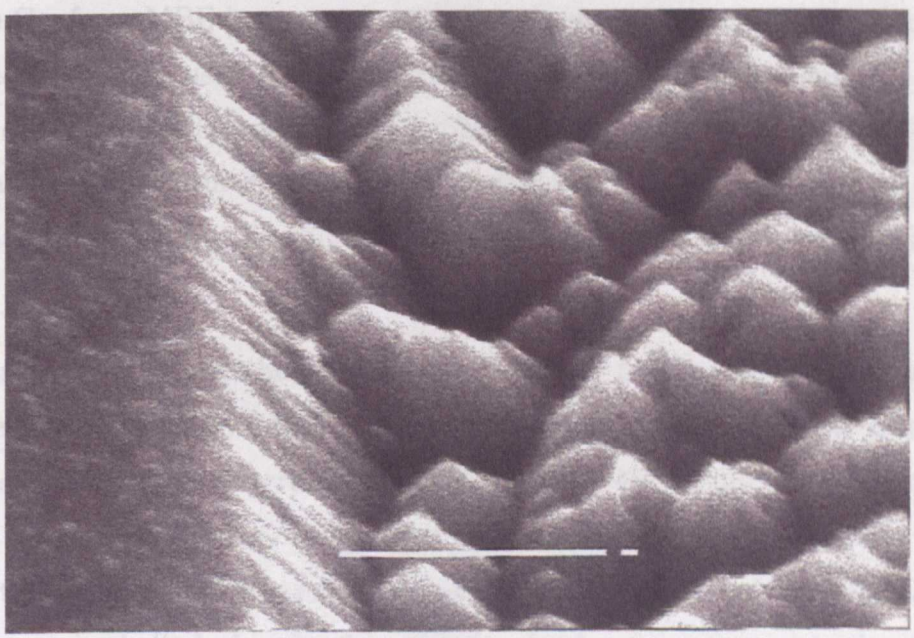

Figure .4: An SEM image of MG 675 after etching. The etch depth is $\sim$1.4μm.

features than MG 675. Striations in the side wall are visible, as in MG 675, but in contrast to MG 716, where the columnar growth of the epilayer can be seen. If the etch proceeds at a faster rate along grain boundary material than in the GaN, then it is possible that when the substrate is reached, the etch stops and the grains become electrically isolated. This would account for smooth etches observed for GaN on SiC samples, but smooth morphologies have been reported for GaN on sapphire, although it is not clear whether this material was etched to the substrate. Another possibility is that during the initial stages of growth, the epilayer has a higher defect density, preventing the etch from reaching the substrate.

It should be noted that although a significant number of samples have been successfully etched, it was not possible to etch all the samples. The reason for this is unclear. It has been proposed that polarity plays a significant role in chemical etching. Polarity determination is not trivial–the test of polarity seems to be based on whether good 2DEG's can be grown on the epilayers. Since MOCVD material has produced the highest mobility 2DEG's, it is assumed that these layers are Ga–face. MBE is assumed to be N–polarity. In this study, MBE material has been primarily used for device fabrication; not all samples could be etched which could suggest layers of different polarity. The presence of a buffer layer or nitridation of the surface prior to growth could be possible explanations for the material difference, but no correlation between growth strategy and etching was found.

Four samples were etched as part of a "test" for polarity determination. GaN epilayers were grown by MBE on template layers ($\sim 5\mu$m thickness) from AXT and Gent. The AXT material is grown by HVPE. The results of etching studies on the bare AXT layer are shown in Figures .7 and .8. The sample was etched under the same conditions as previous samples. In this sample. the etch rate was $\sim$ 150nm min^{-1}. Striations in the sidewalls are clearly visible, as is the "lifting" of the Ti capping layer. The etch depth is $\sim 5.5\mu$m.

In Figures .9 and .10, the results of etching the MBE material on the template layer are shown. Slight undercutting of the MBE material is visible, as are

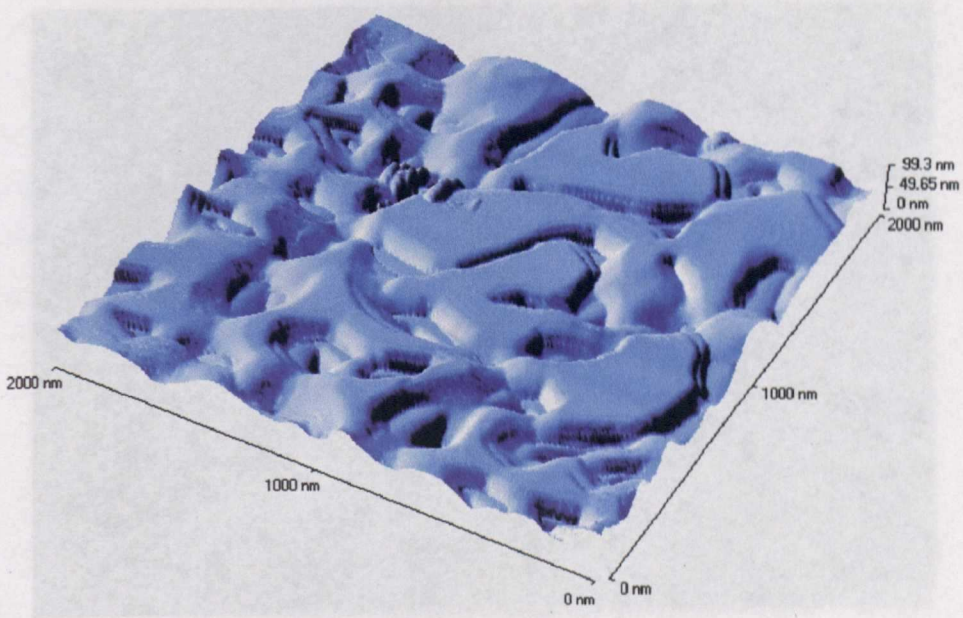

Figure .5: An AFM image of MG 676 prior to etching.

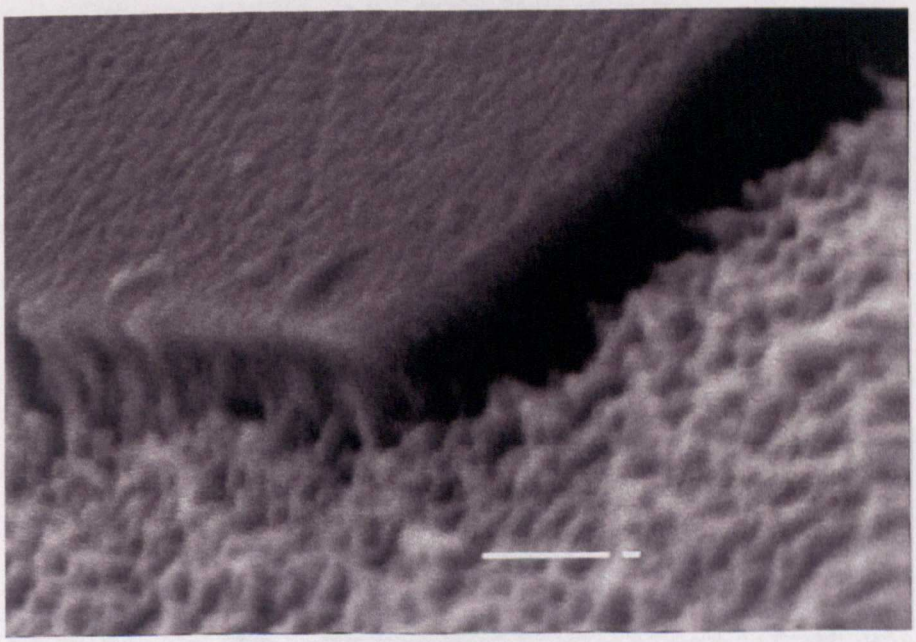

Figure .6: An SEM image of MG 676 (with the Ti capping layer) after etching.

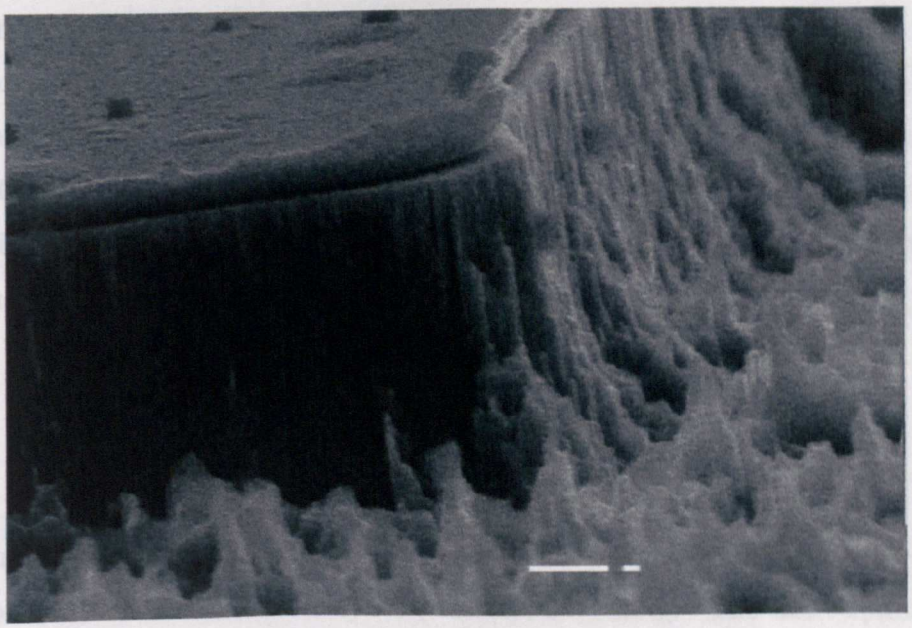

Figure .7: An SEM image of the AXT template layer after etching.

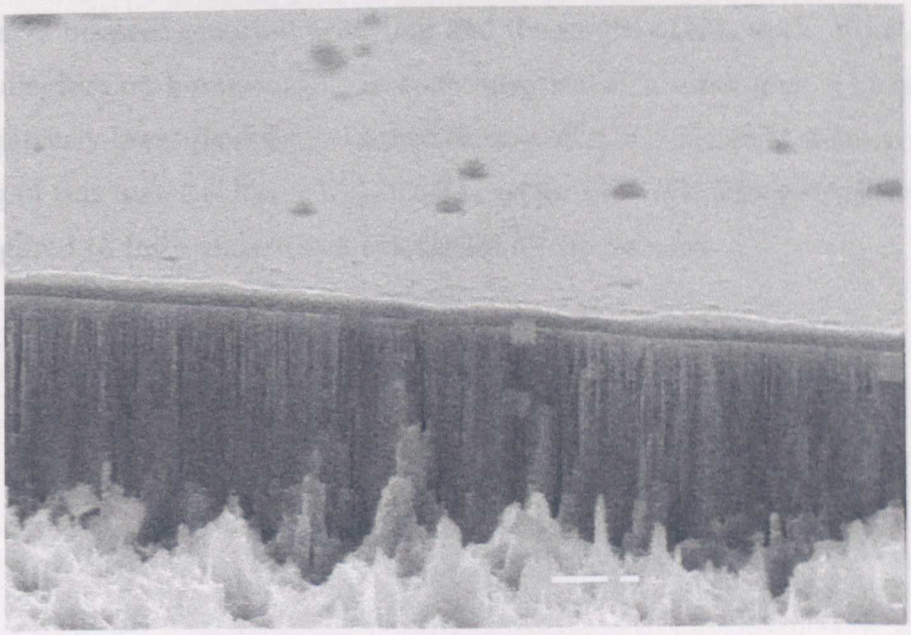

Figure .8: An SEM image of the AXT template layer after etching.

striations on the sidewall. The interface between MBE epilayer is clearly visible. The etch rate was slightly lower in this sample than for the bare template layer. In contrast to these results, the Gent template layer did not etch, nor did the epilayer grown on it. This would suggest that the template layers are of different polarity and that the MBE grows layers of the same polarity as the underlying material. This was a preliminary study–more samples must be studied before any conclusions can be drawn.

.4 SUMMARY

The main objective of this part of the work was achieved–successful device fabrication with mesa definition by wet chemical etching. The active areas were well–defined, with no rounding of the corners. The production of smaller active area devices using this method should be possible, since no significant undercutting is observed after prolonged exposure of the sample to the etchant.

The mechanism behind the etch process remains unclear–there are striking differences between reported behaviour and the results of this work. Final surface morphologies vary between samples under identical etch conditions. The etch rate is consistently lower than that attained during MOCVD material etching–indeed, etching of this material has not been achieved in this work. More detailed studies are required to fully understand the nature of this process.

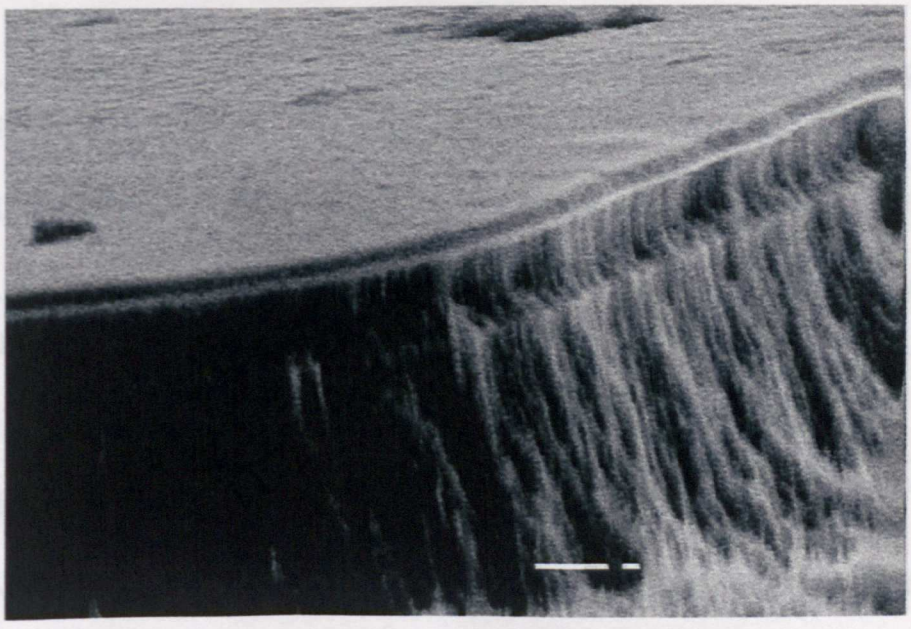

Figure .9: An SEM image of MG 787 after etching.

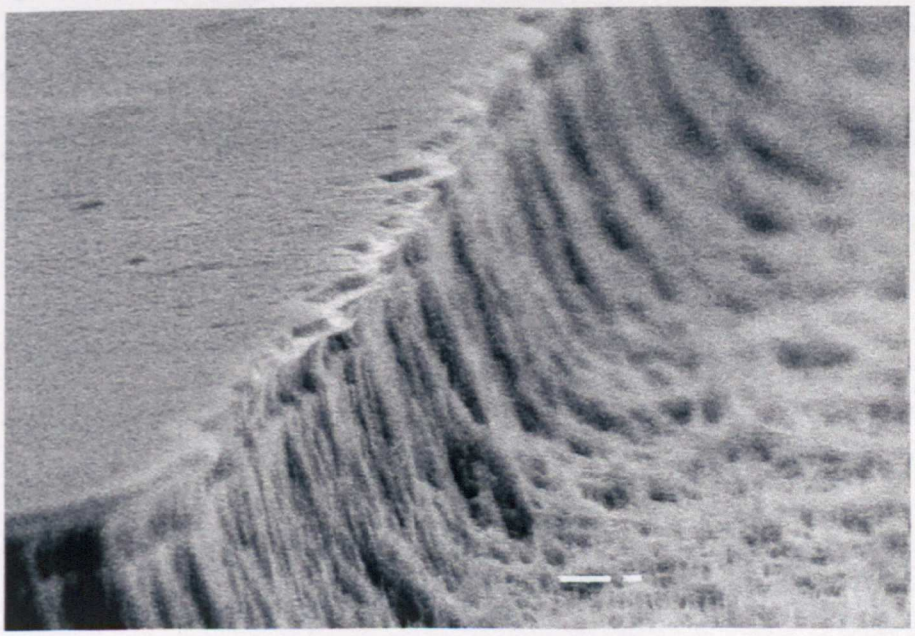

Figure .10: An SEM image of MG 787 after etching.

REFERENCES

[1] P. Hawker, A. J. Kent, T. S. Cheng, and C. T. Foxon. *Physica B*, **263-264**, 227, (1999).

[2] M. S. Minsky, M. White, and E. L. Hu. *Appl. Phys. Lett*, **68**, 1531, (1996).

[3] L. H. Peng, C. W. Chuang, Y. C. Hsu, J. K. Ho, C. N. Huang, and C. Y. Chen. *IEEE J. Sel. Qua. Elec*, **4**, 564, (1998).

[4] H. Lu, Z. Wu, and I. Bhat. *J. Electrochem. Soc*, **144**, L8, (1997).

[5] M. Ohkubo. *J. Cryst. Growth*, **189 / 190**, 734, (1998).

[6] C. Youtsey, G. Bulman, and I. Adesida. *J. Elec. Mat*, **27**, 282, (1998).

[7] C. Youtsey, I. Adesida, L. T. Romano, and G. Bulman. *Appl. Phys. Lett*, **72**, 560, (1998).

[8] L. H. Peng, C. W. Chuang, J. K. Ho, C. N. Huang, and C. Y. Chen. *Appl. Phys. Lett*, **72**, 939, (1998).

[9] C. Youtsey, I. Adesida, and G. Bulman. *Appl. Phys. Lett*, **71**, 2151, (1997).

[10] C. Youtsey, L. T. Romano, and I. Adesida. *Appl. Phys. Lett*, **73**, 797, (1998).